Aus dem Institut für Physik der Universität Potsdam

Oscillatory Instability of Dense and Dissipative Keplerian Shear Flow

Dissertation

zur Erlangung des akademischen Grades
Doktor der Naturwissenschaften
(Dr. rer. nat.)
in der Wissenschaftsdisziplin Theoretische Physik

eingereicht an der
Mathematisch–Naturwissenschaftlichen Fakultät
der Universität Potsdam

von
Jürgen Schmidt

Potsdam, im Oktober 2000

Contents

Short Summary

In this thesis the oscillatory instability of a dense collision–dominated planetary ring is considered in the framework of a hydrodynamic model. The motivation for the study is the search for intrinsic instabilities in the ring's flow which might cause part of the yet unexplained radial structuring found in Saturn's B ring. Such intrinsic instabilities, discussed in the literature in the framework of hydrodynamic models, were the so called viscous instability (Ward, 1981; Lin & Bodenheimer, 1981) and the viscous oscillatory instability (Schmit & Tscharnuter, 1995). While the viscous instability is improbable for plausible conditions for the Saturnian B ring, the oscillatory instability seems promising.
An existing model (Schmit & Tscharnuter, 1995) is generalized here by the hydrodynamic heat flow equation and investigated for linear stability. The growth of oscillatory unstable modes, the oscillation frequencies, and the eigenfunctions are in a quantitative agreement with direct local simulations of a dense planetary ring (Schmidt et al., 2000). Essential for the good agreement is the inclusion of the heat flow equation and new estimations for the transports of momentum and energy in simulations (Salo et al., 2000b).

Introduction

"I am not aware that any practical use has been made of Saturn's rings, either in astronomy or in navigation ... But when we contemplated the rings from a purely scientific point of view, they become the most remarkable bodies in the heavens, except, perhaps, for those still less useful bodies—the spiral nebulae ..."

—James Clerk Maxwell, 1856

Our understanding of the Saturnian ring system has developed rapidly since the Voyager missions sent their data to earth. Still many questions wait for a convincing answer. One of the most puzzling features seen in the Voyager images is the so called irregular structure (Cuzzi et al., 1984) of the dense main rings, most dominant in the B ring (Smith et al., 1982; Lane et al., 1982). The ring seems to be divided into a huge number of ringlets of various sizes and widths. The fluctuations in the radial density profile of the ring are found down to the instrumental resolution limit of the Voyager experiments.

Orbital resonances with outer Saturnian satellites explain isolated features in the Voyager data (Lissauer & Cuzzi, 1982; Rosen et al., 1991), but for the formation of the bulk of the structure none of the existing models is generally accepted at present. One process that could form radial structure – under conditions that are consistent with observational and theoretical constraints on the properties of the B ring – is the viscous oscillatory instability of Keplerian shear flow.

An isothermal hydrodynamic model for the oscillatory instability in the B ring was proposed by Schmit & Tscharnuter (1995). In this thesis this model is extended by the hydrodynamic heat–flow equation, allowing for spatial and temporal perturbations of the energy of the random motion of the ring particles. This is motivated by significantly smaller growth rates of oscillatory instability found in direct N-particle simulations of ring systems (Salo et al., 2000b) compared to the growth rates predicted by the isothermal model. In particular, the simulations show oscillatory instability only for dense systems that are flattened due to the influence of the disk's self–gravity. An isothermal model leads to unstable oscillatory modes even for a moderately dense ring without self–gravity. With the heat–flow an additional diffusion mechanism is introduced in the system which in general can be expected to have a stabilizing effect, and thus, could explain the difference between model and simulations. The possibility that the heat–flow equation might be of quantitative importance for the stability of planetary rings was already pointed out in Stewart et al. (1984).

The inclusion of the energy balance equation leads to several complications of the treatment compared to the isothermal case. On the one hand there is the obvious complication by an additional mode, corresponding to an additional eigenfunction of the linearized equations. So, for instance, many calculations can be done analytically in the isothermal model, like the determination of the marginal eigenfunctions, or the computation of a Landau type equation for the development of the system in the weakly nonlinear regime. This is technically more involved in a non–isothermal model. On the other hand a number of additional parameters are introduced with the heat–flow equation. For the investigation of the linear stability now one needs to know, besides the hydrodynamic transport coefficients, about temperature derivatives of several quantities (pressure, viscosity, and granular cooling), in addition to their spatial derivatives. Here, a basic problem of the modeling of planetary rings is met: the transport coefficients and the equation of state of such a flow are only poorly known. The best constrained quantity seems to be at present the shear viscosity. Analytical estimations exist for the shear viscosity (Araki & Tremaine, 1986) that are supported by results from event driven local N-particle simulations (Wisdom & Tremaine, 1988; Salo, 1991) and by observational constraints from the damping of resonantly driven density waves (Shu, 1984; Shu et al., 1985a; Shu et al., 1985b). For the bulk viscosity and the heat conductivity no estimates exist so far for the material flow in a planetary ring, but it can be shown that already in the isothermal model the bulk viscosity influences sensitively the stability of the system. For the purpose of the current study a new approach is followed: The transport coefficients, the equation of state, and the cooling function, as well as their derivatives, when needed, are determined directly from simulational systems (Salo et al., 2000b). This allows a direct comparison of the hydrodynamic theory and the instabilities that are observed in the simulations. This is in itself an important test of the applicability of hydrodynamic modeling, since, if no consistency can be achieved between theory and simulations that are carried out under the same idealizing assumptions, it seems hopeless to conclude from the theoretical results on the behavior of a Saturnian ring.

The theoretical predictions of this thesis will be tested by the imaging of the rings by the Cassini–Mission, planned to go in orbit around Saturn in 2004: with the high resolution images of the narrow–angle cameras onboard Cassini it will be possible to verify if the B ring is in a state that is affected by oscillatory instability.

In chapter 1 a brief introduction is given on the history of exploration of Saturn's ring system, the appearance of the main rings, and their basic properties, with emphasize on the radial structure. Also the models discussed so far in the literature in favor of an explanation of the structure are shortly discussed. Chapter 2 introduces the hydrodynamic model for the ring's flow that includes the energy balance equation. This is exemplified by a simple model for the vertical structure of a dense collision–dominated non–selfgravitating planetary ring, displaying also the limits of hydrodynamic modeling for this system. In the first part of chapter 3 the non–isothermal model is analyzed for linear stability, the linear stability of non-axisymmetric modes is shortly discussed, the dispersion relation for the radial modes is derived, and a long wavelength approximation for the roots of this relation is given. The second part of that chapter provides an estimation of the various parameters needed for a qualitative discussion of the stability behavior implied by the dispersion relation. The last part of chapter 3 is devoted to the computation of a Landau equation for the nonlinear saturation and nonlinear competition of left and right traveling oscillatory unstable modes in a self–gravitating isothermal model. In chapter 4 the development of unstable oscillatory modes in simulations is described. Further, it is shown how the parameters of the hydrodynamic dispersion relation can be determined directly from the simulations. The comparison of the hydrodynamic model to the simulations, given in chapter 5, is basically restricted on the development of the oscillatory unstable modes in the linear regime, as the growth rates, oscillation frequency, and the relative amplitudes and phases of the state variables. Here, a good quantitative agreement is found. Implications from the weakly nonlinear isothermal model developed in chapter 3 are in qualitative agreement with the long term evolution of the oscillatory unstable modes observed in simulations.

Chapter 1

The Saturnian Ring System

“It is girdled by a thin flat ring, nowhere touching, inclined to the ecliptic”

—Christian Huygens, *The System of Saturn, 1659*

Apparently Galileo Galileo in 1610 was the first to detect the rings of Saturn. Through his self–constructed telescope he saw the left and right ansae of the main rings as bright hazy spots left and right to the planet and called them the ”Saturnian branch stars”. It was some 50 years later that Christian Huygens explained the phenomenon with a thin ring that surrounds Saturn, inclined to the ecliptic and in 1675 Giovanni Dominico Cassini discovered the dark division between the A and B ring, the first structure that has been seen in the rings. It was his son Jacques Cassini who suggested in 1715 that the ring was formed by many satellites that orbit the planet in one plane, the satellites themselves being too small to be distinguished from earth. Already in 1755 Immanuel Kant predicted the ring to be divided into ringlets, envisioning ideas that are similar to the viscous diffusion instability that was discussed more than 200 years later. At the end of the 18th century Laplace concluded that the disk cannot be one solid object and suggested that the ring consists rather of many narrow solid ringlets, since a solid disk should break apart due to centrifugal forces. Roche suggested in 1848 that the rings are the result of the disruption of a large satellite near Saturn. In 1859 James Clerk Maxwell (Maxwell, 1859) proved that solid ringlets also cannot be stable and concludes ”*the only viable system of rings reduces to an innumerable number of uncorrelated particles orbiting around the planet with different velocities . . . these particles may be assembled into a system of narrow rings or they may move one after the other without any particular regularity . . . the tendency of the particles to coagulate into narrow rings . . . retards the disintegration process”*. In the second half of the 19th century several observers reported a subdivision of the A and B rings into concentric dark and bright bands. The many particle model was confirmed in 1895 by Keeler who measured the orbital velocity of the ring using the Doppler effect, showing a rotation law that was in accordance with Kepler’s laws. The important role of collisions in such a system of many particles was pointed out by Jeffreys (1947), who argued that the collisions must be inelastic, leading to a rapid damping of the random motions of the particles, and thus, to a flattening of the disk. A minimum random velocity, and therefore a minimum thickness of the disk, would be maintained by unavoidable collisions of particles of radius R_p on nearby circular Keplerian orbits, given by the difference in circumferential velocity $2R_p\Omega$.

With the improved technical capabilities of the 20th century the quality and the amount of observational data available for the rings of Saturn has rapidly increased, culminating in the local probing of the rings in course of space missions, Pioneer 11 in 1979, and the Voyager 1 and 2 flybys 1980 and 1981. Only in the Voyager data the true variety in the appearance of the rings became visible. One of the most striking features, and yet not explained, is the radial structure, most pronounced in the B ring.

Figure 1.1: *Saturn and his main rings in a Voyager image. The A ring (outermost) and the brighter B ring are separated by the dark Cassini Division. The C ring lies within the B ring and is much fainter. An impression of the opacity can be got from the lit face of the planet shining through the rings.*

1.1 Properties of the Dense Saturnian Rings

This section describes briefly basic properties of the opaque Saturnian rings, the A and the B ring, their extensions, density profiles, and properties of the particles. This provides merely a crucial background necessary for an understanding of the instability mechanism presented in section 2 as well as the approximations made in the model. A detailed overview of the appearance and properties of Saturn's rings and the ongoing physical processes can be found in the book "Planetary Rings"(Greenberg & Brahic, 1984), in particular the chapters by Cuzzi et al. and Stewart et al., introductory texts are the review articles by Spahn (1992) or Durisen (1999). The painting by Bill Hartman [fig (1.2)] gives an impression of how Saturn's rings could look like for an observer in the ring plane.

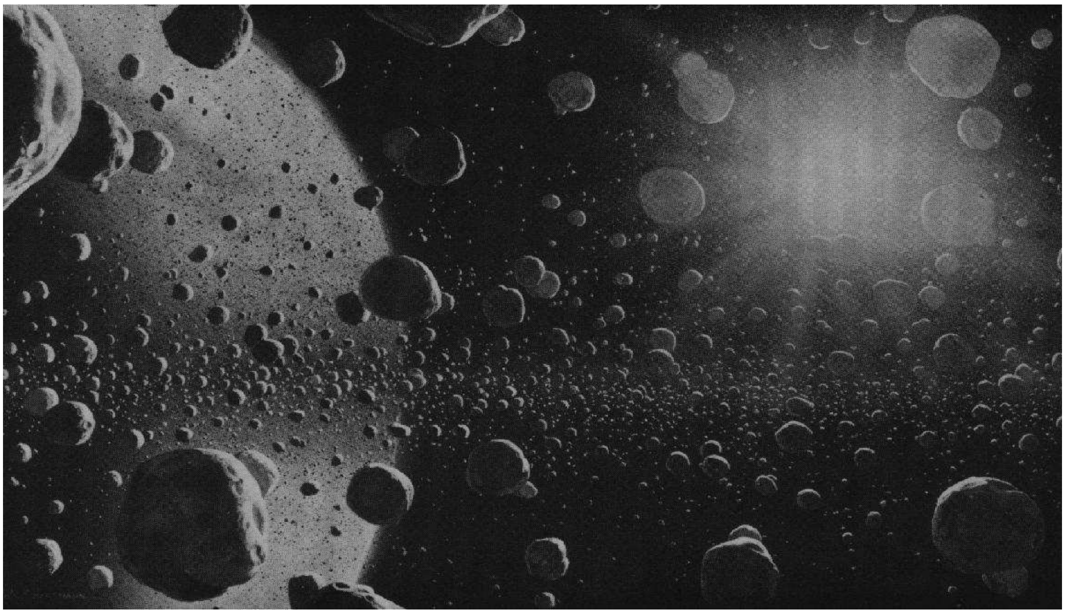

Figure 1.2: *The view of the rings for an observer in the ring plane as imagined by the painter Bill Hartman. The ring particles are believed to consist of water ice, their size-distribution having an upper limit of a few meters and ranging down to centimeters. Particles collide frequently, in the order of 10–100 times per orbital period.*

Particle Properties

Observations of the infrared spectrum of Saturn's rings (Kuiper et al., 1970; Pilcher et al., 1970) are consistent with the ring particles formed of water ice, the deviations in the spectral properties being mainly attributed to a small abundance of silicates (Cuzzi et al., 1984). Independently, the measurements of the particles' size distribution (Marouf et al., 1983), optical depth (defined below) [Lane et al. (1982)], and the estimation of the mass surface density of the rings by the observed characteristics of density waves (Holberg et al., 1982; Esposito et al., 1983) together imply a particle bulk density close to the one of water ice.

The size distribution of the particles is inferred from the light scattering properties of the rings at different wavelengths (Marouf et al., 1982; 1983; Zebker et al., 1985). In general the so obtained size distribution in the A and B ring follows approximately a differential power law (Cuzzi et al., 1984)

$$n(R) = n_0 R^{-3}, \quad 1\,\mathrm{cm} < R < 5\,\mathrm{m}\,, \tag{1.1}$$

with lower and upper cut off at a radius of 1 cm and 5 m, respectively. The measurements suggest that only very few bodies with $R > 10\,\mathrm{m}$ are present in the rings, following perhaps a very steep power law $\propto r^{-5}$ (Cuzzi et al., 1984). Radiative transfer models for a more recent stellar occultation observed from earth (French et al., 2000) infer an exponent of -2.75 in the above power law and a lower and upper cut off of 30cm and 20m, respectively. However, as discussed in French et al. (2000) this upper size limit could also represent loose particle aggregates of meter–sized particles, rather than individual particles.

A radial variation of the ring color is observed (Estrada & Cuzzi, 1996), which seems in some regions to be correlated with the radial structure visible in figures (1.4) and (1.6), and in other regions not. Such color differences may be attributed to a different abundance of impurities in the water ice, or, to radial variations in the particle size distribution (Cuzzi et al., 1984; Estrada & Cuzzi, 1996; Cuzzi & Estrada, 1998).

Optical Depth Profile

The (normal) optical depth τ is a measure for the surface fraction of the ring that is covered by the ring particles, defined as

$$\tau = \int_{R_{min}}^{R_{max}} \mathrm{d}R\, n(R)\, \pi R^2 \,, \tag{1.2}$$

where $n(R)$ is the number density per unit surface in the particle size increment $\mathrm{d}R$ at particle radius R. For uni–sized spheres with $R = R_p$ the optical depth is thus

$$\tau = \sigma \frac{\pi R_p^2}{m_p} \tag{1.3}$$

with the mass surface density σ and the particle mass m_p. The optical depth can be directly determined measuring the light flux of a star of known optical properties transmitted through the rings (such stellar occultation experiments were carried out by the Voyager missions and also earth based occultations have been recorded). The optical depth profile of the A, B,

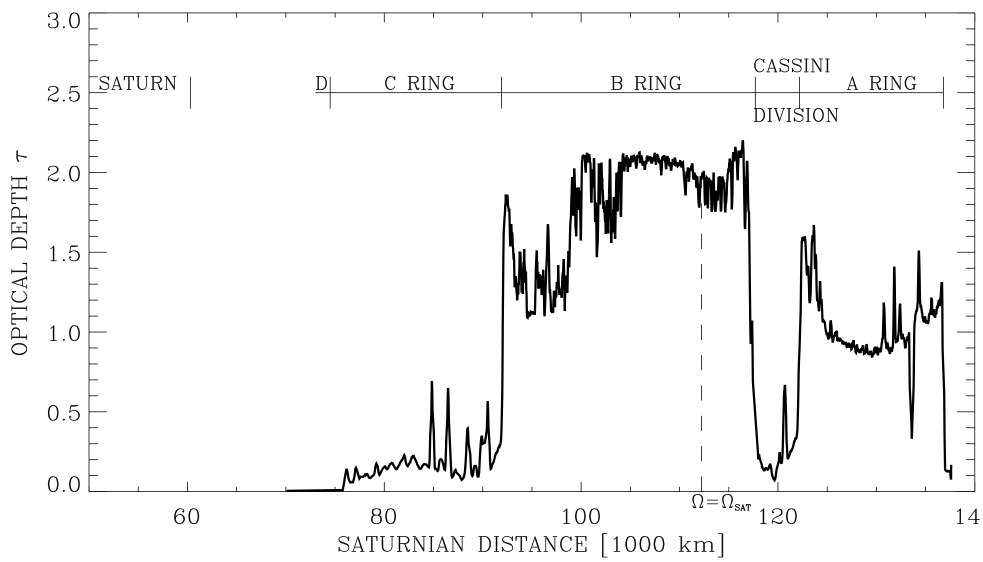

Figure 1.3: *Optical depth profile of the Saturnian main rings, A, B, and C, from the Voyager PPS data. Small scale fluctuations that reach optical depths as high as $\tau = 3$ in the B ring are smoothed by a local averaging.*

and the C ring is shown in fig (1.3) obtained from the Voyager photo polarimeter (PPS) experiment. Small scale fluctuations are smoothed by a local averaging over neighboring data points to display the global variation. By far the highest opacity is found in the outer parts of the B ring, with optical depth exceeding 2. An image of the main rings in transmitted light is shown in fig (1.4c) where the dense regions now appear dark. This image also exemplifies that there are many similarities between the C ring and the Cassini division.

A comparison of optical depth profiles for the Saturnian ring system of the Voyager experiments and several more recent earth based stellar occultation experiments is given in Nicholson et al. (2000).

Ring Thickness

From the Voyager PPS stellar occultation experiment an extremely sharp edge of the outer A ring can be deduced (Lane et al., 1982). The sharpness of the edge places an upper limit on the particles random motion deviating from the mean circular Keplerian motion of the ring. This limits also the thickness of that part of the ring to be less than 200 m (Lane et al., 1982). Since sharp ring edges can only be maintained against the process of viscous spreading by energy input (e.g. by orbital resonances with moons), the inner parts of the rings, in general lacking such a steady energy supply, can be expected to be even thinner. The upper limit for the ring thickness is consistent with the results from N–particle simulations [Wisdom & Tremaine (1988), Salo (1991), see also chapter 2.2], and with simple estimations of the vertical density profile (Stewart et al., 1984) as

$$\varrho(z) = \varrho(0) \exp\{-\frac{\Omega^2}{2c^2} z^2\} , \tag{1.4}$$

where c is the particles' velocity dispersion and Ω the Kepler frequency. In general the dissipative nature of the collisions of the ring particles tends to decrease the velocity dispersion. However, as mentioned in the introduction of this chapter it was already pointed out by Jeffreys (1947) that the system should maintain a minimum velocity dispersion of a few times $R_p\Omega$ due to the finite particle radius R_p. This estimation implies also a vertical scale hight in the order of a few particle diameters only.

The thickness of the main rings of Saturn is more crudely constrained by observations during crossings of the Saturnian ring plane by the earth, when the rings can be viewed edge–on, to be on the order of a few kilometers (Brahic & Sicardy, 1981). From observations with the Hubble Space Telescope of the latest such configuration a thickness of 2.4 ± 1.3 km was deduced (Nicholson et al., 1996). This apparent thickness is mainly attributed to a large scale warping of the ring plane (Burns et al., 1979) due to the gravitational influence of the massive Saturnian moon Titan, and to inclination gravitational resonances of the ring material with the moon Mimas that cause bending wave trains (vertical oscillations) in the A ring with an amplitude estimated to be about 1 km (Shu et al., 1983). The influence of the thickness of the F ring on the photometry is discussed for the 1995 edge–on observations in Nicholson et al. (1996) and Poulet et al. (2000).

Irregular Structure in the B Ring

The pronounced radial structure of the B ring is best visible in the Voyager images shown in fig (1.4), in particular in frame (a) with the outermost part of the B ring. Frame (b) opposes images of the neighborhood of the Cassini–Division from opposite sides of the planet. The ringlet in the center is clearly eccentric, and also the edge of the B ring (left, bright) varies roughly 50 km with longitude. This edge is attributed to the gravitational influence of the Saturnian moon Mimas whose 2:1 horizontal orbital resonance coincides with the edge. Also visible is a mismatch of the finer structure in the outer parts of the B ring, indicating an azimuthal variation or a time variability. The B ring is the densest planetary ring with optical depths mostly larger than one and in some parts as high as 3 which translates into

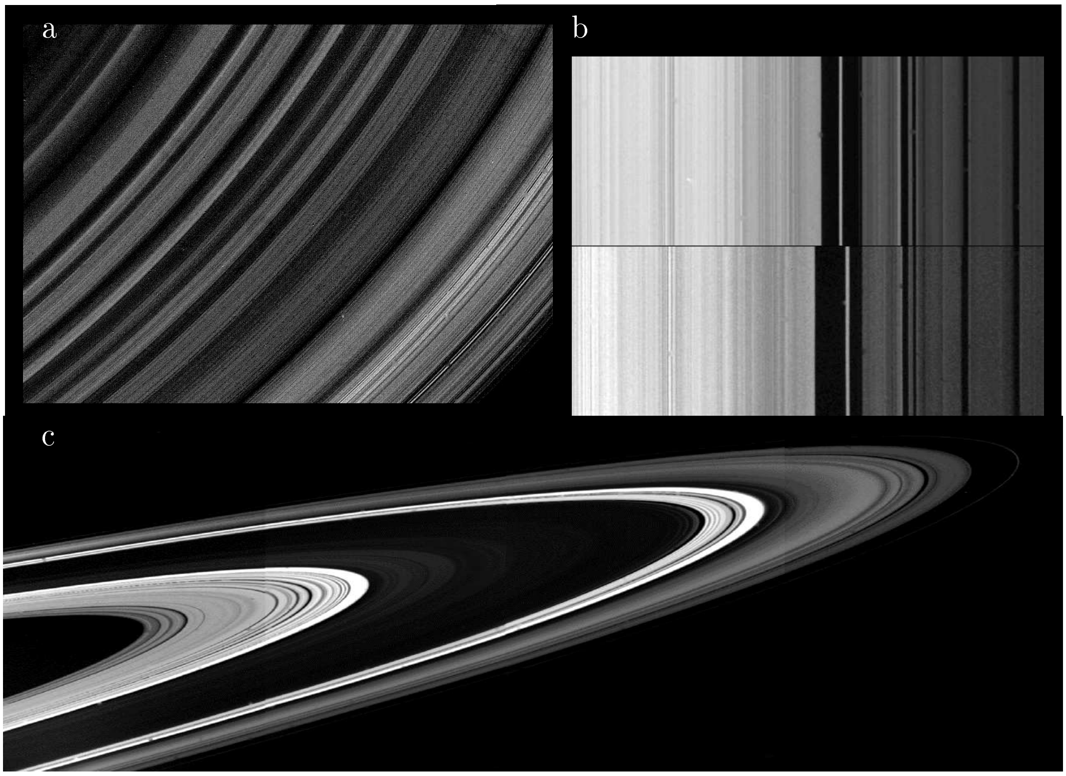

Figure 1.4: *Voyager images of the Saturnian ring system. Frame (a): The lit face of the B ring from a distance of 700,000 km covering a range of 6,000 km. Frame (b): The outer edge of the B ring (left, bright) and the inner edge of the Cassini division (right, dark). The upper and lower image are from opposite sides of the planet. The edge of the B ring shows a variation with longitude of roughly 50 km. Also visible is a mismatch of the finer structure in that part of the B ring, indicating an azimuthal variation or a time variability. Frame (c): The un-lit side of the rings, where the optical thin regions, i.e. the C ring and the Cassini division, appear brightest. The opaque B ring appears black, while the somewhat less dense A ring is in intermediate level of brightness.*

a surface density of 1000 to $2000\,\mathrm{kg/m^2}$ for a particle bulk density of $1000\,\mathrm{kg/m^3}$ and a particle size distribution given by eq (1.1).

The B ring seems to be split into a large number of concentric ringlets with various widths and at various distances. This structure persists, depending on the radial position in the B ring, down to the resolution limit (a few kilometers) of the imaging of the Voyager missions (ISS) and the photo-polarimeter experiment (PPS) (down to 100 m). In fig (1.5) the fluctuations are shown for the inner and outer part B ring (Saturnian distance $93,000$ km to $95,000$ km and $115,000$ km to $117,500$ km) in a plot taken from Cuzzi et al. (1984) obtained form the Voyager ultraviolet spectrometer (UVS) data. The radial scale of the fluctuations in this data set is smaller in the denser outer part, practically seen down to the resolution limit of 3 km of the UVS. On the other hand more recent studies of Voyager 2 images (Horn & Cuzzi, 1996) imply a weak dominance of a scale–length of about 100 km of the structure in the inner B ring between its inner edge and about $100,000$ km, being replaced by a preferred length of about $200 - 300$ km between $100,000$ and $116,000$ km [see fig (1.3) for the location

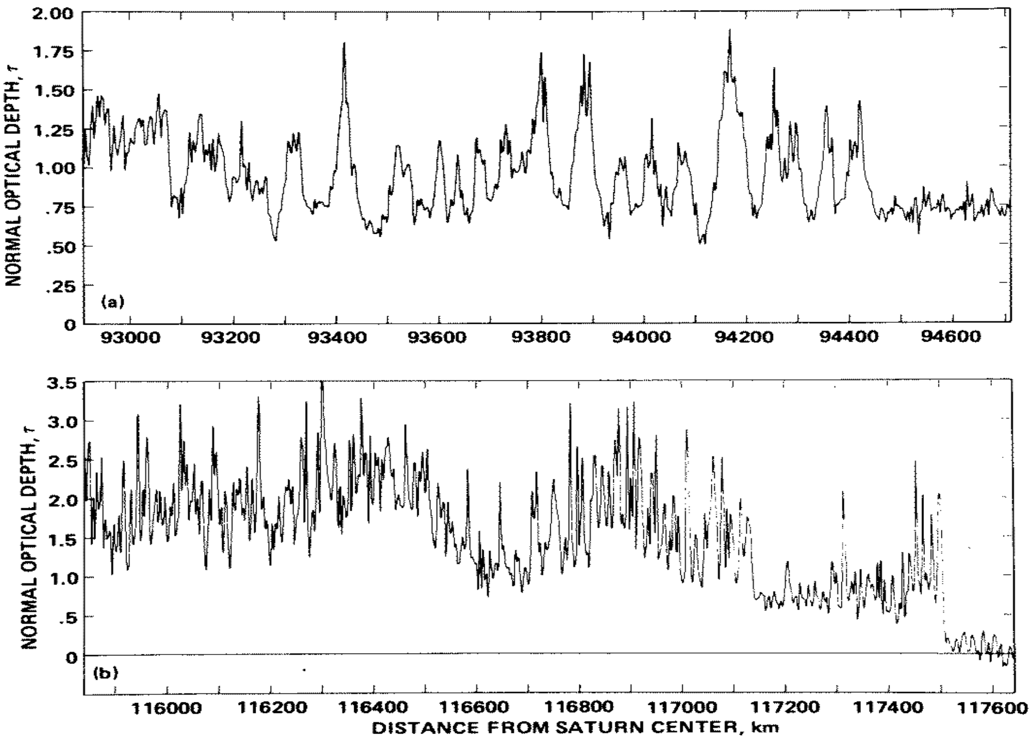

Figure 1.5: *Optical depth profile of the B ring from the Voyager ultraviolet spectrometer stellar occultation (UVS) data, taken from Cuzzi et al. (1984).*

in the B ring, and fig (1.6) showing Voyager 2 images of the inner and outer parts of the ring].

The comparison of multiple optical depth profiles of the Saturnian rings in Nicholson et al. (2000), obtained over a time span of 9 years, shows very little temporal variation of the structure larger than about 20 km. Almost all of the detected differences could be attributed to previously known non–axisymmetric features such as resonance induced bending and inclination waves (Nicholson et al., 2000). Smaller scale structure lies below the resolution limit of the occultation experiment reported in that study, mainly caused by the finite angular diameter of the observed star (Sgr 28, in this case).

As mentioned above, the rings also show a radial variability in color (Cuzzi et al., 1984; Estrada & Cuzzi, 1996), possibly indicating a variation in the size distribution, the composition, or the surface structure of the ring particles. These color variations are in some parts of the ring weakly correlated to the optical depth profile (Estrada & Cuzzi, 1996; Cuzzi & Estrada, 1998).

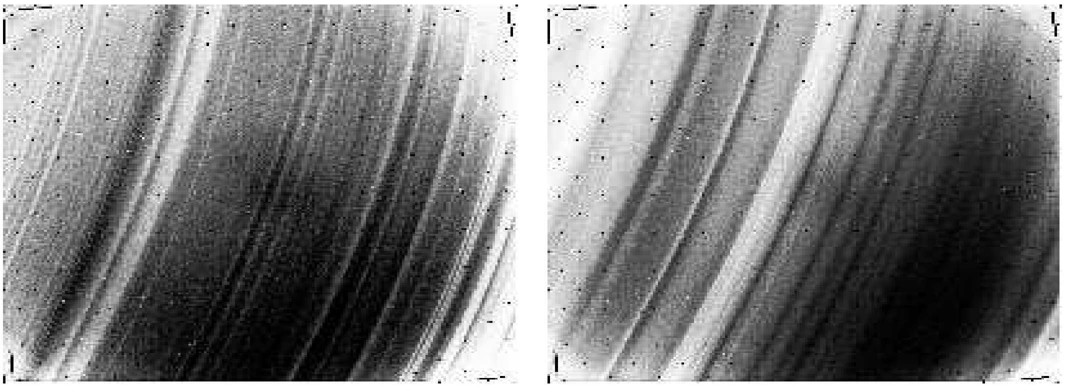

Figure 1.6: *Images of the inner part of the B ring (left, between Saturnocentric distances* 95, 550 *and* 99, 050 *km) and the outer part (right,* 107, 400 *to* 110, 900 *km) from the Voyager 2 narrow angle camera.*

1.2 Models for the B Ring Structure

"Der Mechanismus der erzeugenden Bewegung des Ringes führet auf eine Bestimmung, die denselben, vermittelst eben der Ursachen, die ihn zerstören sollen, in einen sichern Zustand versetzet, dass er in etliche concentrische Zirkelstreifen getheilet wird, welche wegen der Zwischenräume, die sie absondern, keine Gemeinschaft mehr unter einander haben. ... Diese Muthmassung vergnüget mich nicht wenig, vermittlest der Hoffnung, selbige noch wohl dereinst durch wirkliche Beobachtungen bestätigt zu sehen."

"The mechanism for creating the motion of the ring leads to a stable state for the same reasons that would lead to its disintegration; this state is reached by the ring being split into a few concentric circular bands which lose contact with each other because the gaps between them are separated. ... I expect – and this gives me great satisfaction – that the actual observations somehow will confirm my assumption."

—Immanuel Kant, *Allgemeine Naturgeschichte und Theorie des Himmels, 1755*

In this section models for the formation of radial structure in a dense ring are outlined that have been proposed in the literature.

Viscous instability
The first model proposed in the literature (Ward, 1981; Lin & Bodenheimer, 1981; Lukkari, 1981) is the so called viscous instability or diffusion instability. The condition for this instability is that the *dynamic* shear viscosity in the rings shall decrease with increasing density. In this case a small density undulation would be amplified since the regions with lowered density would heat up through the higher viscosity there, compared to zones with enhanced density. The result was a migration of particles from rarefied to denser regions. The stability criterion for viscous instability will be re-derived in chapter 2 together with the condition for overstability.

In the beginning of the 80's this mechanism looked very promising to be the origin for the B ring structure. Theoretical work (Goldreich & Tremaine, 1978a) resulted in an explicit expression for the *kinematic* viscosity in planetary rings, i.e. in a central gravity field

$$\nu = \frac{c^2}{\pi\Omega}\frac{\tau}{1+\tau^2} \,. \tag{1.5}$$

Based on this expression a decrease of the dynamic viscosity $\nu\tau$ for increasing τ could be understood for high optical depths if the velocity dispersion c was itself a decreasing function of the optical depth. In a system of inelastic particles $\partial c/\partial\tau < 0$ is possible since then an increased density, leading to an increased collision frequency, would enhance the collisional cooling, and thus, reduce the dynamic viscosity together with the velocity dispersion. This is basically the argument presented by Lin & Bodenheimer (1981). Such an amplification of density fluctuations was also observed in simulations (Lukkari, 1981), albeit under restricted conditions.

However, later theoretical work (Shukhman, 1984; Araki & Tremaine, 1986) stressed the importance of contributions to the viscosity due to the finite particle volume, the so called collisional or nonlocal transfer of momentum. This nonlocal viscosity is even the dominant part in dense rings, where the structure is best seen, and most importantly it prevents the total momentum transfer to decrease with enhanced density. The viscosities have also been determined in direct N–particle simulations of planetary rings under various conditions, confirming the importance and the effect of the nonlocal viscosity (Wisdom & Tremaine, 1988; Salo, 1991) and it was confirmed that $\partial(\nu\tau)\partial\tau > 0$. Thus, the viscous instability seems to be ruled out as an explanation for the observed structure in the rings.

Embedded moonlets

The presence of a large body, say hundred meters to kilometers in size, would induce a characteristic structure in an otherwise uniform ring of meter sized or smaller particles. Since the three body gravitational interaction with the central planet leads to an effective repelling force between such an embedded moonlet and a ring particle, the moonlet tends to clear a gap around its orbit. It was concluded by Hénon (1981) that the radial structure of the B ring might be attributed to various moonlets orbiting within the ring. The same idea was employed by Lissauer et al. (1981) to model the formation of density features in the Cassini Division and a possible significance of the process was conjectured also for the B ring structure.

The prominent example of the opening of a gap in the rings by an embedded body is the orbiting of the moon Pan in the Encke Division in the outer A ring, which was predicted theoretically (Cuzzi & Scargle, 1985; Showalter et al., 1986) and later on detected in the Voyager images (Showalter, 1991). A kinematic model for the scattering of the ring particles by an embedded moonlet is described in Spahn & Wiebicke (1989) and implications for the optical depth profile in Spahn & Sponholz (1989). The inclusion of viscosity in the model, promoting the closure of the gap that the moonlet opens, is considered in Spahn & Sremčević (2000).

However, there are no clear gaps visible in the optical depth profile of the B ring. The optical depth is almost everywhere larger than about 0.6 in the inner B ring and even larger than 1 in the outer two thirds of the B ring. Structures of the size of tens to hundreds of kilometers cannot be produced by Moonlets that are to small to even clear a gap. Still, it seems probable that part of the observed smaller scale optical depth fluctuations, not visible in the images, are caused by smaller moonlets less then a kilometer in size. Such bodies would form a local density depletion, inclined with respect to the tangential direction (Spahn & Sremčević, 2000).

Ballistic transport
Like all objects in space that are not shielded by an atmosphere planetary rings are subject to a steady bombardment with micro–meteoroids (Cuzzi & Durisen, 1990). The impact speeds can be as high as 20 km/s, so that even micron–sized impactors lift a considerably large mass, the ejecta, from the body they hit. The ejected material would follow nearly Keplerian trajectories[1], eccentric and inclined to the ring plane. The descending node of these orbits lies in most cases again in the dense rings, so that the probability of re–absorption is high. Ballistic transport is the net radial transport of mass and angular momentum caused by meteoroid–impact ejecta that are re–absorbed by neighboring ring regions (Durisen, 1984; Durisen et al., 1989; 1992).

The amount of mass ejected from a given radial zone of a planetary ring, that is not too dense, should be (roughly) proportional to the surface density, so that a given small radial density undulation would grow if it has a wavelength that equals the typical radial throw distance of the ejected material. This process can be modeled with hydrodynamic equations where source and sink terms for mass and momentum are added to the continuity and Navier–Stokes equations, respectively. A stability analysis of these equations (Durisen et al., 1996) predicts the growth of perturbations on a 100 km scale in ring regions with $\tau < 1$. This is in agreement with the observation of a (weak) preference of a 100 km length–scale in the structure in the inner B ring (Horn & Cuzzi, 1996). The minimum e–folding time of the instability is about 10^5 years for $\tau \sim 0.5$. The model cannot account for the formation of structure in the outer two thirds of the B ring, where the optical depth is about $\tau = 2$. At too high optical depth the formation of structure by ballistic transport becomes quite ineffective since the density dependence of the production of ejected material saturates and also the smoothing by viscous diffusion should be faster than the formation of the structure. A basic problem of the model is the lack of such a 100 km structure in the C ring ($\tau \sim 0.5$), which should form there as well, when this effect works in the inner B ring.

A success of the ballistic transport model is the correct prediction of similar characteristic features in the optical depth profile at the inner edges of the A and B rings (Durisen et al., 1992). In both cases there are linear ramps in the optical depth on the lower τ side with radial width in the order of 1000 km, then a sharp edge with an increase of τ from 0.2 to about 1, followed by a maximum in optical depth at the inner edge of the respective ring [see fig (1.3)].

Electromagnetic angular momentum transport
When *larger* meteoroids hit the rings, it is plausible to assume that a part of the produced material in form of small dust grains will be charged and levitated in the Saturnian magnetosphere (Goertz et al., 1986; Goertz & Morfill, 1988). In particular, small charged grains will feel a torque caused by the Saturnian magnetic field, which is rotating uniformly with Saturn's spin rate. In this way the stream of these small dust grains re–impacting the rings can transport a considerable amount of angular momentum from Saturn's rotation to the rings. Similar as in the ballistic transport instability this process can amplify density undulations that have a particular relation with the typical hopping distance of the levitated charged dust. However, in contrast to the ballistic transport mechanism, here the amplification of a given structure is rather attributed to the angular momentum deposition than to the mass transport. The characteristic wavelength favored by the model is in this case

[1]The dynamics of micron–sized ejected grains would be perturbed by a variety of non–Keplerian forces: The magnetic field of Saturn, solar radiation pressure, solar gravity, and drag forces as the plasma drag and Poynting–Robertson drag (Grün et al., 1984; Hamilton & Krivov, 1996).

several hundred kilometers which could account for part of the structure in the outer part of the B ring (Horn & Cuzzi, 1996).

The effect of plasma production in a larger sized meteoroid impact in the rings offers also an explanation for the so called spokes phenomenon (Grün et al., 1983), an azimuthal variation in the ring's brightness of a duration of several hours. Also, this model predicts a minimum of the rings surface density slightly outside the co–rotational radius (the radial distance from Saturn where the Keplerian angular velocity coincides with the angular velocity of the planet's spin). The flow of charged grains is always directed away from this radius, since here the Lorenz force reverses sign. This minimum is really observed in the optical depth profile [see fig (1.3)], although less pronounced than predicted by the model (Shan & Goertz, 1991). Also, the model implies that the minimum actually lies only about 10 km outward the co-rotational radius, the outward displacement attributed to viscous effects. The actual displacement is roughly 2000 km, indicating perhaps an underestimation of the ring viscosity in Shan & Goertz (1991) who indeed neglected the non–local part of the shear viscosity in their model, which should exceed the local part (Salo et al., 2000b) for optical depths as high as in the outer parts of the B ring ($\tau \sim 2$). However, a larger viscosity would also lead to a considerable increase of the characteristic growth times of that electromagnetic transport instability or even prevent it at all.

An interesting feature of the model proposed in Shan & Goertz (1991) is the prediction of a radial variation in particle size.

In general, there are large uncertainties in some of the parameters of this model as well as the ballistic transport model. These are for instance the impact rates of meteoroids of different populations, their velocity and mass distribution, but also the amount of ejecta they produce, with their typical mass and velocity distribution. The latter are also sensitive to the poorly known surface properties of the ring particles.

Viscous overstability

A decrease of the dynamic viscosity with increasing density as required for viscous instability is apparently not given in the Saturnian rings (Araki & Tremaine, 1986; Wisdom & Tremaine, 1988). Rather the opposite behavior is found, namely an increase of viscosity with density. In this case Keplerian shear flow may be subject to an instability of the oscillatory hydrodynamic modes. Then the restoring forces in the compressed phase of the oscillation are so strong that the system overshoots the previous expanded phase at the other side of equilibrium and the amplitude of oscillations starts to grow. It is this "overshooting" that led to the, somewhat counterintuitive, naming "overstability"[2]. From a dynamical point of view the onset of overstability is a Hopf bifurcation, the real parts of a conjugate complex pair of eigenvalues of the Jacobian matrix of the dynamical equations becoming positive.

Viscous overstability has been investigated in the context of accretion disks (Kato, 1978; Blumenthal et al., 1984) and in narrowly confined planetary rings (Papaloizou & Lin, 1988; Longaretti & Rappaport, 1995; Mosqueira, 1996) and in the interplay with nonlinear spiral density waves (Borderies et al., 1985; 1986). The possible significance for the formation of radial structure in the dense Saturnian rings was pointed out in Schmit & Tscharnuter (1995) and Schmit & Tscharnuter (1999). The hydrodynamic model proposed in these papers predicts the growth of radial undulations in density and radial and tangential velocity in the rings on scales larger than about 100 m. As discussed in Schmit & Tscharnuter (1999) the development of the overstable perturbations in the nonlinear regime may lead to the formation of structure on larger scales. Also, a spatial variation of the nonlinearly saturated

[2] It seems that this naming can be traced back to Sir Arthur Eddington [Chandrasekhar (1981), p3].

amplitude of the oscillations is reported in that study.

A non–isothermal hydrodynamic model for viscous overstability in Saturn's B ring is subject of chapter 3 of this thesis and a comparison to direct local simulations of a dense planetary ring is given in chapter 5.

Chapter 2

Hydrodynamic Model for a Planetary Ring

Hydrodynamic modeling is one of the basic approaches to the theoretical description of astrophysical disks, such as galactic disks (Toomre, 1964; Julian & Toomre, 1966; Goldreich & Tremaine, 1978b; Binney & Tremaine, 1987), accretion disks (Lynden-Bell & Pringle, 1974; Kato, 1978; Papaloizou & Lin, 1989; Blumenthal et al., 1984; Debrulle & Knobloch, 1992; Kleiber & Glatzel, 1999), and planetary rings (Stewart et al., 1984; Shu et al., 1985a; Shu et al., 1985b; Schmit & Tscharnuter, 1995; 1999). In spite of many similarities in the appearance of these disk systems, however, there are crucial differences in the physical conditions, and the typical scales. These differences substantiate in the specific hydrodynamic model. So, for instance in galactic dynamics physical collisions can be neglected, the flow is often treated as inviscid[1] and the self–gravity of the disk is of great importance as compared to the gravitational influence of a central region. Usually, in hydrodynamic models of galactic disks and planetary rings the system is considered as isothermal. In hot accretion disks this is not possible, also the flow may become turbulent, the matter hot and ionized. The material, depending on the local opacity of the disk, may also couple to the radiation field, leading to significant contributions to the pressure and temperature (Blumenthal et al., 1984; Kley et al., 1993). Magnetic fields may influence the stream of matter, the model equations are those of magneto-hydrodynamics (Balbus & Hawley, 1991; 1996; Rüdiger et al., 1999; A. Drecker, 2000).

The interest of this thesis is focused on dense collision–dominated planetary rings, as the Saturnian B ring, and the effects of an inclusion of the energy balance equation. Thus, the situation for hydrodynamic modeling is very similar to the one met in the theory of rapidly sheared flow of granular matter: The flow consists of macroscopic particles that collide inelastically, where the energy loss in the random motion of the particles is counter-effected by the input of energy due to viscous shear from the collective motion. In granular flows on earth, energy balance can only be achieved temporarily, as is the case in the description of avalanche dynamics, and the dynamics of chute flows. The granular flow comes eventually to rest and undergoes a transition from fluid like behavior to a solid like state of the system. In contrast, for the investigation of the processes in the rings that are of interest here, the basic flow of the ring can be considered as stationary[2]. The important difference of a

[1] Besides a possible gas component in the model that would lead to an effective viscosity.

[2] Besides a steady inward drift of the mass of the planetary ring towards the central planet on a secular time scale of about 10^8–10^9 years. This drift is caused by the permanent flow of energy from collective motion in the central gravity field to the random motion of the particles in the ring via viscous shear. The random

planetary ring as compared to granular matter flow in a quasi–stationary state is the motion in the central gravity field, leading to qualitative differences in the transport properties of the system.

The dynamics of granular matter are theoretically described in terms of kinetic theory, based upon a kinetic equation of Boltzmann or Enskog type (see appendix A). By computing moments of this kinetic equation the balance laws of mass, momentum, and energy for the system are derived, usually referred to as the hydrodynamic approximation, in a similar manner as for ordinary hydrodynamics (Huang, 1963) but with the Enskog correction due to the final particle volume (Résibois & De Leener, 1977; Chapman & Cowling, 1970). These equations can be closed through the constitutive equations that relate the fluxes of momentum and energy to the gradients of velocity and temperature in the system. Kinetic theory then gives explicit expressions for the transport coefficients in terms of the density and the temperature by deriving an approximate solution for the one particle distribution function that is in general assumed to be nearly the Maxwell–Boltzmann distribution (Chapman & Cowling, 1970). For granular matter the transport coefficients are in general depending on the inelasticity of the particles (Lun et al., 1984; Jenkins & Richman, 1985)(see appendix B). The hydrodynamic approximation for granular matter has its difficulties of its own:

- There is **no scale separation** over orders of magnitude as in fluid dynamics between the microscopic and mesoscopic scales given by the molecular diameter and the mean free path and the typical size of the variations of the macroscopic fluid properties. Closely related is the problem of the definition of a thermodynamic limit for granular systems: In general neither the particle number nor the system size can be considered to a good degree of approximation as infinitely large.

- There is theoretical evidence (Sela & Goldhirsch, 1998) that the **Navier–Stokes order is not sufficient** for granular matter in a solution scheme for the one particle distribution function as the Chapman–Enskog method. Hydrodynamic equations in the next order of that method, the Burnett order, have been derived for granular matter by Sela & Goldhirsch (1998), but computations with their complicated relations are bookkeeping. Further, the authors argue that the Burnett equations themselves are mathematically ill–posed (Bobylev, 1984).

- Usually, when deriving constitutive equations for granular matter (Lun et al., 1984; Jenkins & Richman, 1985; Brey et al., 1996; Sela & Goldhirsch, 1998) the **assumption of a small dissipativity** of the grain collisions is made, i.e. the approximate solutions for the one particle distribution function arise from a perturbation expansion about the elastic hard sphere gas for small inelasticity. So the theories can not be applied to systems of grains which collide even moderately dissipatively.

- In general the constitutive relations and transport coefficients for granular hydrodynamics are based on the **assumption of a velocity independent coefficient of restitution**, where the coefficient of restitution measures the damping of the relative velocity that two grains suffer in a collision. However, it is clear from collision experiments (Raman, 1918; Bridges et al., 1984) and from theoretical modeling (Kuwabara &

motion is dissipated in inelastic collisions to internal heat of the particles via plastic and viscoelastic energy dissipation. On the same time scale the conserved angular momentum requires a spreading of a fraction of the disk. So eventually the bulk of the mass of a collision–dominated ring will fall on the central planet while a small fraction of the particles forms a wide–spread disk carrying all the initial angular momentum of the system (Lynden-Bell & Pringle, 1974).

Kono, 1987; Brilliantov et al., 1996; Morgado & Oppenheim, 1997) that the coefficient of restitution is a monotonic decreasing function of the impact velocity.

In spite of such problems hydrodynamic theory is successfully used in investigations of rapidly sheared granular material, as in avalanche dynamics (Hutter, 1996; Savage & Hutter, 1989), size segregation in flows (Jenkins & Mancini, 1989; Arnarson & Willits, 1998), the investigation of instabilities in (force free) granular shear flow (Hopkins & Louge, 1991; Savage, 1992; Alam & Nott, 1998), but also in the description of granular cluster formation (Goldhirsch & Zanetti, 1993; Petzschmann et al., 1999; Spahn et al., 1997). The applicability of a hydrodynamic modeling for granular flows has to be verified carefully for the particular case under consideration. Positive indications are for instance a high collision frequency compared to the shear rate and the smoothness of the system, in the sense that the scale of variations of the state variables is small compared to the mean free path.

A hydrodynamic theory for granular flow under Keplerian shear inherits the problems arising in the force free case. For instance, the dissipativity of the collisions in a planetary ring is probably not small (Bridges et al., 1984). For a given surface density of the ring there exists an upper limit for the coefficient of restitution for which a disk can be energetically stable (see section 2.2). For moderately dense rings this critical restitution is considerably smaller than a validity of the transport coefficients of granular kinetic theory would require. Also, the velocity dependence of the coefficient of restitution affects the energy equilibrium of the ring. Although such an equilibrium can be achieved with a velocity independent coefficient of restitution, and many crucial phenomena are covered in this approximation, a velocity dependent restitution is realistic (Bridges et al., 1984). In the theory of planetary rings hydrodynamical modeling usually concentrates on the balances of mass and momentum, assuming that the disk is in a *uniform* equilibrium of viscous heating and collisional loss of energy (Stewart et al., 1984). In this sense the 'granular' aspect of the flow influences the dynamics of the model only indirectly. Such hydrodynamic models have been used to investigate the stability of the rings (Lin & Bodenheimer, 1981; Ward, 1981; Schmit & Tscharnuter, 1999) or to study satellite induced waves (Shu, 1984; Shu et al., 1985a; Shu et al., 1985b).

An additional difficulty is met in the hydrodynamic modeling of a planetary ring: for a ring particle moving in the central gravity field the mean free path is restricted by its epicyclic motion. This is similar to the situation of a charged particle moving in a magnetic field on Larmor circles. This fact can be more easily taken into account in a kinetic description of the N–particle dynamics (Goldreich & Tremaine, 1978a; Shukhman, 1984; Araki & Tremaine, 1986). On the hydrodynamic level this will lead to considerable deviations in the transport processes, since the mean free path is of crucial influence here. The deviations are expected to be large at low densities, where the particles collide a few times per orbital period or even less, and smaller at large density, in particular in self–gravitating systems, where a particle collides frequently with others within one orbit. Therefore, the transport coefficients derived for granular systems without volume forces are in general not applicable for the modeling of a planetary ring. In this thesis another approach is followed: the values for the transport coefficients, the equation of state, and the collisional cooling function are determined directly from simulated ring systems (Salo et al., 2000a) and used in the linear stability analysis of the hydrodynamic equations. This has the advantage that the effects of epicyclic motion and of a velocity dependent restitution on the transports are naturally included in the analysis. This method provides also a test for the applicability of a Newtonian ansatz for the stress tensor in this system.

2.1 Basic Equations

The ring is described as a thin, self–gravitating viscous fluid disk, consisting of inelastic, uni–sized, smooth, spherical particles. The mean fields of density ϱ, velocity $\vec{u}$, and granular temperature T are supposed to obey the hydrodynamic balance laws for mass, momentum, and energy. A motivation of these balance laws from kinetic theory is given in appendix A, where also the generalizations due to the close packing of a dense system of macroscopic particles are discussed, as well as the inclusion of the inelasticity of the collisions.

The granular temperature is defined for an ensemble of particles of one unit mass in terms of the energy of the random motions as an average in terms of the one–particle distribution function (appendix A) as

$$T = \frac{1}{3}\left\langle (\vec{v}-\vec{u})^2 \right\rangle ,$$

where $\vec{v}$ is the peculiar velocity of the particles. The energy balance contains a cooling term Γ, typical for granular matter, that accounts for the steady dissipation of energy of the motion due to the inelastic collisions of the ring particles. With the pressure tensor $\widehat{P}$ and the heat flux vector $\vec{q}$, the gravitational force field $\vec{F}$ of the central planet, and the disk's mean field self–gravity potential ϕ the balance equations read

$$(\partial_t + u_\alpha \nabla_\alpha)\varrho = -\varrho \nabla_\alpha u_\alpha \tag{2.1}$$
$$\varrho(\partial_t + u_\alpha \nabla_\alpha) u_\beta = \varrho F_\beta - \varrho \nabla_\beta \phi - \nabla_\alpha \widehat{P}_{\alpha\beta} \tag{2.2}$$
$$\frac{3}{2}\varrho(\partial_t + u_\alpha \nabla_\alpha) T = -\widehat{P}_{\alpha\beta}\nabla_\alpha u_\beta - \nabla_\alpha q_\alpha - \Gamma \,, \tag{2.3}$$

where a sum over repeated indices is understood. In what follows a Cartesian coordinate system will be used. The thermodynamic fluxes of momentum ($\widehat{P}$), and energy ($\vec{q}$) may both contain collisional contributions that arise in dense systems (see appendix A). The fluxes are related linearly to the gradients of the state variables via the constitutive equations, i.e. the Newtonian ansatz for the pressure tensor

$$\widehat{P}_{\alpha\beta} = p\delta_{\alpha\beta} - 2\eta \widehat{D}_{\alpha\beta} - \xi \nabla_\mu u_\mu \delta_{\alpha\beta} \,, \tag{2.4}$$

and Fourier's law for the heat flow

$$q_\alpha = -\kappa_D \nabla_\alpha T \,. \tag{2.5}$$

The dynamic shear and bulk viscosity and the dynamic heat conductivity are denoted by η, ξ and κ_D respectively, and $\widehat{D}$ is the traceless shear tensor.

$$\widehat{D}_{\alpha\beta} = \frac{1}{2}(\nabla_\alpha u_\beta + \nabla_\beta u_\alpha - \frac{2}{3}\delta_{\alpha\beta}\nabla_\lambda u_\lambda) \,. \tag{2.6}$$

The disk's self–gravity potential is related to the mass density by Poisson's equation

$$\nabla^2 \phi = 4\pi\, G\, \rho \,. \tag{2.7}$$

The central gravity force per unit mass $\vec{F}$ by a planet of mass M is

$$\vec{F} = \vec{\nabla}\frac{GM}{\sqrt{r^2+z^2}} = -\vec{e_r}\Omega^2 r \left(1 + O(z/r)^3\right) - \vec{e_z}\Omega^2 z \left(1 + O(z/r)^2\right) \,, \tag{2.8}$$

with Newton's gravitational constant G and the Kepler frequency $\Omega = \sqrt{GM/r^3}$ at radius r. Orders of $(z/r)^2$ are neglected, since r is about 10^8 m, while the main rings of Saturn have a vertical extension of 100 m at most. For the investigation of the local dynamics of the particles in the rings it is often convenient to use a Cartesian coordinate system centered at a radial distance r_0 of the central planet. If $\vec{x} = (x, y, z)$ is the position vector in that coordinate system, where the z–axis points along the spin axis of the ring, and x in radial direction away from the planet, the linearized gravitational force in that frame reads

$$\vec{F} = -\vec{e_x}\left(\Omega_0^2 r_0 - 2\Omega_0^2 x\right) - \vec{e_z}\Omega_0^2 z - \vec{e_y}\Omega_0^2 y\,, \tag{2.9}$$

where orders of x/r_0 and z/r_0 are neglected. If the Cartesian frame is additionally rotating around the planet at distance r_0 with Kepler frequency $\Omega_0 = \sqrt{GM/r_0^3}$ the Coriolis and centrifugal forces have to be added

$$\vec{F} = \vec{e_x}3\Omega_0^2 x - \vec{e_z}\Omega_0^2 z - 2\Omega_0\vec{e_z} \times \vec{u}\,. \tag{2.10}$$

2.2 Example: Vertical Structure

An illustrative example for the application of hydrodynamic modeling to planetary rings is the derivation of vertical density profiles for the ring. From a comparison to results from balance laws derived in terms of kinetic theory (Simon & Jenkins, 1994) and molecular dynamics simulations (Wisdom & Tremaine, 1988; Salo, 1991) one can learn about advantages and limitations of the granular hydrodynamic description.

Energy balance of a planetary ring

The energy budget of a planetary ring in a stationary state requires the cancellation of the rate of viscous energy transfer $\dot{E}_\nu$ from the systematic shearing motion to the ring particles' random motion and the loss rate of energy $\dot{E}_{coll}$ by the inelastic collisions. Both contributions may depend in general on the optical depth τ [eq (1.3)] and the velocity dispersion of the system.

An important quantity affecting this balance is the collision frequency ω_c. The collision frequency for particles with cross section πR_p^2 at mass density ρ and velocity dispersion c may be estimated as follows. The number of collisions per particle ΔN in the time interval Δt is approximately

$$\Delta N = \pi R_p^2 \frac{\rho}{m_p} c\Delta t\,. \tag{2.11}$$

This implies for the collision frequency of a thin ring with scale height $H = \sigma/\rho$

$$\omega_c \approx \frac{\Delta N}{\Delta t} = \frac{\pi R_p^2}{m_p}\frac{\sigma}{H}c\,. \tag{2.12}$$

Inserting for the scale height $H = c/\Omega$ [see eq (1.4)] yields the estimate

$$\omega_c \approx \Omega\tau\,. \tag{2.13}$$

This estimate does not include the reduction of the effective volume by the particles' proper volume. This effect becomes important for large optical depth [see fig (4.10), lower left plot, for a result obtained from simulations].

Summarizing in a heuristic way (Stewart et al., 1984) the argumentation of Goldreich & Tremaine (1978a) two limiting regimes for the mean free path l of the ring particles can be combined in a single formula for the kinematic viscosity $\nu \equiv \omega_c l^2$. For high optical thickness the particles collide frequently in one orbital revolution and the mean free path is $l = c/\omega_c$. For low optical thickness the collision frequency may be small compared to the orbital frequency. In the latter case the mean free path is restricted rather by the epicyclic length $l = c/\Omega$. Both limiting cases are combined in the formula for the viscosity

$$\nu = \frac{\omega_c c^2}{\Omega^2(1+\tau^2)} \tag{2.14}$$

The viscous gain rate of energy is then

$$\dot{E}_\nu \equiv \nu \left(r\frac{\partial \Omega}{\partial r} \right)^2 \approx \frac{9}{4} \frac{\omega_c c^2}{(1+\tau^2)} \,. \tag{2.15}$$

The dissipation rate can be estimated following again the heuristic arguments of Stewart et al. (1984). The coefficient of restitution ϵ is the measure for the damping of the normal component of the relative velocity in a collision [eq (A.10)]. The magnitude of the relative velocity is typically of the order of the velocity dispersion c, and thus, the energy loss in one collision is approximately $(1-\epsilon^2)c^2$. Then the energy loss rate is given by

$$\dot{E}_{coll} \approx \omega_c c^2 (1-\epsilon^2) \,. \tag{2.16}$$

A stationary state is only achieved if gain and loss balance, i.e.

$$\left(1-\epsilon^2\right)\left(1+\tau^2\right) = b \,, \tag{2.17}$$

where b is a constant of order unity. This formula does not depend on the velocity dispersion c if ϵ is velocity independent, since in these simplified considerations both, energy loss and gain, have the same dependence on c. For a given value of this constant restitution, equilibrium exists only for one particular value of the optical depth. If ϵ is too high, the simulated system is unstable since it constantly heats up and vice versa, if ϵ is too low the system cools down monotonically. An explicit dependence of the energy balance condition on velocity dispersion, and hence a defined steady state temperature, is established in physically more realistic models: First, the coefficient of restitution in realistic impacts is a decreasing function of impact velocity (Bridges et al., 1984), thus the energy loss will be small in cold systems, they tend to heat up, and large in hot systems that tend to cool down. In between the system attains a stable equilibrium steady state temperature. Second, gravitational interactions between particles would correspond to totally elastic collisions. Thus, the monotonic collisional cooling when ϵ is too low should be slowed down and stopped by gravitational scattering that becomes more efficient in a colder system. Third, when the system cools down it flattens and the local density increases. At high density the particle diameter may no more be small compared to the mean free path, and in addition to the viscosity (2.14) the nonlocal transport of momentum becomes important. Local and nonlocal parts of the the kinematic viscosity are pictured in fig (4.10) and (4.11) determined from local molecular dynamics simulations of a planetary ring with different optical depths. The nonlocal contribution may establish a minimum velocity dispersion of the order $R_p\Omega$. In this energy equilibrium the system's collision frequency may exceed considerably the value of the simple estimate (2.13).

Examples from non–selfgravitating simulations with constant coefficient of restitution are shown in fig (2.1) where the time development of the temperature of simulated rings with fixed optical depth $\tau = 0.4$ but different coefficients of restitution is plotted. The prediction of eq (2.17) is qualitatively confirmed. The particular value for ϵ that leads to a steady state for $\tau = 0.4$ seems to be near 0.7. Of course this steady state is unstable, since the true (ϵ, τ)–pair can never be established exactly. For a higher ϵ the simulated system constantly heats up, for a lower ϵ it cools[3]. The equilibrium that is eventually reached in

[3]The energy input in the simulations comes over the periodic boundaries. See chapter 4 for a brief description of the simulation method

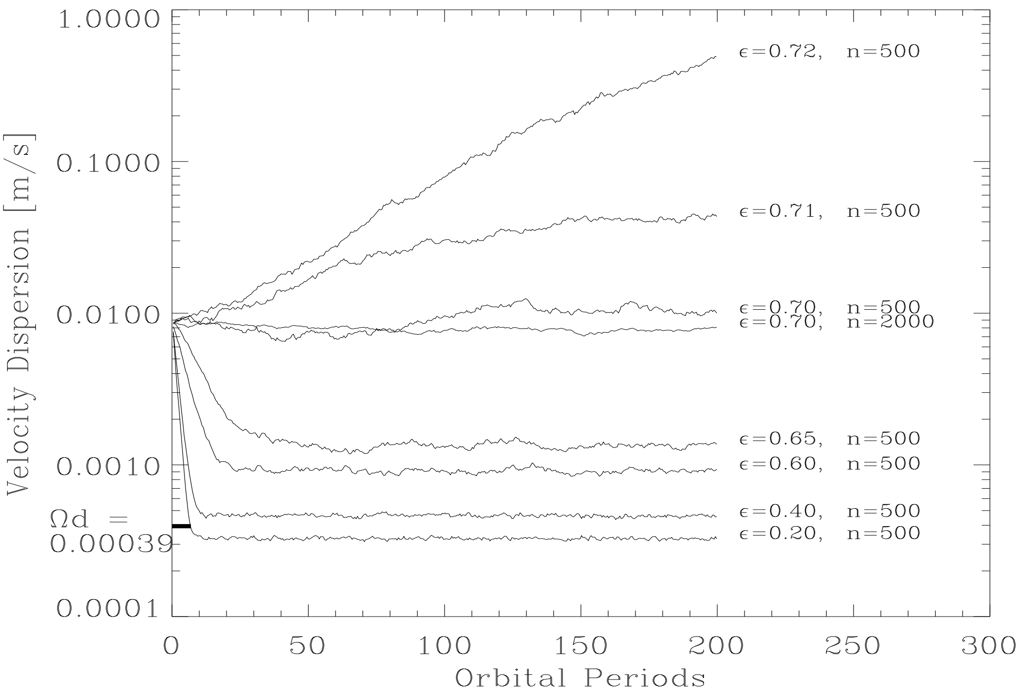

Figure 2.1: *Time development of the scalar velocity dispersion in simulations for various values of the coefficient of restitution. The optical depth is fixed (here $\tau = 0.4$).*

the latter case is due to the additional viscous gain by the nonlocal viscosity.

Vertical density profiles

In this paragraph the vertical density profiles of simulated rings near the local energy balance and in the nonlocal steady state are compared to theoretical profiles. The latter are solutions of the hydrodynamic balance equations or of similar balances that have been derived in terms of kinetic theory (Simon & Jenkins, 1994).

From the hydrodynamic balance laws (2.1) one can obtain the vertical density profiles for a steady ring that is radially and azimuthally uniform, i.e. $\partial_t\{\varrho, \vec{u}, T\} = 0$, $\vec{u} = r\Omega\vec{e_\varphi}$, and density, temperature, pressure, transport coefficients, and granular cooling depend only on z. The balance of momentum and energy then require

$$\begin{aligned} p' + z\Omega^2\varrho &= 0 \\ [\kappa_D T']' + \frac{9}{4}\eta\Omega^2 - \Gamma &= 0\,, \end{aligned} \tag{2.18}$$

while the continuity equation is trivially fulfilled. A prime denotes differentiation with respect to z. The first equation describes the vertical balance of pressure and gravity forces, the second one the vertical balance of heat conduction, viscous heating, and the collisional cooling.

The transport coefficients, the equation of state, and the cooling function Γ have been computed for *dense* rapidly sheared granular flows by Jenkins & Richman (1985). These relations are given in the appendix B and will be used here to determine the vertical stratification predicted by the hydrodynamic equations. Solutions with or without the nonlocal corrections to the transport due to the particles' covolume (see appendix B) are considered separately.

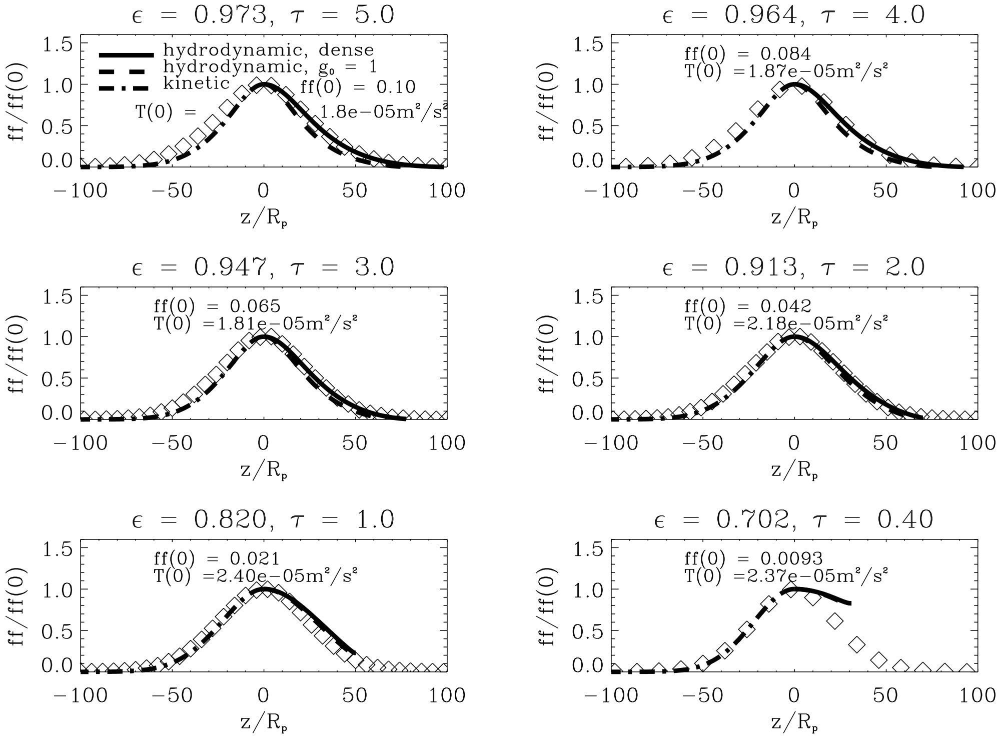

Figure 2.2: *A comparison of density profiles for a planetary ring obtained from simulations (symbols), hydrodynamic equations (2.18) including finite particle volume effects (solid line), without finite particle volume effects (dashed line), and the balance laws (2.19) computed for dilute systems (dash-dotted line).* ff *denotes the filling factor defined as* $\mathit{ff} = \varrho/\varrho_p$. *The systems are near the local equilibrium given by the condition (2.17).* $g_0(\mathit{ff})$ *is the Carnahan–Starling factor (see Appendix B), accounting for finite particle size effects in dense systems. For* $g_0 = 1$ *such effects are excluded.*

In the framework of kinetic theory Simon & Jenkins (1994) investigated the vertical structure of a *dilute* planetary ring. They formulated kinetic balance laws for energy and momentum. This model includes the idea worked out in Goldreich & Tremaine (1978a) that the velocity dispersion in a planetary ring is anisotropic, a tensor of second rank. In contrast to the kinetic balance equations shown in appendix A the distribution function they use is purely Maxwellian but anisotropic (often referred to as 'triaxial'). The vertical components of the momentum and energy balance equations of this approach lead to equations similar to eq (2.18)

$$\begin{aligned} (\mathit{ff}T)' + \lambda(\epsilon) z \Omega^2 \mathit{ff} &= 0 \\ \alpha(\epsilon)\left[T'\sqrt{T}\right]' + \beta(\epsilon)\Omega T \mathit{ff} - \gamma(\epsilon)\mathit{ff}^2\sqrt{T^3} &= 0\,. \end{aligned} \tag{2.19}$$

Here, $T = \frac{1}{3}Tr\{c_\alpha c_\beta\}$ is the trace of the velocity dispersion tensor. The coefficient functions that account for the dependence on the coefficient of restitution are given in the appendix B. Here, $f\!f$ denotes the filling factor defined as $f\!f = \varrho/\varrho_p$ with the particles' material density ϱ_p.

A main difference of eq (2.18) and (2.19) appears in the density dependence of the viscous heating term. When neglecting the finite particle size corrections in η [eq (B.1)] the dynamic viscosity is independent of the density. This is covered qualitatively in the high τ limit of eq (2.14) for the kinematic viscosity $\nu = \eta/\varrho$, where the finite particle size contributions are also excluded. In eq (2.19) the viscous heating is proportional to density, and so it becomes inefficient in low density rings, or more precisely, in low density parts of the ring. This is covered qualitatively in the low τ limit of eq (2.14). In this sense eq (2.14) is an interpolation between the viscous gain terms in the two approaches.

Numerical solutions of eq (2.18) and (2.19) are shown in fig (2.2) subject to the initial conditions

$$T(z=0) = T_0\,, \quad f\!f(z=0) = f\!f_0\,, \quad T'(z=0) = 0\,.$$

The midplane values T_0 and $f\!f_0$ are taken from simulations for rings with (ϵ, τ)–pairs that

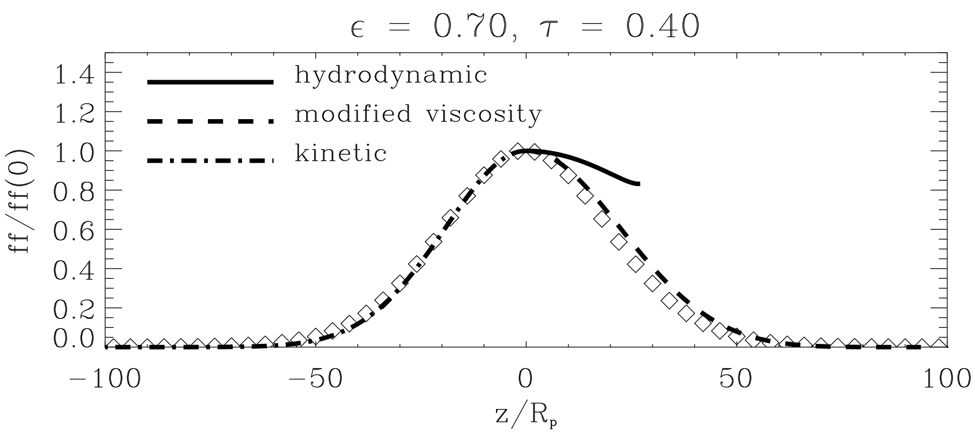

Figure 2.3: *Hydrodynamic (solid) and kinetic profiles (dash–dotted) for a simulation with $\tau = 0.4$. The hydrodynamic balance laws fail to reproduce the simulational profile. A solution of the hydrodynamic equations with a density dependent viscosity (dashed) leads to a good agreement.*

closely match the condition (2.17). The agreement with the simulated profiles is good for the hydrodynamic profiles as well as for the triaxial kinetic ones. A slight improvement is obtained if in the granular hydrodynamic transport coefficients given by eq (B.1, B.2, B.3) and the equation of state [eq (B.5)]) the corrections due to the finite particle volume are taken into account. For rings with lower optical depth the hydrodynamic profiles get worse. The main reason for this is that the hydrodynamic viscosity η stays independent of density while the actual viscous heating in the system does not: As argued above, at low densities the mean free path is restricted by the epicyclic length rather than collisions. In the triaxial kinetic description this is taken into account. This is checked by introducing a cut off for the viscous heating by hand: multiplying the viscosity in equations (2.18) with the filling factor significantly improves the hydrodynamic density profiles [fig (2.3)].

The situation is different for simulated systems that are in nonlocal equilibrium sustained by nonlocal viscous gain. These rings are denser and flatter. Typical examples are shown in fig (2.4) together with the theoretical profiles. Corrections to the transport coefficients and

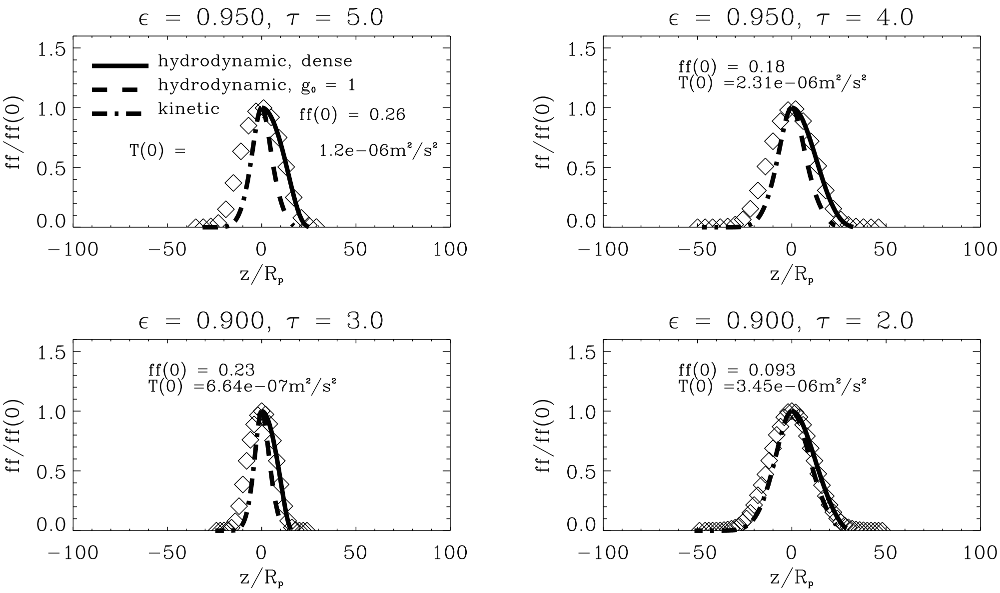

Figure 2.4: *Density profiles for simulated rings in the nonlocal equilibrium. Finite particle size effects, $g_0 > 0$, are important.*

the equation of state due to the finite particle volume, described by the radial distribution function at contact $g_0(\mathit{ff})$ (see Appendix B) are important. The hydrodynamic profiles with the transport coefficients for dilute systems and the triaxial kinetic profiles underestimate the ring thickness, while the hydrodynamic profiles that have been computed with the density corrected transport coefficients give an excellent agreement.

The effect of self–gravity can be approximated in the simulations by an enhancement of the frequency of vertical oscillations in the equations of motion [eq (4.1)] for the particles in the simulation box (Wisdom & Tremaine, 1988) (see also chapter 4). Wisdom & Tremaine (1988) have used a factor $\Omega_z/\Omega = 3.6$ in their simulations. This enhancement factor leads to an increased flattening of the simulated disk, the particles tend to form a mono–layer, and the nonlocal transports get more important. For optical depths larger than about one the system then starts to develop a two–layered sheet [fig (2.5)], and for still higher optical depths more layers are formed (Wisdom & Tremaine, 1988; Salo, 1991). This enhancement of the frequency of vertical oscillations is easily applied to the theoretical balance laws (2.1) replacing Ω in the first equation (momentum balance) by $\Omega_z = 3.6\Omega$. However, the multi-layer structure observed in the simulations can not be reproduced by the vertical hydrodynamic balance equations.

Summary

The hydrodynamic balance laws (2.1) can successfully match the vertical profiles of the stationary state of simulations under certain conditions.

- The system has to be dense. The applicability of **hydrodynamics is restricted to systems with a high collision frequency**, i.e. at high optical depth τ and high filling factors ff.

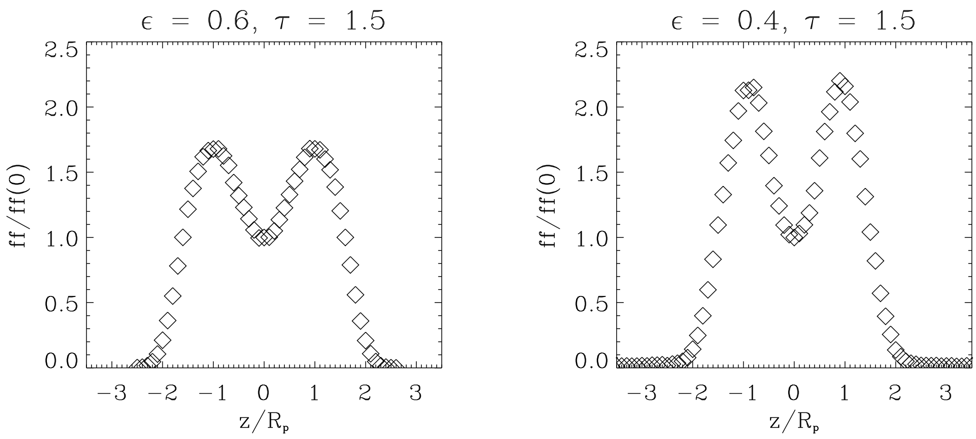

Figure 2.5: *Density profiles for simulated rings with an enhanced frequency of vertical oscillations* $\Omega_z = 3.6\Omega$.

- In this case the **finite particle volume affects the transport processes** and the equation of state and has therefore to be included in the hydrodynamic description.
- The restriction of the granular transport coefficients (Appendix B) to a **coefficient of restitution ϵ near one is problematic** for a realistic description of the ring.
- In the case of an incorporation of the ring's self–gravity by an enhancement of the frequency of vertical oscillations (Wisdom & Tremaine, 1988) the **multi-layer structure cannot be modeled by the hydrodynamic equations** [fig (2.5)].

2.3 Thin Disk Approximation

Very often astrophysical disks are extremely flat. For example, the rings of Saturn have a radial extension of 100,000 km compared to a thickness of 100 m. So the ratio of radial to vertical scale is for such a planetary ring about 10^{-6}, for a typical galactic disk about 0.1, and for a cold accretion disk less than 0.1.

In a highly flattened system it is reasonable to assume that the vertical stratification has a minor effect on the dynamics, if any. Then the hydrodynamic equations (2.1) are often written as balance laws for the ring's surface density and the components of the velocity in the plane, usually referred to as the thin disk approximation in the literature.

These thin disk balance equations can be obtained from the three dimensional ones by integration over the vertical coordinate z, under the assumption of a negligible vertical velocity u_z and z–independent planar components of the velocity. Then the balance laws (2.1) read

$$\begin{aligned} (\partial_t + u_\alpha \nabla_\alpha)\sigma &= -\sigma \nabla_\alpha u_\alpha \\ \sigma(\partial_t + u_\alpha \nabla_\alpha)u_\beta &= \sigma F_\beta - \sigma \nabla_\beta \phi - \nabla_\alpha \widehat{P}_{\alpha\beta} \\ \frac{3}{2}\sigma(\partial_t + u_\alpha \nabla_\alpha)T &= -\widehat{P}_{\alpha\beta}\nabla_\alpha u_\beta - \nabla_\alpha q_\alpha - \Gamma\,, \end{aligned} \tag{2.20}$$

where the indices extends run now only over the planar coordinates. The vertical components of the central gravity and the disk's self–gravity are assumed to have odd parity with respect to the vertical coordinate, the density even parity, and the temperature is assumed not to depend on z. The surface density is defined by

$$\sigma(x,y) = \int_{-\infty}^{\infty} \mathrm{d}z\, \varrho(x,y,z)\,, \tag{2.21}$$

and Γ is the z–integrated cooling. Similarly, in the pressure tensor and heat flux vector

$$\begin{aligned} \widehat{P}_{\alpha\beta} &= p\delta_{\alpha\beta} - 2\eta\widehat{D}_{\alpha\beta} - \xi\nabla_\mu u_\mu \delta_{\alpha\beta} \\ q_\alpha &= -\kappa_D \nabla_\alpha T\,, \end{aligned} \tag{2.22}$$

the quantities p, η, ξ, and κ_D are now z–integrated.

With the density approximated as $\varrho(x,y,z) = \sigma(x,y)\delta(z)$ the 3D Poisson equation for a highly flattened disk reads

$$\nabla^2\phi(x,y,z) = 4\,\pi\,G\,\sigma(x,y)\delta(z)\,. \tag{2.23}$$

For $z \neq 0$ the Laplace equation $\nabla^2\phi = 0$ has to be solved. Assuming the factorization

$$\phi(x,y,z) = f_1(x)f_2(y)f_3(z) \tag{2.24}$$

yields

$$\frac{\partial^2 f_1(x)}{\partial x^2}\frac{1}{f_1(x)} + \frac{\partial^2 f_2(y)}{\partial y^2}\frac{1}{f_2(y)} + \frac{\partial^2 f_3(z)}{\partial z^2}\frac{1}{f_3(z)} = 0 \tag{2.25}$$

which is only possible if each of the terms is constant, e.g.

$$k_x^2 := \frac{\partial^2 f_1(x)}{\partial x^2}\frac{1}{f_1(x)} \tag{2.26}$$

$$k_y^2 := \frac{\partial^2 f_2(y)}{\partial y^2}\frac{1}{f_2(y)} \tag{2.27}$$

$$k^2 := \frac{\partial^2 f_3(z)}{\partial z^2}\frac{1}{f_3(z)} \tag{2.28}$$

under the condition

$$k_x^2 + k_y^2 + k^2 = 0\,. \tag{2.29}$$

The k_i follow from physical arguments. The equations for the f_i can then be integrated, e.g.,

$$f_3(z) = b\exp\{\pm kz\}\,, \quad b = const. \tag{2.30}$$

The physically reasonable choice is a real positive k for $z < 0$ and negative k for $z > 0$. Thus, the function

$$\begin{aligned} \phi(x,y,z) &= b\,f_1(x)f_2(y)\exp\{-k|z|\} \\ &=: f_4(x,y)\exp\{-k|z|\} \end{aligned} \tag{2.31}$$

solves the Laplace equation. It satisfies $\nabla^2\phi = 0$ everywhere except in the ring plane $z = 0$. The Poisson equation affords

$$4\pi G\int_V \mathrm{d}^3r\,\varrho = \int_V \mathrm{d}^3r\,\nabla^2\phi\,. \tag{2.32}$$

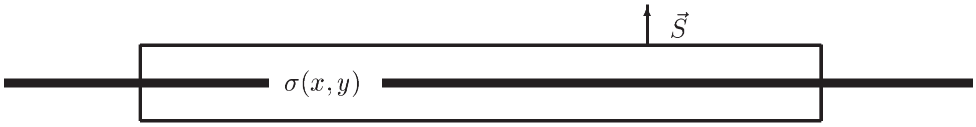

Figure 2.6: *Surface S enclosing a segment of the thin disk with surface density* $\sigma(x,y)$.

With Gausses theorem the surface density $\sigma(x,y)$ can be determined that generates the desired discontinuity in the potential at $z=0$, i.e.

$$\int_V \mathrm{d}^3 r \nabla^2 \phi = \int_S \mathrm{d}^2 \vec{S} \cdot \vec{\nabla} \phi \,. \tag{2.33}$$

The surface of integration S is chosen very close and parallel to the thin disk, as shown in fig (2.6), such that the contributions from $\partial_x \phi$ and $\partial_y \phi$ to the last integral in (2.33) vanish. The normal components of the gradient of the potential (2.31) are at S

$$\begin{aligned} \lim_{z\to 0+} \frac{\partial \phi}{\partial z} &= -k\, f_4(x,y) \\ \lim_{z\to 0-} \frac{\partial \phi}{\partial z} &= +k\, f_4(x,y), \end{aligned} \tag{2.34}$$

thus

$$4\pi G \int_V \mathrm{d}^3 r \varrho = 4\pi G \int_{S_{||}} \mathrm{d}^2 A\, \sigma(x,y) \tag{2.35}$$

and

$$\int_S \mathrm{d}^2 \vec{S} \cdot \vec{\nabla} \phi = 2k \int_{S_{||}} \mathrm{d}^2 A\, f_4(x,y) \,. \tag{2.36}$$

Since this holds for an arbitrary surface S it follows

$$f_4(x,y) = -\frac{2\pi G}{k}\, \sigma(x,y) \,. \tag{2.37}$$

For the purpose of the linear stability analysis of chapter 3, ϕ is the potential of a harmonic perturbation of the surface density of the disk of the form

$$\sigma(x,y) \propto \exp\{i\, n\, x + i\, m\, y\} \,. \tag{2.38}$$

Thus, the conditions (2.26), (2.27), and (2.29) are consistently fulfilled with the identification $k_x \equiv i\, n$ and $k_y \equiv i\, m$ so that finally

$$\phi(x,y,z) = -\frac{2\pi G}{\sqrt{m^2+n^2}}\, \sigma(x,y) \exp\{-\sqrt{m^2+n^2}\, |z|\} \,. \tag{2.39}$$

Chapter 3

Viscous Overstability

In this chapter the hydrodynamic model for the viscous overstability of granular Keplerian shear flow is presented. This is basically an extension of the model of Schmit & Tscharnuter (1995) by the hydrodynamic heat flow equation. The thin disk approximation is employed, in this case the balance laws (2.20) for the vertically integrated state variables and the Poisson equation (2.23). The constitutive equations are the relations (2.22) with the z–integrated transport coefficients.

In section (3.1) the model is investigated for linear stability computing the growth rates of modes of the linearized equations. In section (3.2), similarly as in Spahn et al. (2000), simple estimates of parameters for the dispersion relation of the linear theory are given and the basic stability behavior of the system is discussed qualitatively. In section (3.3) the weakly nonlinear stability of the system is studied in a multiple scale approach deriving a Landau equation for the growth of the amplitude of overstable modes into the nonlinear regime.

3.1 The Non–Isothermal Hydrodynamic Model

3.1.1 Linear Stability

The vertically integrated balance laws (2.20) posses a stationary solution for uniform surface density Σ, temperature T_0, disk self–gravity potential ϕ_0, and for a purely Keplerian velocity field $\vec{U} = -\frac{3}{2}\Omega(r_0)\, x\, \vec{e}_y$, expressed in a frame that rotates at a distance r_0 from the planet with the local Keplerian angular velocity $\Omega(r_0)$, where the x–axis points radially outward and the y–axis in orbital direction. A secular viscous inward drift of the ring particles is neglected as well as the small influence of the planetary oblateness and the disk's self-gravity potential on the orbital frequency. Then the balance laws reduce to the stationary energy balance condition

$$\Gamma = \frac{9}{4}\eta\Omega^2 \,, \tag{3.1}$$

requiring a local cancellation of the collisional cooling and the heating of the random kinetic energy by viscous shear. For a given dissipativity law of the inelastic particle collision this energy balance provides a relation between Σ and T_0 of the stationary state.

Now let the flow be allowed for small perturbations from the stationary state denoted by σ, T, ϕ, and $\vec{u} = (u, v)$. Linearizing and inserting the constitutive relations (2.22) in eq (2.20) the linearized balance equations are obtained neglecting terms that are higher than linear order in $\sigma, T, \vec{u}$, and their derivatives. Introducing the ground state *kinematic* shear and bulk viscosity ν and ζ these read

$$
\begin{aligned}
\frac{D\sigma}{Dt} &= -\Sigma\vec{\nabla}\cdot\vec{u} \\
\frac{Du}{Dt} &= 2\Omega v - \frac{1}{\Sigma}\left(\frac{\partial p}{\partial\sigma}\bigg|_o\frac{\partial\sigma}{\partial x} + \frac{\partial p}{\partial T}\bigg|_o\frac{\partial T}{\partial x}\right) \\
&\quad +\nu\nabla^2 u - \frac{3\Omega}{2\Sigma}\left(\frac{\partial\eta}{\partial\sigma}\bigg|_o\frac{\partial\sigma}{\partial y} + \frac{\partial\eta}{\partial T}\bigg|_o\frac{\partial T}{\partial y}\right) + \left(\frac{\nu}{3}+\zeta\right)\frac{\partial}{\partial x}(\vec{\nabla}\cdot\vec{u}) - \frac{\partial\phi}{\partial x} \\
\frac{Dv}{Dt} &= -\frac{1}{2}\Omega u - \frac{1}{\Sigma}\left(\frac{\partial p}{\partial\sigma}\bigg|_o\frac{\partial\sigma}{\partial y} + \frac{\partial p}{\partial T}\bigg|_o\frac{\partial T}{\partial y}\right) \\
&\quad +\nu\nabla^2 v - \frac{3\Omega}{2\Sigma}\left(\frac{\partial\eta}{\partial\sigma}\bigg|_o\frac{\partial\sigma}{\partial x} + \frac{\partial\eta}{\partial T}\bigg|_o\frac{\partial T}{\partial x}\right) + \left(\frac{\nu}{3}+\zeta\right)\frac{\partial}{\partial y}(\vec{\nabla}\cdot\vec{u}) - \frac{\partial\phi}{\partial y} \\
\frac{DT}{Dt} &= \frac{2}{3\Sigma}\left[-p\vec{\nabla}\cdot\vec{u} - 3\eta\Omega\left(\frac{\partial v}{\partial x}+\frac{\partial u}{\partial y}\right) + \frac{9}{4}\Omega^2\left(\frac{\partial\eta}{\partial\sigma}\bigg|_o\sigma + \frac{\partial\eta}{\partial T}\bigg|_o T\right)\right. \\
&\quad \left. - \left(\frac{\partial\Gamma}{\partial\sigma}\bigg|_o\sigma + \frac{\partial\Gamma}{\partial T}\bigg|_o T\right) + \kappa_D\nabla^2 T\right] \\
\nabla^2\phi(x,y,z) &= 4\pi G\,\sigma(x,y)\delta(z)\,.
\end{aligned}
\tag{3.2}
$$

Here, $D/Dt \equiv \partial_t - \frac{3}{2}\Omega x\partial_y$ is the material derivative and the symbol $|_o$ denotes that the respective differentiation has to be taken at the system's ground state. The perturbations in the self–gravity potential can be expressed through the perturbations in the density by use of the last equation and eq (2.39).

These equations are brought in a dimensionless form, scaling time with the inverse orbital frequency Ω^{-1}, density with the ground state quantity Σ, and velocities with the effective velocity dispersion c of the system. The effective velocity dispersion is defined via the total pressure

$$p = c^2\Sigma\,. \tag{3.3}$$

Length is scaled by c/Ω, which reduces in a dilute ring to the epicyclic length when c reduces to the velocity dispersion. In what follows, all variables and parameters are scaled quantities, their notation is unchanged. Further, the parameter $g \equiv \pi G\Sigma/(c\Omega)$ is introduced, which accounts for the system's self-gravity as compared to the pressure forces (c^2) and rotation (Ω). g is the inverse of the Toomre parameter (Toomre, 1964).

For shorthand writing partial derivatives taken at the ground state are denoted by a subscript, i.e.

$$p_\sigma \equiv \frac{\partial p}{\partial\sigma}\bigg|_o, \quad p_{\mathrm{T}} \equiv \frac{\partial p}{\partial T}\bigg|_o$$

are the derivatives of the total pressure (including a local and nonlocal part) and equivalent symbols are used for the ground state derivatives of (scaled) η and Γ. Further the symbol

$$E_{\mathrm{T}} \equiv \frac{2}{3}\frac{\partial\Gamma}{\partial T}\bigg|_o - \frac{3}{2}\frac{\partial\eta}{\partial T}\bigg|_o \tag{3.4}$$

is introduced, describing the linear reaction of the ground state radial energy balance (3.1) to variations in temperature.

For the non–axisymmetric perturbations of the stationary state with azimuthal wavenumber m and radial wavenumber n an appropriate ansatz that accounts for the shear in the system (i.e. $n = l + \frac{3}{2}m\,t$) reads

$$\begin{pmatrix} \sigma \\ u \\ v \\ T \end{pmatrix} = \begin{pmatrix} \sigma_t \\ u_t \\ v_t \\ T_t \end{pmatrix} \exp\left\{ i \left(l + \frac{3}{2} m\,t \right) x + i\,m\,y \right\} , \tag{3.5}$$

with time dependent amplitude functions σ_t, u_t, v_t, T_t. The solutions (3.5) with continuous wavenumbers describe an infinitely extended system. Periodic boundary conditions, as for instance employed by local simulations, require a discrete set of m and n, commensurable with a length of periodicity. Assuming solutions of the form of eq (3.5) (Goldreich & Tremaine, 1978b; Debrulle & Knobloch, 1992) the dependence of the linearized equations on the radial coordinate x is turned into a time dependence. Thus, for the amplitude functions a set of linear ordinary differential equations with time dependent coefficients is obtained

$$\begin{pmatrix} \dot\sigma_t \\ \dot u_t \\ \dot v_t \\ \dot T_t \end{pmatrix} = \widehat{M}(t) \begin{pmatrix} \sigma_t \\ u_t \\ v_t \\ T_t \end{pmatrix} \tag{3.6}$$

where $\widehat{M}$ is the coefficient matrix that depends on time through n

$$\widehat{M} = \tag{3.7}$$

$$\begin{pmatrix} 0 & -i\,n & -i\,m & 0 \\ i\left(2\frac{g\,n}{k} - \frac{3}{2}\eta_\sigma m - p_\sigma n\right) & -\left(\nu m^2 + n^2\left(\frac{4}{3}\nu + \zeta\right)\right) & 2 - n\,m\left(\frac{\nu}{3} + \zeta\right) & -i\left(\frac{3}{2}\eta_{\mathrm{T}} m + p_{\mathrm{T}} n\right) \\ i\left(2\frac{g\,m}{k} - \frac{3}{2}\eta_\sigma n - p_\sigma m\right) & -1/2 - n\,m\left(\frac{\nu}{3} + \zeta\right) & -\left(\nu n^2 + m^2\left(\frac{4}{3}\nu + \zeta\right)\right) & -i\left(\frac{3}{2}\eta_{\mathrm{T}} n + p_{\mathrm{T}} m\right) \\ \frac{3}{2}\eta_\sigma - \frac{2}{3}\Gamma_\sigma & -i\left(2m\,\nu + \frac{2}{3}p\,n\right) & -i\left(2n\,\nu + \frac{2}{3}p\,m\right) & -E_{\mathrm{T}} - \frac{2}{3}\kappa k^2 \end{pmatrix}$$

Here $k \equiv \sqrt{m^2 + n^2}$ is the modulus of the wavenumber.

3.1.2 Asymptotic Linear Stability of Non-Axisymmetric Perturbations

In this section expressions for the asymptotic (large time) behavior of the solutions of eq (3.6) are derived, following the treatment of Debrulle & Knobloch (1992) of a similar system of equations for compressible plane Couette flow. It is assumed that for large times the solutions can be expressed in the form

$$\begin{pmatrix} \sigma_t \\ u_t \\ v_t \\ T_t \end{pmatrix} = \begin{pmatrix} \hat\sigma \\ \hat u \\ \hat v \\ \hat T \end{pmatrix} \exp\{\theta(t)\} . \tag{3.8}$$

Then $\dot\theta$ is given by the eigenvalues of the coefficient matrix (3.7). The eigenvalues can be expanded asymptotically as

$$\dot\theta = a_2 t^2 + a_1 t + a_0 + a_{-1}/t \ldots . \tag{3.9}$$

Additionally the $1/k$ term in eq. (3.7) is expanded asymptotically in powers of $1/t$. Equating each power of t in the characteristic equation separately to zero gives four distinct solutions for each coefficient a_i. The corresponding four solutions for the function $\theta(t)$ are in leading order in t

$$\begin{aligned}
\theta_1 &= -\frac{p_\sigma t}{\left(\frac{4}{3}\nu + \zeta\right)} + O(1) \\
\theta_2 &= -\frac{1}{2}\kappa\, m^2\, t^3 + O(t^2) \\
\theta_3 &= -\frac{3}{4}\,\nu\, m^2\, t^3 + O(t^2) \\
\theta_4 &= -\frac{3}{4}\left(\frac{4}{3}\nu + \zeta\right)\, m^2 t^3 + O(t^2)\,.
\end{aligned} \tag{3.10}$$

Thus, all non–axisymmetric modes are *linearly* stable[1], decaying asymptotically as $\exp\theta_i$. Every small non–axisymmetric perturbation is 'wound up' by the differential rotation of the system, its radial wavelength tending eventually to zero. This does not mean, however, that non–axisymmetric structures are impossible at all in this system. The equations (3.6) allow for transient growth of small initial perturbations that can grow in the nonlinear regime, thus violating the validity of the linear approximation, and may locally change the ground state considerably (Debrulle & Knobloch, 1992). In the context of the excitations of density waves in galaxies this amplification mechanism has been discussed for a similar (but inviscid) system for instance by Julian & Toomre (1966) and Goldreich & Tremaine (1978b) [see also Toomre (1981) and Goldreich & Lynden-Bell (1964)]. In a planetary ring the gravitational interaction of such structures may give rise to gravitational wakes (Salo, 1992a). In Salo et al. (2000b) it is shown that in simulations gravitational wakes in general coexist with the radial oscillating density patterns formed by overstable modes of axisymmetric perturbations (see also chapter 4). This thesis focuses solely on the radial structure caused by overstability.

3.1.3 Growth Rates of Radial Modes

Focusing on purely radial modes $\propto \exp\{\omega\, t + i\, k\, x\}$ the characteristic equation of $\widehat{M}$ for $m = 0$ yields a real local dispersion relation connecting the complex growth rate ω and the modulus of the radial wavenumber k

$$0 = f_0(k) + f_1(k)\omega + f_2(k)\omega^2 + f_3(k)\omega^3 + \omega^4\,. \tag{3.11}$$

The functions f_i are given in Spahn et al. (2000) in terms of un–scaled quantities in the notation of eq (3.2).

For the kinematic shear viscosity a dependence on the surface density of the form

$$\nu \propto \sigma^\beta\,, \tag{3.12}$$

is assumed (Schmit & Tscharnuter, 1995). This assumption is justified, because the exponent β is depending weakly on the ground state density Σ and the collision frequency of the system, and thus, can be considered constant for small amplitudes of the density perturbation σ. However, β can be varied with the ground state density Σ, thus serving as an order parameter in the analyses. The derivative of the dynamic viscosity with respect to density is then given by

$$\eta_\sigma = \nu(\beta + 1)\,. \tag{3.13}$$

[1]Provided, that $p_\sigma > 0$, as it the case here although in an ensemble of dissipatively colliding particles $p_\sigma < 0$ is possible if the temperature is a strongly *decreasing* function of the density.

Using the scaled quantities the dispersion relation (3.11) is expressed in the form

$$\begin{aligned}0 = \;& p_{\rm T} k^2 \left(-k^2\left(\tfrac{2}{3}\Gamma_\sigma \nu + \tfrac{3}{2}(1+\beta)\nu^2\right) + \left(-\tfrac{2}{3}\Gamma_\sigma + \tfrac{1+3\beta}{2}\nu + \tfrac{2}{3}k^2\nu p\right)\omega + \tfrac{2}{3}p\omega^2\right)\\ +\;& 3\eta_{\rm T} k^2 \left(-\tfrac{2}{3}\Gamma_\sigma + \tfrac{3}{2}(1+\beta)\nu + p_\sigma k^2 \nu - 2k\nu g + \nu\omega^2 + \omega\left(\tfrac{2}{3}p + k^2\nu\left(\tfrac{4}{3}\nu + \zeta\right)\right)\right)\\ +\;& D_{iso}\left(E_{\rm T} + \tfrac{2}{3}k^2\kappa + \omega\right)\end{aligned} \tag{3.14}$$

where

$$\begin{aligned}D_{iso} &= \omega^3 + \omega^2 k^2 \nu\left(\frac{7}{3} + \zeta\right) + \omega\left(1 - 2kg + p_\sigma k^2 + k^4\nu\left(\frac{4}{3}\nu + \zeta\right)\right)\\ &\quad + \nu k^2\left(3(1+\beta) - 2kg + k^2 p_\sigma\right).\end{aligned} \tag{3.15}$$

$D_{iso} \equiv 0$ is the dispersion relation calculated by Schmit & Tscharnuter (1995) which is contained as the isothermal limit in our model [see also Spahn et al. (2000)]. Namely, for finite $\eta_{\rm T}, p_{\rm T}, \Gamma_{\rm T}$, and arbitrary but fixed ω and k, the relation $D_{iso} = 0$ follows from the fourth order non–isothermal dispersion relation (3.14) in the limit of infinite heat conductivity κ. This limit is physically clear, since a large heat conductivity rapidly smoothes out fluctuations in the temperature, leading eventually in the mathematical limit $\kappa \to \infty$ to the isothermal system from which the dispersion relation $D_{iso} \equiv 0$ is derived. Similarly, the isothermal dispersion relation is obtained for $E_{\rm T} \to \infty$, where $E_{\rm T}$ gives the inverse of the relaxation time for a thermally excited system (see below).

In order to obtain approximate expressions for the roots of eq. (3.14) in the long wavelength limit the growth rates $\omega(k)$ are expanded in powers of k as

$$\omega(k) = b_0 + b_1 k + b_2 k^2 \ldots . \tag{3.16}$$

Inserting this relation in eq. (3.14) and equating each power of k separately to zero yields four solutions for the b_i and thus four approximate solutions $\omega^{(i)}(k)$ which read to order k^2

$$\omega^{(1)}(k) = -E_{\rm T} - k^2\frac{2}{3}\kappa + k^2 F_1 + O(k^3) \tag{3.17}$$

$$\begin{aligned}\omega^{(2)}(k) &= i\left[1 - g\,k - \frac{k^2}{2}\left(g^2 - p_\sigma\right) + k^2 F_2\right]\\ &\quad + \frac{k^2}{2}\left[\nu\left(\frac{2}{3} + 3\beta\right) - \zeta\right] + k^2 F_3 + O(k^3)\end{aligned} \tag{3.18}$$

$$\omega^{(3)}(k) = {\omega^{(2)}}^*(k) \tag{3.19}$$

$$\omega^{(4)}(k) = 3\,\frac{k^2}{E_{\rm T}}\left[\frac{2}{3}\Gamma_\sigma\eta_{\rm T} - \nu(1+\beta)\left(\frac{3}{2}\eta_{\rm T} + E_{\rm T}\right)\right] + O(k^3), \tag{3.20}$$

where

$$\begin{aligned}F_1 &= \frac{p_{\rm T}}{1+E_{\rm T}^2}\left(\frac{2}{3}\Gamma_\sigma - \nu\frac{1+3\beta}{2} + \frac{2}{3}E_{\rm T}\,p\right)\\ &\quad - \frac{3\eta_{\rm T}}{E_{\rm T}(1+E_{\rm T}^2)}\left(\frac{2}{3}\Gamma_\sigma + \frac{2}{3}E_{\rm T}\,p - \nu\left\{\frac{1+3\beta}{2} + 1 + E_{\rm T}^2\right\}\right)\\ F_2 &= -\frac{p_{\rm T}}{1+E_{\rm T}^2}\left\{\frac{2}{3}\Gamma_\sigma E_{\rm T} - \frac{2}{3}p - \nu\frac{1+3\beta}{2}E_{\rm T}\right\}\\ &\quad + \frac{3\eta_{\rm T}}{1+E_{\rm T}^2}\left\{\frac{2}{3}\Gamma_\sigma + \frac{2}{3}E_{\rm T}\,p - \nu\frac{1+3\beta}{2}\right\}\\ F_3 &= -\frac{p_{\rm T}}{1+E_{\rm T}^2}\left(\frac{2}{3}\Gamma_\sigma + \frac{2}{3}E_{\rm T}\,p - \nu\frac{1+3\beta}{2}\right)\\ &\quad - \frac{3\eta_{\rm T}}{1+E_{\rm T}^2}\left(\frac{2}{3}\Gamma_\sigma E_{\rm T} - \frac{2}{3}\,p - \nu\frac{1+3\beta}{2}E_{\rm T}\right)\end{aligned}$$

The mode with purely real growth rate $\omega^{(1)}$ is connected to the thermal stability of the system. The leading wavelength independent term E_{T} describes the dependence of the radial energy balance between viscous heating and collisional cooling on variation of the temperature [see eq (3.4)]. For stability E_{T} has to be positive, requiring the cooling to dominate the heating when temperature is increased over the ground state value, and vice versa when the temperature is decreased. The second term, proportional to k^2, corresponds to a hydrodynamic heat diffusion mode, with the term $\propto \kappa$ which is purely damping. For the parameter values of the dispersion relation determined in simulations (chapter 4) E_{T} is indeed positive in all cases and dominates the other two terms in the expansion $\omega^{(1)}$. Also, the correction F_1 is always smaller then the term $\frac{2}{3}\kappa$.

The second and third modes have complex conjugate growth rates $\omega^{(2)}$ and $\omega^{(3)}$. Their real parts may become positive for appropriate β, leading to oscillatory instability. The functions F_2 and F_3 contain the corrections to the isothermal model due to the heat flow equation at this order, the other terms already follow from the isothermal model. In the isothermal model the imaginary part is the Keplerian frequency with corrections due to self-gravity and pressure forces. The real parts yield an expression for the stability boundary in the limit $\lambda \to \infty$

$$\beta_{cr}^{\infty} \equiv \frac{1}{3}\left(\frac{\zeta}{\nu} - \frac{2}{3}\right) \tag{3.21}$$

so that long wavelengths become overstable if $\beta > \beta_{cr}^{\infty}$ which was already derived by Schmit & Tscharnuter (1995). An exact expression for the line of marginal stability $\beta_{cr}(k)$ for the isothermal model is given in section (3.3) where eigenfunctions of the hydrodynamic equations are derived at marginal stability.

The fourth mode with growth rate $\omega^{(4)}$, corresponding to the viscous instability, is again purely real. It reduces in the isothermal limit to

$$\omega^{(4)} \to -3k^2\,\nu(1+\beta) + O(k^3) \tag{3.22}$$

yielding the stability criterion $\beta > -1$ which is equivalent to the conditions derived by Lin & Bodenheimer (1981), and Ward (1981).

Since with the heat flow an additional diffusion mechanism is introduced in the system the functions F_2 and F_3, can be expected to have a primarily stabilizing effect, as argued in Spahn et al. (2000). This is confirmed by the quantitative comparison presented in chapter 5.

3.2 Estimation of Parameters

The 4th order dispersion relation (3.14) resulting from the linear stability analyses of the z–integrated non–isothermal hydrodynamic equations (2.20) includes a number of parameters that have to be evaluated before any conclusion about the stability of the stationary Keplerian flow field can be drawn. These parameters are the ground state values for the kinematic shear viscosity ν, bulk viscosity ζ, and heat conductivity κ, the equation of state $p = p(\Sigma, T_0)$, the cooling function $\Gamma = \Gamma(\Sigma, T_0)$, and the derivatives of p, ν, and Γ with respect to the temperature and the surface density taken at the ground state. Further parameters are the ground state values Σ and T_0 themselves and the Kepler frequency Ω at the location in the rings of interest. The latter are unproblematic since the radial optical depth profile of the rings is well known and for the velocity dispersion and particle's material density estimations exist in the literature. Also for the magnitude of the shear viscosity some independent estimations exist, emerging from the observation of the damping of resonance induced density and bending waves in Saturn's rings (Shu, 1984; Shu et al., 1985a; Shu et al., 1985b).

To investigate the qualitative effect of the heat flow equation on the stability of the system the remaining parameters can be estimated using a simplified but physically reasonable set of assumptions (Spahn et al., 2000). So, for the dependence of the viscosity on perturbation temperature and density the parameterization

$$\nu \propto \sigma^{\beta} T^{\alpha} \tag{3.23}$$

is used, where the parameter $\beta = \partial \log \nu / \partial \log \sigma$ is the same as in the isothermal model. For dense rings ($\tau \geq 1$) β is found analytically (Araki & Tremaine, 1986) and by molecular dynamics simulations (Wisdom & Tremaine, 1988; Salo, 1991) to be larger than one. According to analytical studies (Stewart et al., 1984; Goldreich & Tremaine, 1978a) $\alpha = 1$ should be used [see eq (2.14)]. However, simulations of dense rings suggest an effective $\alpha \leq 1/2$ [see Salo (1991) and under the additional influence of a size distribution Salo (1992b)]. The exponent α smaller than 1 can be attributed to the nonlocal part of the shear viscosity that depends more weakly on the temperature than the local part. For the granular cooling the relation

$$\Gamma = \Omega \tau \sigma (1 - \epsilon^2) T \tag{3.24}$$

gives an estimate (Stewart et al., 1984). One notices the difference in the temperature dependence of the cooling as compared to the granular expression (B.6) where the temperature has an exponent 3/2. This is a consequence of the z–integration: an implicit temperature dependence is hidden in the collision frequency $\omega_c \approx \Omega\tau$. Inserting instead for the collision frequency the estimation (2.12), i.e. $\omega_c \propto \rho c$, then $\Gamma \propto T^{3/2}$ is retained.

No estimations exist so far in the literature for the bulk viscosity and the heat conductivity in the rings. In fig (3.1) the ratios of bulk viscosity to shear viscosity and heat conductivity to shear viscosity are shown for elastic hard sphere gases taken from the textbook by Chapman & Cowling (1970) and for slightly inelastic hard sphere gases from the relations (B.1, B.2, B.3) given in appendix B as derived by Jenkins & Richman (1985). For high filling factors these ratios approach constant values, i.e. $\kappa/\nu \approx 4$ and $\zeta/\nu \approx 1$, which should at least give an order of magnitude estimation for the dense Saturnian B ring.

The equation of state $p = p(\Sigma, T_0)$ should in principle contain a nonlocal pressure accounting for the enhanced collision frequency and the reduced free volume due to the particles' proper volume. However, the pressure affects mainly the short wavelength perturbations of the system (Spahn et al., 1997), and for a qualitative estimate of the longer wavelengths that become overstable [$\lambda \geq 100\,m$ (Schmit & Tscharnuter, 1995)] the relation for an ideal gas will be sufficient, i.e.

$$p = \sigma T\,. \tag{3.25}$$

With these expressions the dispersion relation can be solved numerically for its roots. In fig (3.2) lines of equal ten–folding times of the overstable modes of the dispersion relation are shown in the (λ, β)–plane. These are plotted in units of one orbital revolution so that the annotations are related to the real parts of the growth rates of overstability by

$$T_{10}[\text{orbits}] \equiv \frac{\ln 10}{2\pi} \frac{\Omega}{\mathrm{Re}(\omega)}\,. \tag{3.26}$$

For the stability diagrams of fig (3.2) the values $\nu = 54 \cdot 10^{-4}\,\mathrm{m^2/s}$ and $c = 2 \cdot 10^{-3}\,\mathrm{m/s}$ are used as in Schmit & Tscharnuter (1995) for the kinematic viscosity and the velocity

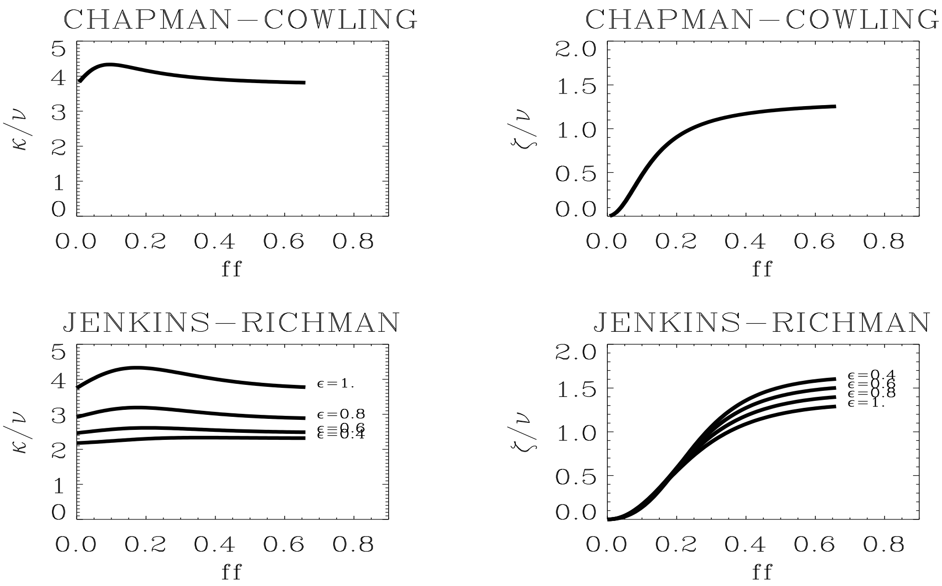

Figure 3.1: *The ratios κ/ν and ζ/ν for dense elastic hard sphere gases (Chapman & Cowling, 1970) and for slightly inelastic hard sphere gases (Jenkins & Richman, 1985). For high filling factors these ratios approach constant values.*

dispersion, which are motivated by observations and numerical experiments. For the optical depth $\tau = 1$ is chosen and a particle bulk density slightly smaller than the one of ice, i.e. $\rho_p = 900\,\mathrm{kg/m^3}$, giving a surface density $\sigma = \tau\, m_p/(R_p\, \pi^2) = 1,200\,\mathrm{kg/m^2}$ for meter sized particles. For the constant coefficient of restitution a value of $\epsilon = 0.4$ is used which is consistent with an effective velocity dependent coefficient of restitution following from the empirical formula of Bridges et al. (1984) [see eq (4.5)] when for the typical impact velocity the velocity dispersion is inserted with equally distributed impact angles. In accordance with the high–filling–factor values of the above mentioned transport coefficients for hard sphere gases [fig (3.1)]the ratio of bulk viscosity to shear viscosity has been fixed to $\zeta/\nu = 1$. Rise times are shown for $\kappa/\nu = 4$, representing the non-isothermal system, and for $\kappa/\nu = \infty$ displaying the isothermal limit [see eq (3.14) and the subsequent discussion].

Clearly, the energy balance equation has a stabilizing effect, shifting the line of marginal stability to higher values of β. This shift is, however, rather insensitive to small variations in κ/ν. $\beta = 1.26$, the value used in Schmit & Tscharnuter (1995), is consistent for an optical depth $\tau = 1$ with the analytical results of Araki & Tremaine (1986) and molecular dynamics simulations (Wisdom & Tremaine, 1988; Salo, 1991). The value of $\alpha = 0.5$ further stabilizes the system as compared to $\alpha = 1$ and shifts the critical wavelength of about 100 m to slightly larger values. Self–gravity has a destabilizing effect on the smaller wavelengths, shifting here the line of marginal stability to smaller β and smaller λ. In the self–gravitating case the marginal curves develop a minimum (see also section 3.3.3).

Another factor that tends to stabilize the overstable mode is the bulk viscosity. If ζ/ν exceeds unity [which was assumed in fig (3.2)], the viscous overstability is shifted to higher β. For example, $\zeta/\nu = 2$ would shift the marginal curve to about $\beta = 1$ for the self–gravitating case and for $\kappa/\nu = 4$, $\alpha = 0.5$ in fig (3.2). The variation of the bulk viscosity affects similarly the isothermal model as already indicated by the analysis of Schmit & Tscharnuter (1995),

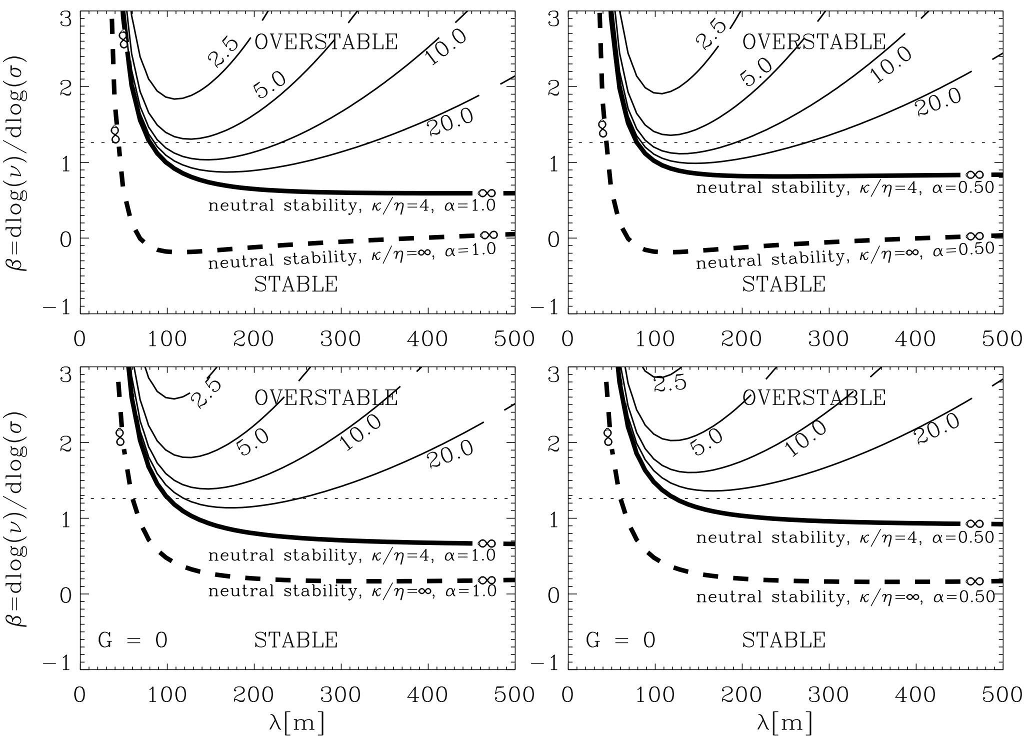

Figure 3.2: *Rise times of overstable perturbations in the* (λ, β)*–plane for an optical depth* $\tau = 1$*, coefficient of restitution* $\epsilon = 0.4$*, for particles of* $1\,m$ *radius and an material density* $\rho_p = 900\,kg/m^3$*. Shown are lines of equal ten–folding times of a given perturbation in units of an orbital revolution [eq (3.26)]. The region above marginal stability, drawn as a thick line, is overstable, the region below is stable. The line of marginal stability of the isothermal limit* ($\kappa \to \infty$) *is also drawn for comparison as a dashed line. The dotted horizontal line marks the value* $\beta = 1.26$ *(Araki & Tremaine, 1986). The plots on the left are for* $\alpha \equiv \partial(\log \nu)/\partial(\log T) = 1$*, those on the right for* $\alpha = 0.5$*. The upper two plots show the rise times for self–gravitating systems, the lower ones for systems without self–gravity.*

although they assumed $\zeta/\nu = 1$ throughout their paper.

In fig (3.3) lines of equal rise times corresponding to the instability of the viscous diffusion mode of the dispersion relation are shown for the same set of parameters as in fig (3.2). For this mode, the energy balance equation seems to have a destabilizing influence, shifting the line of marginal stability for $\alpha = 1$ even to positive β close to one. However, as already argued above, earlier molecular dynamics simulations (Salo, 1991; Salo, 1992b) imply a smaller value of α, and a detailed determination of transport coefficients for planetary rings in simulations (Salo et al., 2000a), to be presented in chapter 4.3, even yields an α close to zero. Already $\alpha = 0.5$ stabilizes the viscous diffusion mode considerably compared to $\alpha = 1$, making a viscous instability improbable for the dense model ring considered here. As for the oscillatory mode self–gravity has a destabilizing influence on the smaller wavelengths, the curves of marginal stability develop a maximum.

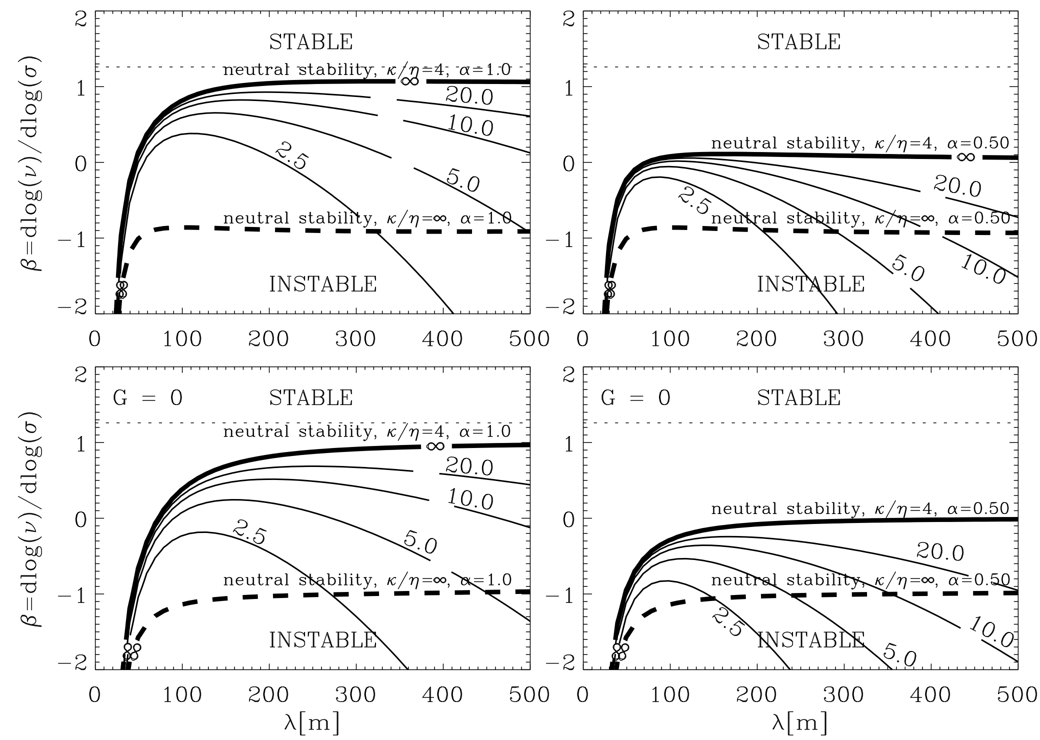

Figure 3.3: *Rise times of perturbations subject to viscous instability in the (λ, β)–plane.*

3.3 Weakly Nonlinear Stability of the Isothermal Model

In this section the *isothermal* hydrodynamic model for the overstability is considered, as it was investigated by Schmit & Tscharnuter (1995). The nonlinear saturation of the overstable modes is modeled in terms of a weakly nonlinear stability analysis of the basic hydrodynamic equations: a Landau equation is derived for the growth of the amplitude of the overstable modes that emerge slightly above threshold for the onset of overstability, employing the method of multiple scales (Cross & Hohenberg, 1993).

The computations are restricted for simplicity to the isothermal model since here the derivation of Landau equation can be carried out analytically. Because of the neglect of the thermal mode the results cannot be expected to describe quantitatively the behavior observed in simulations. The focus lies merely on qualitative effects of the nonlinearity, as the saturation of the growth of overstable modes and the nonlinear competition of left and right moving traveling wave solutions at marginal stability. Also, nonlinear corrections to the linear eigenfunctions at marginal stability, obtained in course of the derivation of the Landau equation, can be compared qualitatively to the modes observed in simulations.

The nonlinear balances for mass and momentum of the isothermal model for purely radial perturbations of the state variables are displayed in section 3.3.1. The method of multiple scales is shortly outlined in section 3.3.2 and applied to the model in the subsequent sections.

3.3.1 Nonlinear Equations

Using the same scaling as in chapter 3.1.1 the dimensionless nonlinear isothermal continuity equation and the Navier Stokes equations read

$$\dot{\sigma} = -(\sigma\, u)' \tag{3.27}$$

$$\begin{aligned}\dot{u} &= 2v - p_{\sigma}\frac{\sigma'}{\sigma} - u\,u' + \left(\frac{4}{3}+\frac{\zeta}{\nu}\right)\nu\sigma^{\beta}\,u'' \\ &\quad + \left(\frac{4}{3}+\frac{\zeta}{\nu}\right)\nu(1+\beta)\sigma^{\beta-1}\sigma' u' + \phi'(\sigma)\end{aligned} \tag{3.28}$$

$$\dot{v} = -\frac{u}{2} - u\,v' + \nu\sigma^{\beta}v'' + \nu(1+\beta)\sigma^{\beta-1}\sigma'(v' - \frac{3}{2})\,. \tag{3.29}$$

The surface density is denoted by σ, and u and v are the radial and *shear corrected* tangential velocities. In this chapter σ, u, and v refer to the scaled *total* values for the state variables and not to the deviations from the stationary state as in the previous chapters.

For the dynamic shear viscosity the expression

$$\eta = \nu\sigma^{1+\beta} \tag{3.30}$$

is used where ν is the *ground state* value for the kinematic viscosity. ζ is the ground state value of the bulk viscosity. ϕ is the ring's self–gravity potential which is related to the surface density by eq (2.39). The influence of the disk's self–gravity compared to the stabilizing effects of pressure (c^2) and rotation (Ω) is described by the dimensionless parameter $g = (\pi G\Sigma)/(c\Omega)$ which is defined as the inverse of the Toomre parameter. A prime denotes the derivative with respect to radial coordinate and a dot the derivative with respect to time.

3.3.2 Outline of the Method

The method of multiple scales has been successfully applied in the literature to many pattern forming systems to separate near criticality the slow evolution of a few dominant (unstable) modes from the continuum of stable modes that follow them adiabatically on a fast time scale (Cross & Hohenberg, 1993).

Order Parameter Expansion

The basic idea is to expand the state variables in powers of the order parameter δ, labeling the distance of the system to the threshold for the onset of an instability. This order parameter will for the system of equations (3.27) be identified with the square root of $(\beta-\beta_{cr})/\beta_{cr}$, where β_{cr} is the critical value of the exponent β of the density dependence of the viscosity (3.30) where oscillatory instability sets in. The time development is assumed to separate on a 'fast' scale (e.g. overstable oscillations, one orbital revolution) and a 'slow' scale (growth of the overstable modes), the scaling determined in terms of δ by the ultimate consistency of the expansion and in particular by the scaling of the unstable roots of the dispersion relation of the linear order [see eq (3.57) below]. The expansion reads

$$\sigma = 1 + \delta\sigma_1 + \delta^2\sigma_2 + \ldots \tag{3.31}$$

$$u = \delta u_1 + \delta^2 u_2 + \ldots \tag{3.32}$$

$$v = \delta v_1 + \delta^2 v_2 + \ldots \tag{3.33}$$

$$\beta = \beta_{cr} + \delta\beta_1 + \delta^2\beta_2 + \ldots \tag{3.34}$$

$$\partial_t \rightarrow \partial_t + \delta^2\partial_\theta\,. \tag{3.35}$$

The last relation introduces in addition to ordinary 'fast' time t the 'slow' time-scale θ. The scales are well separated for small values of δ, i.e. near the threshold of overstability.

Let the vector of state variables ψ be defined as

$$\psi(x,t) = \sum_{i=0}^{\infty} \delta^i \psi_i(x,t), \quad \psi_i(x,t) = \begin{pmatrix} \sigma_i(x,t) \\ u_i(x,t) \\ v_i(x,t) \end{pmatrix}. \tag{3.36}$$

Then the expanded equations (3.27) can be written in the form

$$\begin{aligned} O(\delta^1): &\quad L\psi_1 = 0 \\ O(\delta^2): &\quad L\psi_2 = N_2(\psi_1, \psi_1) \\ O(\delta^3): &\quad L\psi_3 = N_3(\psi_1, \psi_2) + \partial_\theta \psi_1 \\ &\quad \vdots \end{aligned} \tag{3.37}$$

so that in successive orders in δ the same linear operator L appears on the left hand side. L itself is of order δ^0. The functions N_i are the remaining nonlinear terms at order i. The nonlinear problem has split in an iterative sequence of linear inhomogeneous equations where the inhomogeneities at a given order are nonlinear functions of the solutions of the lower order equations. The linear operator L is given by

$$L = \begin{pmatrix} \partial_t & \partial_x & 0 \\ (p_\sigma + \frac{\partial \phi}{\partial \sigma})\partial_x & \partial_t - \left(\frac{4}{3} + \frac{\zeta}{\nu}\right)\nu\partial_x^2 & -2 \\ \frac{3}{2}\nu(1+\beta_{cr})\partial_x & \frac{1}{2} & \partial_t - \nu\partial_x^2 \end{pmatrix}. \tag{3.38}$$

The gravitational potential ϕ of the disk will be related to the surface density by eq (2.39). Note that the linear operators used implicitly in section 3.1.1, i.e. eq (3.2,3.7) were *not* restricted to marginal stability of viscous overstability. In contrast, L has to be of zeroth order in δ, and thus, β_{cr} appears instead of β, a consequence of the expansion about the distance δ to marginal stability considered in the current section.

Adjoint Linear Operator and Solvability Conditions

The existence of solutions of an inhomogeneous linear problem as eq (3.37) is restricted by Fredholm's theorem, leading to the so called solvability conditions.

Suppose a scalar product is given in the space of the state variables ψ. Then the Fredholm theorem states that solutions of the inhomogeneous linear problem exist if and only if the inhomogeneity is orthogonal to the solutions of the homogeneous adjoint problem. Let $L^\dagger$ be the adjoint operator of L and ψ_0^{ad} one of its null solutions, i.e. $L^\dagger \psi_0^{ad} = 0$. Multiplying the expanded equations (3.37) scalar with ψ_0^{ad} leads then to the conditions

$$O(\delta^2): \quad \langle \psi_0^{ad} | N_2(\psi_1, \psi_1) \rangle = 0 \tag{3.39}$$

$$O(\delta^3): \quad \langle \psi_0^{ad} | N_3(\psi_1, \psi_2) + \partial_\theta \psi_1 \rangle = 0 \tag{3.40}$$

$$\vdots$$

the solvability conditions at the respective order in the expansion (3.37). In particular the solvability condition at order δ^3 yields an equation for the time development on the slow time scale θ of the solution ψ_1 of the linear order in the expansion (3.37).

Let a scalar product in the space of marginal overstable eigensolutions ψ [solutions of the form (3.60)] be defined as

$$\langle\psi^i|\psi^j\rangle \equiv \lim_{t_f\to\infty}\lim_{D\to\infty}\frac{1}{t_f}\frac{1}{D}\int_0^{t_f}\mathrm{d}t\int_{-D/2}^{D/2}\mathrm{d}x\,(\sigma^{i^*}\sigma^j + u^{i^*}u^j + v^{i^*}v^j)\,. \tag{3.41}$$

With respect to that scalar product the adjoint operator $L^\dagger$ is given by

$$L^\dagger = \begin{pmatrix} -\partial_t & -(p_\sigma + \frac{\partial\phi}{\partial\sigma})\partial_x & -\frac{3}{2}\nu(1+\beta_{cr})\partial_x \\ -\partial_x & -\partial_t - \left(\frac{4}{3}+\frac{\zeta}{\nu}\right)\nu\partial_x^2 & 1/2 \\ 0 & -2 & -\partial_t - \nu\partial_x^2 \end{pmatrix} \tag{3.42}$$

The two linearly independent single mode null solutions ($\propto \exp\{\omega\,t + i\,k\,x\}$) of $L^\dagger\psi = 0$ in the overstable subspace at marginal stability [$\mathrm{Re}(\omega) = 0$, $\mathrm{Im}(\omega) =: s, s \neq 0$] are

$$\psi_{0,1}^{ad} = \varphi_{0,1}^{ad}\exp\{-i\,s\,t + i\,k\,x\} \quad \text{and} \quad \psi_{0,2}^{ad} = \varphi_{0,2}^{ad}\exp\{i\,s\,t + i\,k\,x\} \tag{3.43}$$

with[2]

$$s = \sqrt{1 - 2gk + p_\sigma k^2 + \left(\frac{4}{3}+\frac{\zeta}{\nu}\right)\nu^2 k^4} \tag{3.44}$$

which is the frequency of the overstable oscillations at marginal stability in the isothermal model, and

$$\varphi_{0,1}^{ad} = \begin{pmatrix} i(p_\sigma k - 2g) + sk\nu\left(\frac{7}{3}+\frac{\zeta}{\nu}\right) \\ i\,s + \nu k^2 \\ 2 \end{pmatrix} \tag{3.45}$$

$$\varphi_{0,2}^{ad} = \begin{pmatrix} i(p_\sigma k - 2g) - sk\nu\left(\frac{7}{3}+\frac{\zeta}{\nu}\right) \\ -i\,s + \nu k^2 \\ 2 \end{pmatrix}. \tag{3.46}$$

$$\tag{3.47}$$

The computation of these null solutions of $L^\dagger$ is entirely in parallel to the solution of the $O(\delta^1)$ equation of eq (3.37) presented in greater detail in the following section.

Practically, the desired Landau equation describing the time evolution of ψ_1 on the slow time scale θ can now be derived in the following steps:

- Assume that the dependences of ψ_1 on t and θ factorize, i.e, $\psi_1 = A(\theta)f(x,t) + c.c$ with complex amplitude A.
- Compute ψ_1 from the $O(\delta^1)$ equation in (3.37).
- Determine with ψ_1 the inhomogenity and the corresponding solvability conditions at $O(\delta^2)$ with the adjoint null solutions (3.43).
- Compute a solution for ψ_2 from the $O(\delta^2)$ equation in (3.37).

[2] The expression under the root is always positive in the regime of parameter values (g, p_σ, ν) that are of interest here.

- Determine with ψ_1 and ψ_2 the inhomogenity and the corresponding solvability condition at $O(\delta^3)$

The solvability condition at $O(\delta^3)$ yields a first order ordinary differential equation for the time development of the complex amplitude $A(\theta)$. In general it may contain linear, quadratic, and cubic terms in A. Since the underlying system requires invariance under the inversion $A \longrightarrow -A$ the quadratic term vanishes and a Landau equation is obtained

$$\partial_\theta A = c_1 A + c_2 |A|^2 A \tag{3.48}$$

with complex coefficients c_1 and c_2.

More generally, if the solution ψ_1 of the linear problem is a superposition of left and right traveling wave solutions with amplitudes A_L and A_R, then two coupled Landau equations are obtained

$$\begin{aligned} \partial_\theta A_L &= c_3 A_L + c_4 |A_L|^2 A_L + c_5 |A_R|^2 A_L \\ \partial_\theta A_R &= c_3 A_R + c_4 |A_R|^2 A_R + c_5 |A_L|^2 A_R \,. \end{aligned} \tag{3.49}$$

The coefficient c_3 is an approximation to the real parts of the growth rates of overstable modes, accurate to third order in δ. c_4 and c_5 will give nonlinear saturation and the competition of traveling and standing wave solutions, depending on their signs and magnitudes. So the *form* of eq (3.49) follows already from the symmetry of the system and by inspection of eq (3.37). The computation and subsequent discussion of the coefficients c_i for the equations (3.27) is left to the remainder of this chapter.

3.3.3 The Linear Problem

In this section the solution ψ_1 of the equation (3.37) at $O(\delta^1)$ is determined. Further, the curve of marginal stability for the viscous overstability in the $(\beta,\, k)$ plane is given. The scaling with δ of the unstable eigenvalues of the linear problem—expanded about this marginal curve—determines the scaling of slow and fast time.

For an isothermal system with purely radial excitations $\propto \exp\{\omega t + i\, k\, x\}$ the matrix (3.7) reduces to the spatial part of the linear operator (3.38) in Fourier space

$$\widehat{M} = \begin{pmatrix} 0 & -i\,k & 0 \\ i(2g - p_\sigma k) & -k^2\nu\left(\frac{4}{3} + \frac{\zeta}{\nu}\right) & 2 \\ -i\frac{3}{2}\nu(1+\beta)k & -1/2 & -k^2\nu \end{pmatrix} \tag{3.50}$$

which leads to the third order dispersion relation[3] given by setting eq (3.15) to zero, i.e.

$$\begin{aligned} 0 \;=\;& \omega^3 + \omega^2 k^2 \nu \left(\frac{7}{3} + \frac{\zeta}{\nu}\right) + \omega\left(1 - 2kg + p_\sigma k^2 + k^4\nu^2\left(\frac{4}{3} + \frac{\zeta}{\nu}\right)\right) \\ & + \nu k^2 \left(3(1+\beta) - 2kg + k^2 p_\sigma\right) \,. \end{aligned} \tag{3.51}$$

This relation has got one real and two conjugate complex roots ω. From the analysis of Schmit & Tscharnuter (1995) (also from chapters 3.1.3 and 3.2) it is clear that depending on the value of β these roots may have a positive real part. Assuming a purely imaginary

[3] In the thin disk solution of the Poisson equation (2.39) only the modulus of the wavenumber enters. Thus, actually $g\cdot\mathrm{sgn}(k)$ had to be written in eq (3.50) and the following equations instead of g. For notational convenience simply keep in mind that in the following $g \longrightarrow -g$ when $k \longrightarrow -k$.

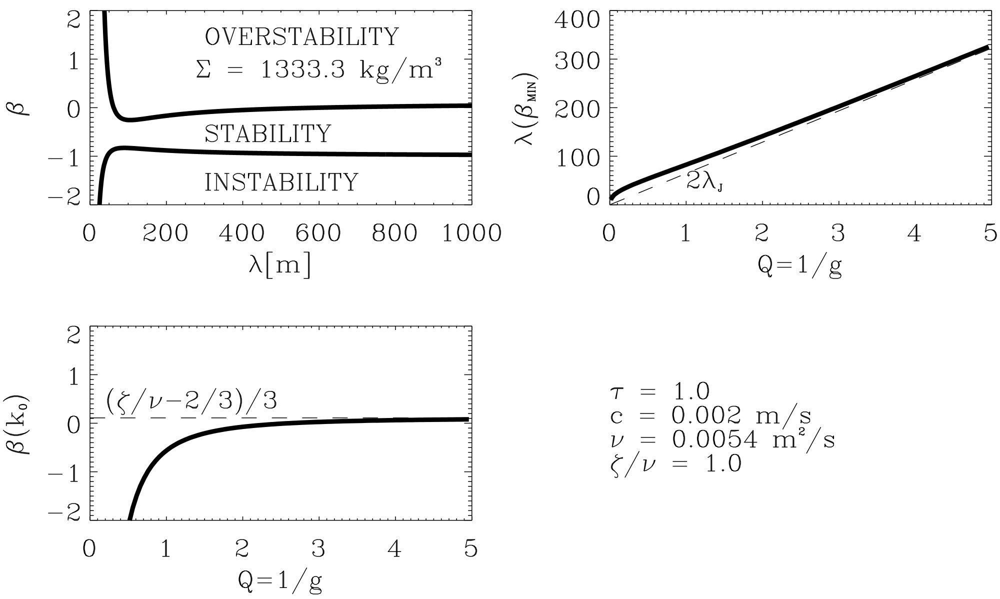

Figure 3.4: *Upper left: Marginal curves of viscous instability and overstability in the* (λ, β)*–plane for plausible parameter values for a dense Saturnian ring. The value of the surface density* Σ *is fixed to* $1,333\,kg/m^2$*. Upper right: The critical wavelength in meters given by eq (3.54) plotted against the Toomre parameter* $Q \equiv \frac{1}{g} = \frac{\Omega c}{\pi G \Sigma}$ *which is proportional to the Jeans-wavelength* $\lambda_J = \frac{c^2}{G\Sigma}$*. Lower plot: The critical value of the order parameter* β *vs Toomre parameter.*

ω the marginal curves $\beta_{cr}(k)$ can be computed from the dispersion relation for the real eigenvalue and the complex conjugate pair of eigenvalues. The marginal curve for viscous instability is given by $\omega = 0$ leading to the requirement that the absolute term of the dispersion relation should vanish, i.e.

$$\beta_{cr}^{vi}(k) = k\frac{2g - p_\sigma k}{3} - 1\,. \tag{3.52}$$

This curve is separating the (λ, β) plane in a region of viscous stability for $\beta > \beta_{cr}^{vi}(k)$ and instability for $\beta < \beta_{cr}^{vi}(k)$. The second marginal curve is for the two oscillatory modes (eq. (3.18,3.19), with $F_2 = F_3 = 0$ in an isothermal system)

$$\beta_{cr}(k) := \frac{1}{3}\left(\frac{\zeta}{\nu} - \frac{2}{3}\right) + \frac{1}{3}\left(\frac{4}{3} + \frac{\zeta}{\nu}\right)\left(p_\sigma k^2 - 2gk + \left[\frac{7}{3} + \frac{\zeta}{\nu}\right]\nu^2 k^4\right), \tag{3.53}$$

separating regions of viscous overstability $\beta > \beta_{cr}(k)$ and stability $\beta < \beta_{cr}(k)$. This critical curve is determined from the condition that the absolute term in the dispersion relation must equal the product of the coefficient of ω^1 and the coefficient of ω^2 (the criterion of Routh and Hurwitz). Both critical curves are shown in fig (3.4).

The marginal curve for viscous overstability has got a minimum if and only if $g > 0$, for a finite $k \equiv k_0$. The critical wavenumber is

$$k_0 = \frac{-6^{\frac{2}{3}} p_\sigma + 6^{\frac{1}{3}} \left(9 g \nu \sqrt{\frac{7}{3} + \frac{\zeta}{\nu}} + \sqrt{81(\frac{7}{3} + \frac{\zeta}{\nu}) g^2 \nu^2 + 6 p_\sigma^3}\right)^{\frac{2}{3}}}{6\nu \sqrt{\frac{7}{3} + \frac{\zeta}{\nu}} \left(9 g \nu \sqrt{\frac{7}{3} + \frac{\zeta}{\nu}} + \sqrt{81(\frac{7}{3} + \frac{\zeta}{\nu}) g^2 \nu^2 + 6 p_\sigma^3}\right)^{\frac{1}{3}}} \tag{3.54}$$

$$= \frac{g}{p_\sigma} - 2\frac{g^3}{p_\sigma^4}\left(\frac{7}{3} + \frac{\zeta}{\nu}\right)\nu^2 + O(g^4)\,. \tag{3.55}$$

Thus, the critical wavenumber is about half of the Jeans-wavenumber $k_J \equiv 2g/p_\sigma$. As shown in fig (3.4), upper right plot, the deviation is small even for large values of g. The smallness of the higher order terms in eq (3.55) comes from the simultaneous appearance of higher orders of the dimensionless kinematic shear viscosity ν which is in the example of fig (3.4) only about 0.3. Eq (3.54) inserted in eq (3.53) gives for the critical β

$$\beta_{cr}(k_0) = \frac{1}{3}\left(\frac{\zeta}{\nu} - \frac{2}{3}\right) - \frac{1}{3}\left(\frac{4}{3} + \frac{\zeta}{\nu}\right)\frac{g^2}{p_\sigma} + O(g^4)\,, \tag{3.56}$$

which is the asymptotic value (large λ) with a negative correction due to the self–gravity. The exact value is shown in fig (3.4, lower plot).

Expanding the dispersion relation in powers of $k - k_0$ and in powers of $\delta = \sqrt{(\beta - \beta_{cr})/\beta_{cr}}$ yields for the real part $r = \mathrm{Re}(\omega)$ of the overstable roots

$$r = c_6\delta^2 - c_7(k - k_0)^2 + O(\delta^3, (k - k_0)^3, (k - k_0)\delta^2) \tag{3.57}$$

with positive real constants c_6 and c_7 that depend on the parameters ν, ζ, p_σ, and g. Supposing that $\mathrm{Im}(\omega)$ represents the (inverse) fast time-scale t, from this equation the scaling is read for the slow time-scale θ represented by r, i.e. $\theta = \delta^2 t$. When additionally the spatial degree of freedom x is splitted in a slow and fast part the scaling becomes $X = \delta x$ yielding also the scaling for the amplitudes A in eq (3.49).

The two overstable eigenvalues of the matrix $\widehat{M}$ at marginal stability $\beta = \beta_{cr}(k)$ are purely imaginary, namely $\mp i\, s$ where s is given by eq (3.44). The corresponding marginal eigenvectors of (3.50) read

$$\varphi_1 = \begin{pmatrix} 2k(i\nu k^2 + s) \\ 2s(i\nu k^2 + s) \\ -i\, s + k^2\nu + \left[\frac{4}{3} + \frac{\zeta}{\nu}\right]\nu k^2(k^4\nu^2 + s^2) \end{pmatrix} \tag{3.58}$$

$$\varphi_2 = \begin{pmatrix} 2k(i\nu k^2 - s) \\ -2s(i\nu k^2 - s) \\ i\, s + k^2\nu + \left[\frac{4}{3} + \frac{\zeta}{\nu}\right]\nu k^2(k^4\nu^2 + s^2) \end{pmatrix}. \tag{3.59}$$

Thus, a solution in the overstable subspace of the linear problem at marginal stability reads[4]

$$\begin{pmatrix} \sigma \\ u \\ v \end{pmatrix} = A\,\varphi_1 \exp\{-i\, s\, t + i\, k\, x\} + B\,\varphi_2 \exp\{i\, s\, t + i\, k\, x\} + \text{c.c.}\,. \tag{3.60}$$

[4]The other eigensolution with growth rate $\omega^{(4)}$ [given by eq (3.22)] will decay rapidly for $\beta = \beta_{cr}(k)$.

For $A = 0$ or $B = 0$ these are left- or right moving waves

$$\begin{pmatrix} \sigma \\ u \\ v \end{pmatrix}_{\pm} \propto \tag{3.61}$$

$$\begin{pmatrix} \mp 2\,k[\,s\cos(s\,t \pm k\,x) + \nu k^2 \sin(s\,t \pm k\,x)] \\ 2\,s[s\cos(s\,t \pm k\,x) + \nu k^2 \sin(s\,t \pm k\,x)] \\ \cos(s\,t \pm k\,x)k^2\left[\nu + \left(\frac{4}{3}\nu + \zeta\right)\left(k^4\nu^2 + s^2\right)\right] - s\sin(s\,t \pm k\,x) \end{pmatrix}$$

and for $A = B$ standing wave solution is obtained

$$\begin{pmatrix} \sigma \\ u \\ v \end{pmatrix}_{S} \propto \tag{3.62}$$

$$\begin{pmatrix} 2k\sin(k\,x)[s\sin(s\,t) - \nu k^2\cos(s\,t)] \\ 2\cos(k\,x)s[s\cos(s\,t) + \nu k^2\sin(s\,t)] \\ \cos(k\,x)\left[\left\{\nu + \left(\frac{4}{3}\nu + \zeta\right)\left(k^4\nu^2 + s^2\right)\right\}k^2\cos(s\,t) - s\sin(s\,t)\right] \end{pmatrix}.$$

In the limit of long wavelengths these solutions yield the simple phase shifts in the variables given in table (3.1). For a velocity dispersion in the order of mm/s and an Keplerian

Spatial phase differences

	Standing wave	Left traveling	Right traveling
Ph(σ)-Ph(u):	$\pm\frac{\pi}{2}$	π	0
Ph(σ)-Ph(v):	$-\frac{\pi}{2}$	$-\frac{\pi}{2}$	$-\frac{\pi}{2}$
Ph(u)-Ph(v):	0,π	$\frac{\pi}{2}$	$-\frac{\pi}{2}$

Table 3.1: *Phase shifts for long wavelength overstable modulations of the state variables for standing waves and left and right moving traveling waves.*

frequency $\Omega = 2{\cdot}10^{-4}\,\mathrm{s}^{-1}$ all wavelengths larger than about 30 m correspond to dimensionless wavenumbers $k < 1$ and already for $\lambda = 300\,\mathrm{m}$ k^2 is only about 1%. These phase shifts of the marginal eigenfunctions will be compared in chapter 5 to the phaseshifts of the state variables observed in simulations. Other properties of the marginal eigensolutions that can be checked by simulations are the ratios of the amplitudes: the perturbations in the radial velocity are about double in size then those in the tangential velocity, and interestingly the ratio of the density amplitude to the velocity amplitudes depends on wavelength.

3.3.4 Second Order Solution

With the solution of the linear order the next steps in the derivation of the Landau equation can be addressed, namely the computation of the inhomogeneity at second order, the solvability condition, and the solution ψ_2 of the second order equation.

Take as a solution of the linear order a superposition of left and right moving modes ($k > 0$) (3.58)

$$\psi_1 = A_R(\theta)\varphi_1(k)\exp\{-i\,s\,t + ikx\} + A_L(\theta)\varphi_1(-k)\exp\{-i\,s\,t - ikx\} + \text{c.c.} \tag{3.63}$$

with slowly in time varying amplitude functions $A_R(\theta)$ and $A_L(\theta)$. With ψ_1 one can write down the inhomogeneity $N_2(\psi_1, \psi_1)$ of the second order equation in (3.37)

$$N_2 = \tag{3.64}$$

$$A_L(\theta)^2\,(i\,k^2\nu+s)^2\,2k\,\exp\{-2i\,k\,x\;-2i\,s\,t\}$$
$$\times\begin{pmatrix} -4\,ik\,s \\ 2\left(is^2+k^2\left\{-ip_\sigma+\left[\frac{4}{3}+\frac{\zeta}{\nu}\right](1+2\beta_{cr})\,\nu\,s\right\}\right) \\ \left[\frac{4}{3}+\frac{\zeta}{\nu}\right]k^2\nu(s-i\,k^2\nu)(k^2\nu(1+2\beta_{cr})+i\,s)+s-i\,k^2\nu(4+\beta_{cr}(2-3\beta_{cr})) \end{pmatrix}$$
$$+A_R(\theta)^2\,(i\,k^2\nu+s)^2\,2k\,\exp\{2i\,k\,x\;-2i\,s\,t\}$$
$$\times\begin{pmatrix} -4\,ik\,s \\ -2\left(is^2+k^2\left\{-ip_\sigma+\left[\frac{4}{3}+\frac{\zeta}{\nu}\right](1+2\beta_{cr})\,\nu\,s\right\}\right) \\ \left[\frac{4}{3}+\frac{\zeta}{\nu}\right]k^2\nu(i\,k^2\nu-s)(k^2\nu(1+2\beta_{cr})+i\,s)-s+i\,k^2\nu(4+\beta_{cr}(2-3\beta_{cr})) \end{pmatrix}$$
$$+A_R(\theta)A_L^*(\theta)\,(k^4\nu^2+s^2)\,4\,ik\,\exp\{2i\,k\,x\}$$
$$\times\begin{pmatrix} 0 \\ -2(k^2p_\sigma+s^2) \\ -\left[\frac{4}{3}+\frac{\zeta}{\nu}\right]k^2\nu((1+2\beta_{cr})k^4\nu^2+s^2)-k^2\nu(4+\beta_{cr}(2-3\beta_{cr})) \end{pmatrix}$$
$$+3\,\beta_1\,k^2\,\nu(k^2\nu-is)\,[\,A_R(\theta)\,\exp\{i\,k\,x-i\,s\,t\}+\;A_L(\theta)\,\exp\{-i\,k\,x-i\,s\,t\}]\begin{pmatrix}0\\0\\1\end{pmatrix}$$
$$+4\,k\,s\,(k^4\nu^2+s^2)\left(|A_R(\theta)|^2-|A_L(\theta)|^2\right)\begin{pmatrix}0\\ 2k^2\nu\left[\frac{4}{3}+\frac{\zeta}{\nu}\right]\\ 1\end{pmatrix}$$
$$+\text{c.c.}\,.$$

With the null eigenfunction of $L^\dagger$ [eq (3.43)]

$$\psi_{0,1}^{ad}=\varphi_{0,1}^{ad}\exp\{-i\,s\,t+i\,k\,x\} \tag{3.65}$$

the solvability condition at this order

$$\langle\psi_{0,1}^{ad}|N_2(\psi_1,\psi_1)\rangle\equiv 0 \tag{3.66}$$

can be computed. In view of the definition (3.41) it is clear that only terms proportional to $\exp\{\pm i\,s\,t\pm i\,k\,x\}$ can survive the evaluation of the scalar product, thus the remaining condition reads

$$0=6\beta_1k^2\nu(k^2\nu-i\,s)A_R(\theta) \tag{3.67}$$

i.e. $\beta_1=0$. A similar equation for the amplitude $A_L(\theta)$ is obtained with $\psi_{0,2}$.

In the next step a particular solution ψ_2 of the inhomogeneous linear second order equation in (3.37) can be computed with the ansatz

$$\begin{aligned}\psi_2 \;=\;& h_1(k)\left(|A_R(\theta)|^2-|A_L(\theta)|^2\right)+h_2(k)A_L(\theta)^2\exp\{-2i\,k\,x\;-2i\,s\,t\}\\ &+h_3(k)A_R(\theta)^2\exp\{2i\,k\,x\;-2i\,s\,t\}+h_4(k)A_R(\theta)\,A_L^*(\theta)\exp\{2\,i\,k\,x\}\\ &+\text{c.c.}\quad.\end{aligned} \tag{3.68}$$

It is straightforward but lengthy to compute the coefficient functions $h_i(k)$ from (3.64) and (3.37). They contain many terms and will therefore not be displayed here. An arbitrary superposition of the first order solutions (3.58, 3.59) may be added to (3.68) in order to obtain a general solution of the inhomogeneous second order equation in (3.37). It turns out that only the particular solution (3.68) contributes to the solvability condition at third order, and thus, to the Landau equation.

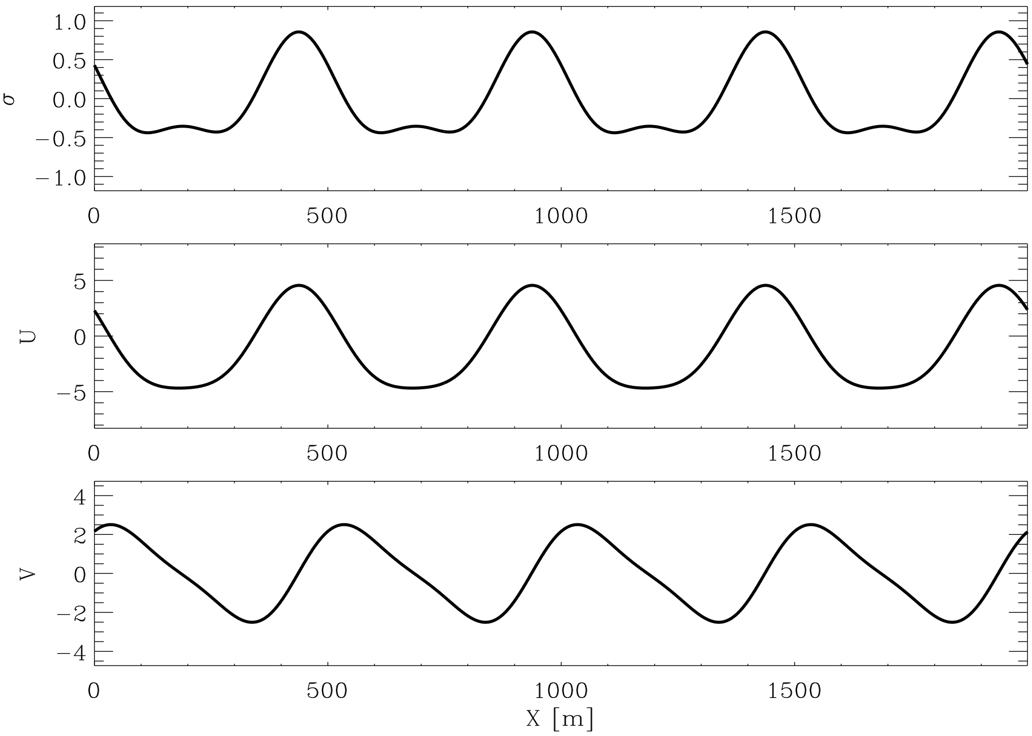

Figure 3.5: *Snapshot of the solutions $\psi = \psi_1 + \delta\psi_2$ for the state variables for a traveling wave. The typical effect of the nonlinearity at first order in δ is a sharpening of the wave crests and a flattening of the perturbation minima.*

In fig (3.5) the superposition $\psi = \psi_1 + \delta\psi_2$ of the first and second order solution with $A_L = 0$ (right traveling wave) is shown for a perturbation with wavelength $\lambda = 200\,\mathrm{m}$. For $|A_R|$ the saturated value following from eq (3.77) is used. The basic effect of the nonlinearity in second order is a driving of the system with the harmonics $\exp\{\pm 2\,i\,k\,x \pm 2\,i\,s\,t\}$ of the linear modes. This results in a sharpening of the wave crests and a flattening of the minima for the perturbations in the density and the radial velocity. The perturbations of the tangential velocity steepen at the back (right moving waves) of the wave crest and the front is flattened. As parameters the values $\nu = 5.4 \cdot 10^{-3}\,\mathrm{m}^2/\mathrm{s}$, $\zeta/\nu = 2$, $\Sigma = 300\ \mathrm{kg/m}^2$, $\Omega = 1.94 \cdot 10^{-4\,\mathrm{s}^{-1}}$, $c = 2 \cdot 10^{-3}\,\mathrm{m}^2/\mathrm{s}^2$, and $p_\sigma = 1$ are used in this case, resulting in a critical value $\beta_{cr}(\lambda_{cr}) = 0.42$. The actual β used as parameter for that plot was 0.6. Fig (3.6) shows a similar plot for a standing wave solution with $A_R = A_L$ at 8 time steps over one orbital period. Here, the perturbations are maximal twice per oscillation period [eq (3.44)] which is in this self–gravitating case slightly larger than the Keplerian period.

3.3.5 Third Order Solvability Condition and Amplitude Equations

With the solutions of the linear order ψ_1 and the second order ψ_2 the inhomogeneity of the third order equation can be written down, and thus, the solvability condition for the third order

$$\langle \psi_{0,1}^{ad} | N_3(\psi_1, \psi_2) + \partial_\theta \psi_1 \rangle \equiv 0 \tag{3.69}$$

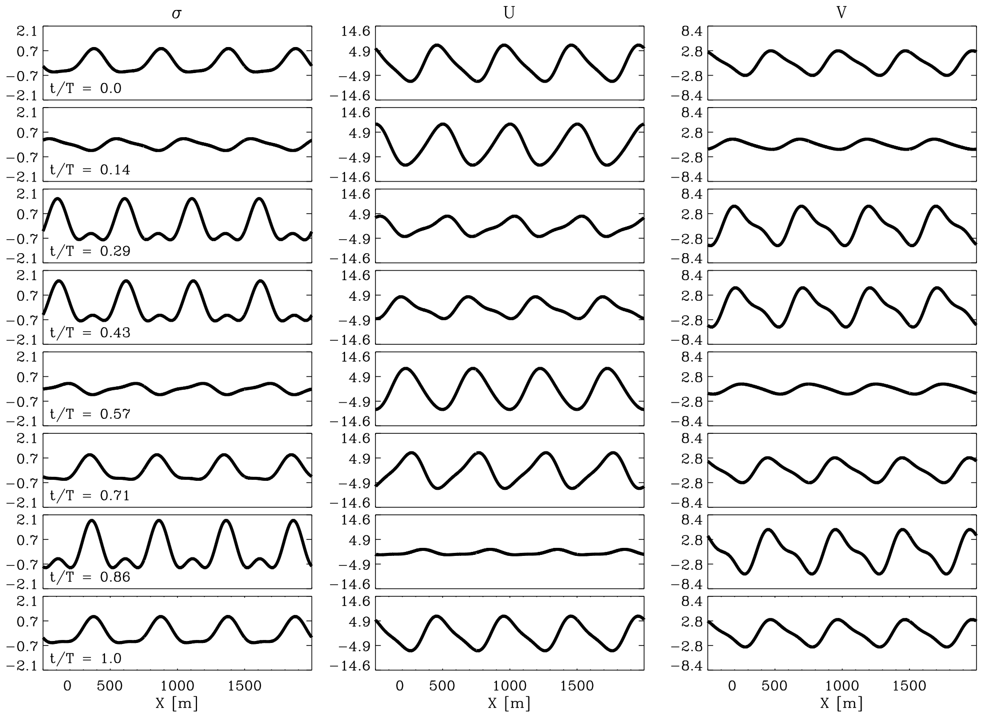

Figure 3.6: *Solutions for the state variables $\psi = \psi_1 + \delta\psi_2$ for a standing wave. The sequence of plots downward shows the time development within one Keplerian period T.*

leading with the adjoint null solutions (3.43) to the complex Landau equations (3.49) for the complex amplitudes A_R and A_L with explicit expressions for the coefficient functions c_i. Again these coefficient functions contain a vast number of terms, basically sums of complicated combinations of the components of the eigenvectors (3.58) and (3.45), and will therefore not be displayed here. Instead, the effect of the real and imaginary parts of the c_i on the solutions of the Landau equation is discussed in general terms and the particular coefficients for the system of hydrodynamic equations under consideration will be displayed graphically for different wavelengths. From eq (3.31) and $\beta_1 = 0$ [eq (3.67)] it follows that in second order accuracy

$$\beta = \beta_{cr} + \delta^2 \beta_2 \tag{3.70}$$

and with

$$\delta^2 = \frac{\beta - \beta_{cr}}{\beta_{cr}} \tag{3.71}$$

the consistency of the expansion requires $\beta_2 = \beta_{cr}$.

The case $A_L \equiv 0$
For a single traveling wave the amplitude equation has the general form

$$\partial_\theta A = (g_r + i g_i)A - (l_r + i l_i)|A|^2 A\,, \tag{3.72}$$

with real parameters g_r, g_i, l_r, and l_i. Returning to un–scaled units $\delta^2\partial_\theta = \partial_t$ and $A\delta = \widetilde{A}$ leads to

$$\partial_t\widetilde{A} = \delta^2(g_r + ig_i)\widetilde{A} - (l_r + il_i)|\widetilde{A}|^2\widetilde{A}\,. \tag{3.73}$$

Dropping the tildes again and replacing $A(t) = |A(t)|\exp\{i\chi(t)\}$ yields separate equations for the modulus of the amplitude and the phase $\chi(t)$

$$\partial_t|A| = \delta^2 g_r|A| - l_r|A|^3 \tag{3.74}$$

$$\partial_t\chi = \delta^2 g_i - l_i|A|^2 \tag{3.75}$$

In the case of a positive g_r and a positive Landau constant l_r small initial amplitudes A_0 will first grow exponentially for $\beta > \beta_{cr}$ with growth rate $\delta^2\, g_r$ until the increasing influence of the cubic term will saturate the growth. In this case (supercritical saturation) the solution is

$$|A| = \pm\frac{A_0\exp\{g_r\delta^2 t\}}{\sqrt{1 + \left(\frac{A_0}{\delta}\right)^2\frac{l_r}{g_r}\left(\exp\{2g_r\delta^2 t\} - 1\right)}} \tag{3.76}$$

$$\longrightarrow \pm\delta\sqrt{\frac{g_r}{l_r}}, \quad \text{as } t\to\infty \tag{3.77}$$

The solution of the equation for the phase is

$$\chi = \chi_0 + g_i\delta^2 t - \frac{l_i}{2l_r}\ln\left[1 + \left(\frac{A_0}{\delta}\right)^2\frac{l_r}{g_r}\left(\exp\{2g_r\delta^2 t\} - 1\right)\right] \tag{3.78}$$

$$\longrightarrow \chi_0 - \frac{l_i}{2l_r}\ln\left[\left(\frac{A_0}{\delta}\right)^2\frac{l_r}{g_r}\right] + \left(g_i - l_i\frac{g_r}{l_r}\right)\delta^2 t \tag{3.79}$$

i.e. the saturated solution $\propto \exp\{i\chi\}$ oscillates with a frequency that is shifted by

$$\Delta s = \left(\frac{g_i}{g_r} - \frac{l_i}{l_r}\right) g_r\,\delta^2\,, \tag{3.80}$$

as compared to the linear modes.

The case $A_R \neq 0, A_L \neq 0$

When left and right traveling waves are present the growth of their respective amplitudes in the weakly nonlinear regime is governed by the coupled Landau equations

$$\begin{aligned}\partial_t A_R &= \delta^2(g_r + i\,g_i)A_R - (l_r + i\,l_i)|A_R|^2 A_R - (w_r + i\,w_i)|A_L|^2 A_R \\ \partial_t A_L &= \delta^2(g_r + i\,g_i)A_L - (l_r + i\,l_i)|A_L|^2 A_L - (w_r + i\,w_i)|A_R|^2 A_L\,.\end{aligned} \tag{3.81}$$

The coefficients of the linear term are given by the growth rates of the linear stability problem. The nonlinear terms lead to a saturation of the amplitude if $w_r/l_r > -1$, and to nonlinear frequency pulling. Standing waves are unstable if $w_r/l_r > 1$ and stable if $-1 < w_r/l_r < 1$ (Cross & Hohenberg, 1993).

Coefficients of the Landau Equation

Various reasonable sets of parameters Σ, c, ν, and ζ/ν are employed to evaluate the coefficients of the Landau equations (3.81) for the hydrodynamic equations (3.27) for $\Omega =$

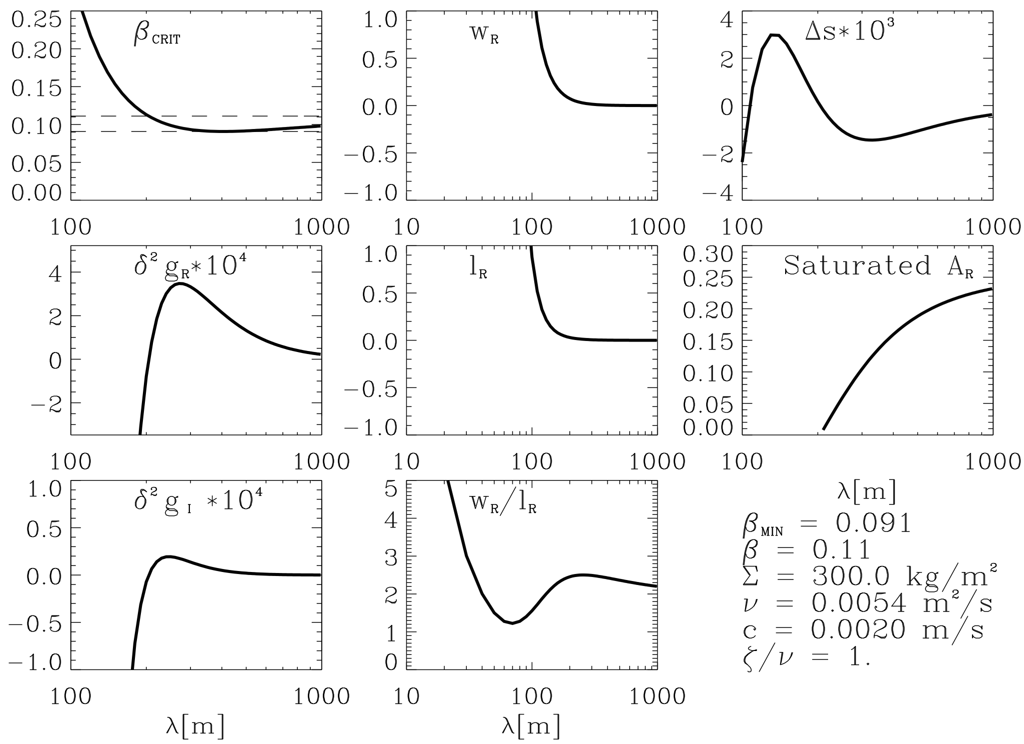

Figure 3.7: *Coefficients of the Landau equation (3.81) vs wavelength (among other quantities). The ratio w_r/l_r is always larger than one, indicating that standing wave solutions will be unstable in the nonlinearly saturated state of the system. Also shown is the value for the saturated amplitude of a single traveling wave and the marginal curve with the critical β and the value that has been taken for the computation of the plots. The nonlinear frequency pulling (3.80) is labeled with Δs.*

$2 \cdot 10^{-4}\,\mathrm{s}^{-1}$. The real parts of the cubic terms l_r and w_r [as defined by eq (3.81)] are always found to be positive at all wavelengths. This implies the saturation of the growth of the linear oscillatory instability of the system. The ratio w_r/l_r is always larger than one (except for systems with very low surface density in the *stable* range of wavelengths, see discussion of figures below), i.e. standing waves will be unstable, traveling waves stable in this system. This ratio approaches a value of two for large wavelength.

In fig (3.7) values for the coefficients of the Landau equations (3.81) are shown for the set of parameters displayed in the figure. In this case overstability sets in first at a wavelength of about 200 m. The chosen value $\beta = 0.11$ corresponds to the marginal β at large wavelengths given by eq (3.21). The line of marginal stability is drawn for reference in the first plot. The quantity $\delta^2 g_r$ is an approximation to the real part of the growth rate of overstability as it follows from the dispersion relation (3.51) of the linear analysis. Similarly, $\delta^2 g_i$ is the correction to the frequency of overstable oscillations (3.44) at marginal stability due to the distance δ of that line. Both are correct to second order in δ. For the parameters of fig (3.7) these values are practically the same as the exact values from the numerical computation of the roots of the dispersion relation (3.51), providing a check for the correctness of the derivation of the coefficients of the Landau equation in the previous sections. Even for

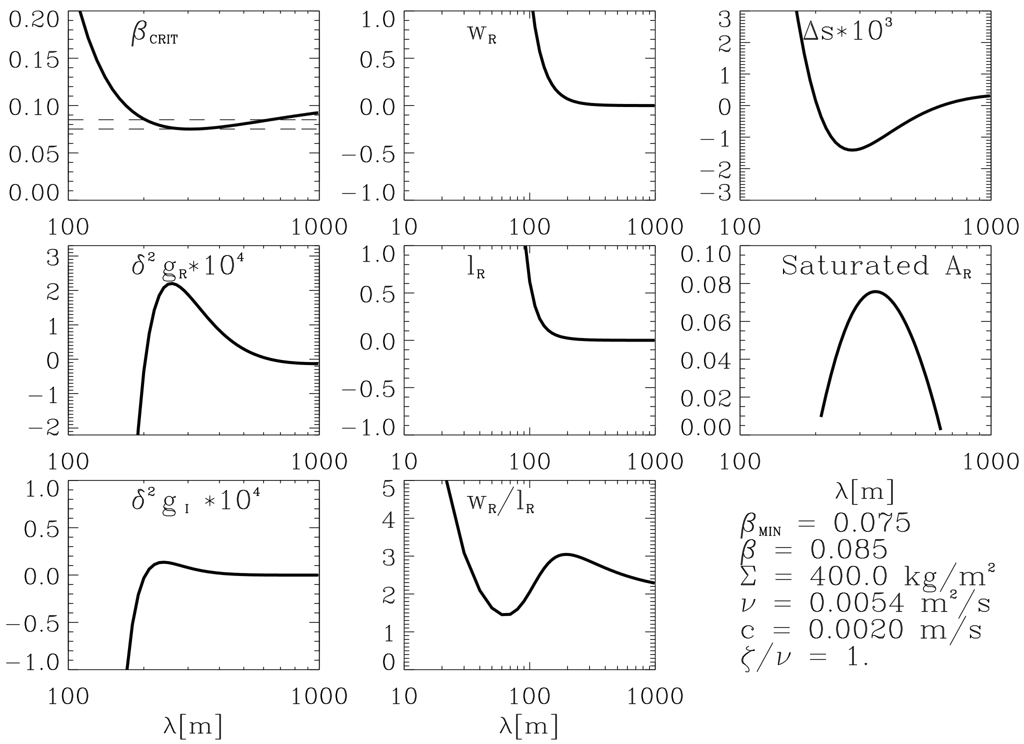

Figure 3.8: *Coefficients of the Landau equation for a system where the instability is restricted to a range of wavelengths.*

larger β with a δ near one the deviations are at most 10% for the growth rate of the fastest growing wavelength. Also shown is the saturated amplitude according to eq (3.77) of a single traveling wave. The nonlinear frequency shift (3.80), shown in the upper right plot of this figure, is always small compared to the frequency of the linear modes (3.44) which is of order one (in units of the Keplerian frequency).

An interesting case is a self–gravitating system with a β that is smaller than the marginal value at large wavelength [eq (3.21)] but larger than than the critical value given by eq (3.56). In this case, shown in fig (3.8), the growth of overstable modes is restricted to a certain range of wavelengths with a maximal amplitude of the saturated mode in between. Also in this case all overstable modes saturate and form traveling waves eventually.

A non–selfgravitating system ($\Sigma = 0$) is shown in fig (3.9). In this case the ratio w_r/l_r is smaller than one in a small range of wavelengths *below* the critical wavelength for overstability. Note that $\Sigma = 0$ does not necessarily imply $\tau = 0$ but can also be seen as the limit of a small particle bulk density at finite optical depth. In the simulation of such a system then the influence of self–gravity can be mimicked by the enhancement of the frequency of vertical oscillations (see chapter 4). This is the method that will be employed for the comparison of simulations and theory in chapter 5. Such an enhanced frequency of vertical oscillations would influence the behavior of the system via a change in the transport properties.

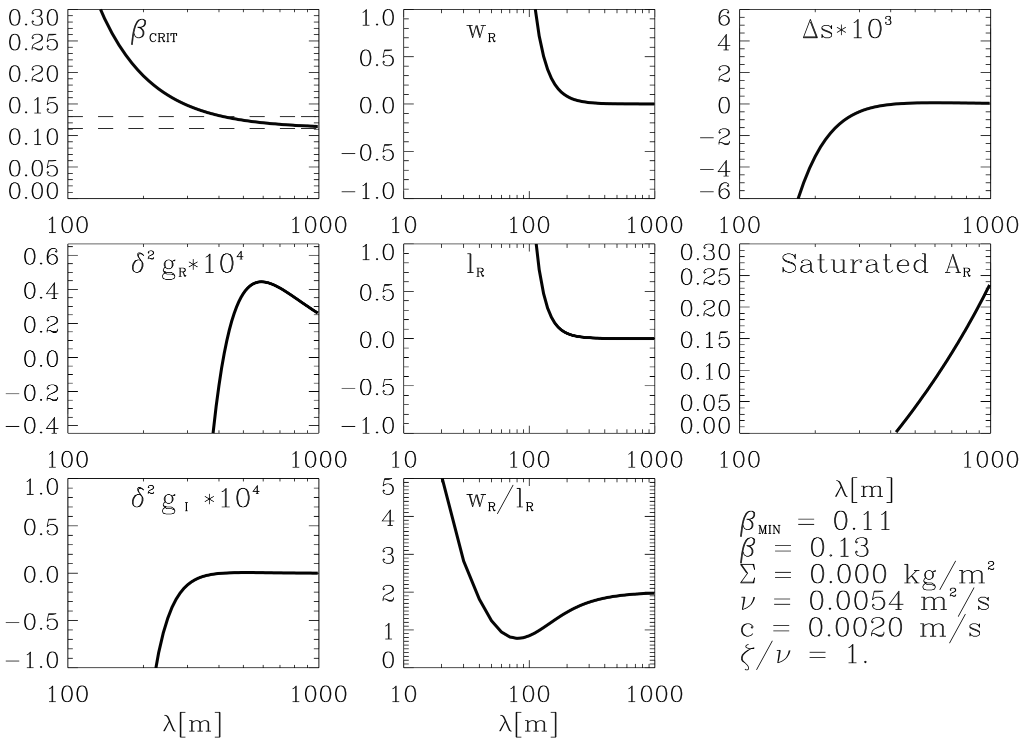

Figure 3.9: *Coefficients of the Landau equation for a non–selfgravitating system.*

3.3.6 Summary

The weakly nonlinear stability analysis of the isothermal hydrodynamic equations (3.27) yields a complex Landau equation for the growth of the amplitude of small perturbations of the purely Keplerian flow field. The coefficients of the Landau equation have magnitudes and signs that predict

- **nonlinear saturation** of the growth of the oscillatory instability
- the **instability of standing wave solutions** with respect to traveling waves as the nonlinearly saturated solutions.

Further, the analysis includes the derivation of **marginal eigenfunctions** with

- **characteristic phase differences** of the state variables
- **wavelength dependent relative amplitudes**
- **nonlinear corrections** that are first order in δ.

The results of this chapter are of *qualitative* relevance for the comparison to simulations. The small values of β used here (to be near threshold and guarantee the applicability of a weakly nonlinear analysis) are clearly unrealistic for dense rings of high optical depth. But when the (also unrealistic) assumption of isothermality is dropped, the line of marginal stability is found to be shifted to significantly higher values of β (see chapter 3.2 and 5).

In particular for the simulated rings investigated in chapter 5 the stability boundary seems to be near $\tau = 1$, rings with lower optical depth being stable. Thus, there are simulated systems around $\tau = 1$ with plausible parameters that are naturally in a weakly nonlinear state.

The isothermal model is employed for the computations in this section for simplicity. Of course, the next step was now to generalize the procedure to the non–isothermal case. For the purpose of this thesis it is assumed that the conclusions from the weakly nonlinear stability of the isothermal model hold qualitatively for the non–isothermal system.

Chapter 4

Simulations

Oscillatory perturbations in density and velocities with growing amplitudes, similar to the predictions of the isothermal model by Schmit & Tscharnuter (1995), are indeed observed in molecular dynamics simulations (Salo et al., 2000b). However, there are qualitative and quantitative differences between that model and the simulations. First, the simulations only show overstability when self–gravity is taken into account, for rings with optical depth $\tau = 1$ and larger, and no overstability is observed for simulated rings with optical depth smaller than $\tau = 0.8$. In contrast, the model predicts overstability for these lower density rings too, and most importantly also in the absence of self–gravity. Second, the growth rates of the model are by roughly a factor of 10 to large.

This discrepancy was the motivation for the study of the influence of the energy balance equation on the stability of a planetary ring as presented in chapter 3. The basic problem for a quantitative comparison between the results of chapter 3 and the simulations is the large number of poorly known parameters of the non–isothermal model. The estimation of some of these quantities in section 3.2 with transport coefficients from hard sphere gas theory and the equation of state of an ideal gas may merely give a hint on the qualitative influence of the energy equation as compared to the isothermal model. For a quantitative comparison this estimation is too crude. This motivates the determination of appropriate values for the parameters of the model directly from the simulated rings themselves. The methods devised in a paper by Salo (Salo et al., 2000a) for the evaluation of the transport coefficients from the simulations and other quantities needed are described in section 4.3 of this chapter. But first a brief description of the simulational method and the necessary assumptions and simplifications that are made is given in section 4.1 and a more detailed presentation of the overstability as observed in the simulations in section 4.2.

4.1 Method

The simulations employ a local simulation method that was first applied to planetary rings by Wisdom & Tremaine (1988). The local simulation method is described in detail for instance in (Salo, 1995).

A rectangular domain of the rings is simulated, co–moving with the local Keplerian angular velocity, with periodic boundary conditions in the circumferential direction. In the radial direction the boundaries are also periodic but modified to take into account the difference in Keplerian velocity over the radial length of the domain. The particle trajectories are calculated by numerical integration of the linearized equations of motion (Hill, 1878)

$$\ddot{x} - 2\Omega\dot{y} - 3\Omega^2 x = F_x \qquad (4.1)$$

$$\ddot{y} + 2\Omega\dot{x} = F_y$$
$$\ddot{z} + \Omega_z^2 z = F_z ,$$

expressed in a Cartesian frame that rotates with the simulation box at the distance r_0 around the central planet of mass M with angular velocity $\Omega = \sqrt{GM/r_0^3}$. The x–axis points in the radial direction and the y–axis in the direction of orbital motion. The force $\vec{F}$ on the right hand side includes for instance the self–gravity between the particles.

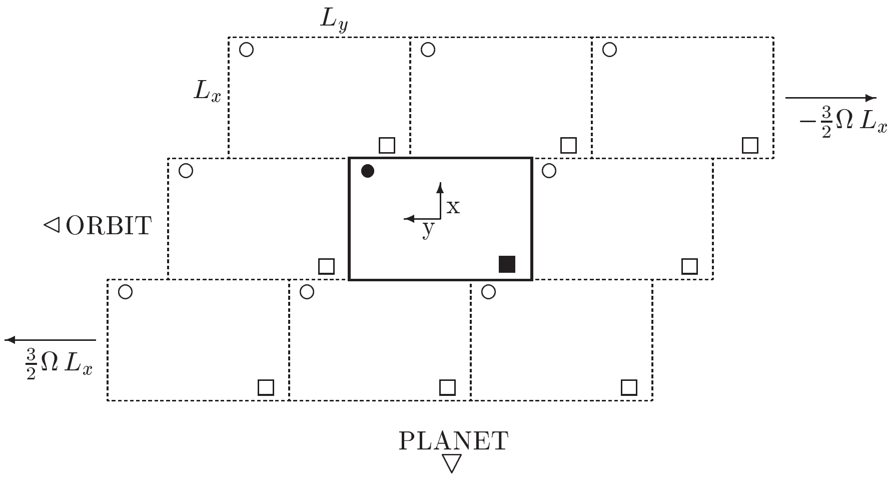

Figure 4.1: *The simulated domain with its replicas. In the co–moving coordinate frame with origin in the original simulation box the upper replica boxes move to the right the lower ones to the left due to the differential rotation. Two example–particles are in the box, indicated by the filled circle and the filled square. The circle particle may collide with the image particle of the squared particle in the replica box. The gravitational interaction between the filled particles is small compared to those between actual particles and image particles.*

At a given time step the code first constructs a table of potentially colliding pairs of particles from their positions and velocities. The pair that will collide next is chosen from the list and their post–collisional velocities are calculated from the pre–collisional ones according to a given dissipative impact model for smooth, uni–sized, spherical particles, i.e. the normal component of the relative velocity is damped by the coefficient of restitution. The collision itself is assumed to take place on a time scale that is much shorter than the mean flight time between impacts. Thus, the impact can be considered to happen instantaneously (event driven method). The collision table is then updated with the new particle coordinates and velocities and the next collision is carried out until the table is empty. The next time step continues by constructing a new list of collision pairs. The size of the calculation region is chosen to be much larger than the typical mean free path between impacts.

To allow for a correct detection of impact pairs over the periodic boundaries and the calculation of the near field self–gravity identical replicas of the simulation domain are introduced that surround the original cell. To account for the shearing motion eight replicas are necessary [fig (4.1)]. Every time a particle leaves the simulation box a mirror particle enters the box. The replica boxes located radially outward move with the velocity $-\frac{3}{2}\Omega\, L_x$ relative to the simulated region, those located nearer to the planet with velocity $\frac{3}{2}\Omega\, L_x$. In this sense the radial boundary is periodic but takes into account velocity differences due to the differential rotation. The 2D periodicity of any pattern in the box is only preserved in a non-rectangular coordinate system where the x–axis (initially radial) gets more and more inclined to the radial direction with the shearing motion of the system.

For the smooth (i.e. no surface friction) uni–sized particles considered in the model (no particle spin) the post–collisional velocities are calculated from the pre–collisional ones according to the formula

$$\vec{v}'_{1,2} = \vec{v}_{1,2} \mp \frac{1+\epsilon}{2}(\vec{g}\cdot\vec{n})\vec{n} \tag{4.2}$$

where ϵ is the coefficient of restitution, $(\vec{g}\cdot\vec{n})\vec{n}$ is the normal component of the relative velocity

$$\vec{g} = \vec{v}_1 - \vec{v}_2 \tag{4.3}$$

in the impact and $\vec{n}$ is the unit vector pointing from the center of particle 2 to the center of particle 1 at the moment of impact. The energy loss in the impact is then

$$\Delta E = \frac{1}{4}(1-\epsilon^2)(\vec{g}\cdot\vec{n})^2 \,. \tag{4.4}$$

For the purpose of the current study a velocity dependent coefficient of restitution is used that was determined in low temperature collision experiments for ice spheres by Bridges et al. (1984)

$$\epsilon(\vec{v}\cdot\vec{n}) = \left(\frac{\vec{v}\cdot\vec{n}}{v_B}\right)^{-0.234} \tag{4.5}$$

where $v_B \approx 0.01\,\mathrm{cm/s}$ is the velocity where impacts become totally elastic. Even for comparatively small impact velocities equation (4.5) predicts a fairly large dissipation. The fact that the coefficient of restitution depends on the impact velocity as a power law is consistent with theoretical models of the impact of granular grains that assign the energy loss to visco–elastic dissipation (Brilliantov et al., 1996) or to plastic deformation (Andrews, 1930; Thornton, 1997).

The self–gravity of the particles can be treated in several ways in the simulations. The simplest idea was already applied in the first study of rings with the local simulation method by Wisdom & Tremaine (1988). The particles' self–gravity in eq (4.1) will in general amplify the action of the vertical component of the central gravity and, thus, increase the frequency of vertical oscillations. Hence, the effect of self–gravity on the ring can be mimicked by an increase of that frequency Ω_z and zero forces F_i on the right hand side of eq (4.1). In the literature often a value $\Omega_z = 3.6\Omega$ has been used (Wisdom & Tremaine, 1988; Salo, 1991). For this reason the same factor is used here. Another possibility to approximate the self–gravity is to discard the planar components of the gravity and compute the vertical force F_z from the vertical density profile of the simulation self–consistently as

$$F_z(z) = -2\pi G \int_{-z}^{z} \mathrm{d}z'\,\varrho(z')\,, \tag{4.6}$$

Following from the Poisson equation. These approximate methods merely consider the effect of the vertical self–gravity, which leads in both cases to an enhancement of the collision frequency and a flattening of the ring when compared to non–selfgravitating systems. For high enough optical depth the system then starts to form a multi-layer structure as already found by Wisdom & Tremaine (1988). The most sophisticated way to include self–gravity (also the most CPU–time consuming) is the inclusion of the direct particle–particles forces. This method is efficient for high particle numbers when the net force exerted on a particle by regions outside a given radius around the particle is approximated as a mean–field (Salo, 1995). This contribution can be computed from the instantaneous density pattern of the simulation box extrapolated for an extended doubly periodic system using its Fourier transform. The particle–particle self–gravity method leads to additional effects as compared to the inclusion of solely the vertical self–gravity which are to be expected accordingly in the Saturnian rings. Namely, the close gravitational encounters of particles, much alike elastic collisions, maintain a significantly higher velocity dispersion in comparison to non–selfgravitating systems under otherwise the same conditions. Second, under conditions that are plausible for the Saturnian rings (in particular the A ring) the simulated systems form Julian–Toomre like gravitational wakes (Julian & Toomre, 1966; Salo, 1992b).

4.2 Overstability in Simulations

The simulations (Salo et al., 2000b) show overstability when self-gravity is taken into account leading to a flattening of the ring. Overstability is observed for different ways of incorporating the self–gravity in the simulations, i.e. full particle-particle gravity interaction or mimicking the effect of gravity with an enhancement of the frequency of vertical oscillations $\Omega_z/\Omega > 1$ [see eq (4.1)]. In fig (4.2) results from simulations with true particle–particle

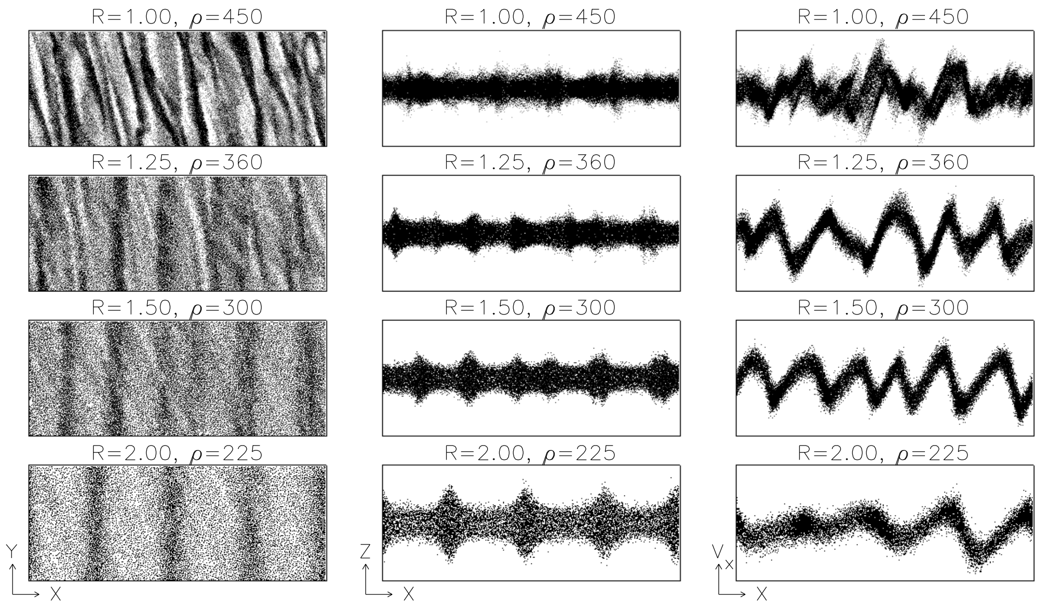

Figure 4.2: *Left: Examples from molecular dynamics simulations with true particle–particle self–gravity showing gravitational wakes and radial structure due to viscous overstability simultaneously. The particle radius R and the material density ρ (values are given in the plot in units of m and kg/m^3, respectively) are varied for a fixed surface density of* $\sigma = 840\,kg/m^2$. *Middle: The same simulated systems shown from aside (the vertical range is about 20 particle radii) showing the vertical splashing at the density enhancements of the overstable modes as envisioned in Borderies et al. (1985). Right: The profile of the radial velocity with a vertical range of about* ± 1 *cm/s.*

self–gravity are pictured with gravitational wakes and radial structure due to viscous overstability appearing simultaneously. The distance to Saturn is 100,000 km and the optical depth is fixed to $\tau = 1.4$. The material density ρ and the particle radius R are varied for a fixed surface density of $\sigma = 840\,\mathrm{kg/m^2}$. As the particles' material density decreases, the non-axisymmetric wake structure gets weaker, and the purely radial overstable oscillations are more pronounced. A Fourier analysis of the surface density indicates that wakes are also present in the lower–most frame, while overstability is present also in the upper frame. The simulated systems are vertically more extended at the density enhancements of the overstable modes as envisioned in Borderies et al. (1985). Radial oscillations are also seen in the radial profiles of the radial and (shear corrected) tangential velocities of the particles.

Similar overstable perturbations are observed in a system where $\Omega_z/\Omega > 1$, indicating that overstability is not bound to the self–gravity itself but rather to the corresponding changes in the viscous properties of the system. A simulational example for $\tau = 1$ is

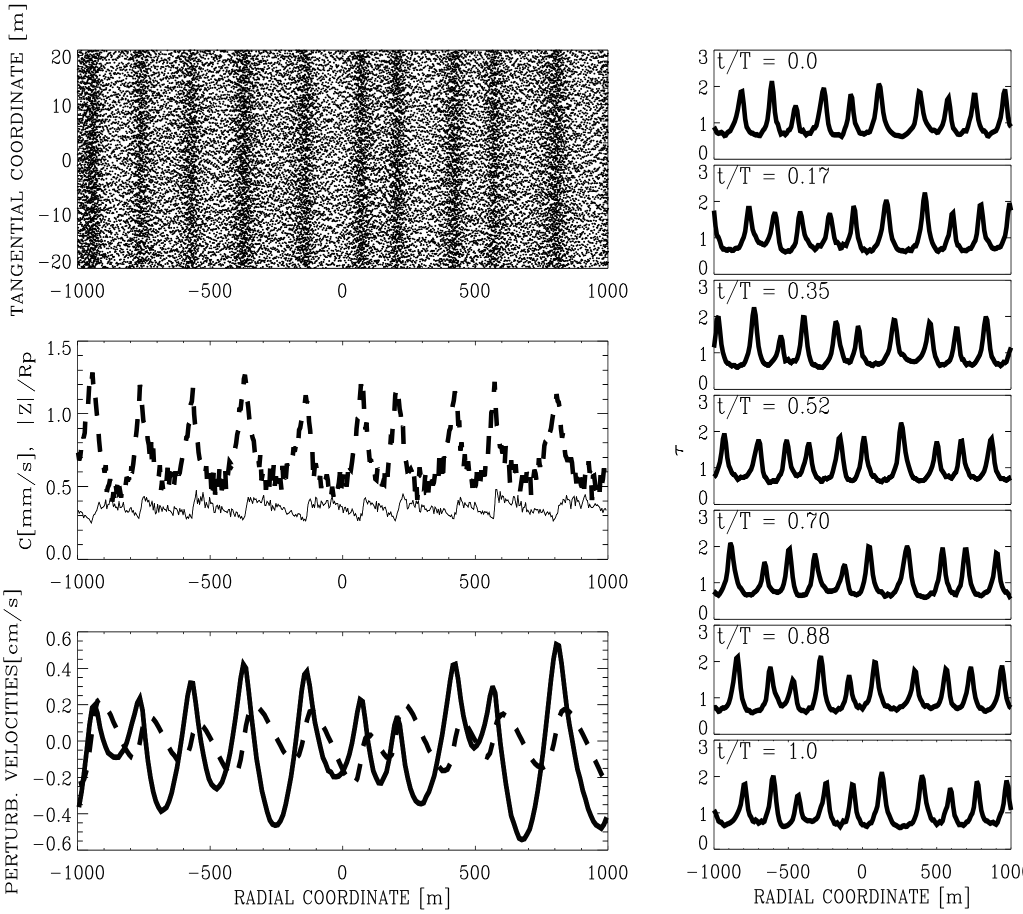

Figure 4.3: *Left: Perturbations of density (projected particle positions), velocity dispersion (thin solid line), ring thickness (thick dashed, R_p is the particle diameter), tangential (dashed), and radial velocity (solid) from a simulation with $\tau = 1$ and self–gravity modeled by a vertical frequency enhancement. Right: Time development of the radial optical depth profile for the same simulation after about 900 orbits.*

displayed in fig (4.3). A snapshot is shown of radial undulations in optical depth, scale height, velocity dispersion, and radial and tangential velocities. The perturbations in radial velocity have roughly the double amplitude of those in the tangential velocity. The spatial oscillations in the radial velocity and in the optical depth are in phase, while the oscillations in the velocities are shifted by about $\frac{\pi}{2}$. These observations are consistent with results from chapter (3.3) for traveling wave solutions [see eq (3.61) and table (3.1)]. A more detailed comparison of the simulational systems to the theoretical results is deferred to chapter (5).

4.3 Determination of Model Parameters in Simulations

The dispersion relation for the non–isothermal model obtained in chapter 3 in dimensionless form

$$\begin{aligned} 0 = \quad & p_{\mathrm{T}} k^2 \left(-k^2 \left(\tfrac{2}{3}\Gamma_\sigma \nu + \tfrac{3}{2}(1+\beta)\nu^2 \right) + \left(-\tfrac{2}{3}\Gamma_\sigma + \tfrac{1+3\beta}{2}\nu + \tfrac{2}{3}k^2 \nu p \right) \omega + \tfrac{2}{3} p \omega^2 \right) \\ + \quad & 3\eta_{\mathrm{T}} k^2 \left(-\tfrac{2}{3}\Gamma_\sigma + \tfrac{3}{2}(1+\beta)\nu + p_\sigma k^2 \nu - 2k\nu g + \nu\omega^2 + \omega \left(\tfrac{2}{3} p + k^2 \nu \left(\tfrac{4}{3}\nu + \zeta \right) \right) \right) \\ + \quad & D_{iso} \left(E_{\mathrm{T}} + \tfrac{2}{3} k^2 \kappa + \omega \right) \end{aligned}$$

$$\begin{aligned} D_{iso} \quad = \quad & \omega^3 + \omega^2 k^2 \nu \left(\frac{7}{3} + \zeta \right) + \omega \left(1 - 2kg + p_\sigma k^2 + k^4 \nu \left(\frac{4}{3}\nu + \zeta \right) \right) \\ & + \nu k^2 \left(3(1+\beta) - 2kg + k^2 p_\sigma \right) \end{aligned}$$

requires a number of parameters to be specified. Namely, the ground state of the model ring is characterized by the surface density Σ, the effective velocity dispersion c and the value for the Keplerian frequency Ω and the exponent β. The effective velocity dispersion is defined via the total pressure (un–scaled) as

$$p = c^2 \Sigma \tag{4.7}$$

so that the dimensionless total pressure is unity in the adopted scaling. In the remainder of this chapter all the quantities are un–scaled, unless explicitly stated.

For the ground state knowledge is required for the transport coefficients ν, ζ, and κ. Further, one needs to know about the derivatives with respect to temperature and surface density of p, ν, and Γ, taken at the ground state.

4.3.1 Evaluation of the Transport Coefficients

The transport coefficients are determined from simulations (Salo et al., 2000b) by tabulating the fluxes of momentum ($\widehat{P}$) and energy ($\vec{q}$). In the hydrodynamic equations these are related linearly to the gradients of the state variables via the transport coefficients in the constitutive relations

$$\begin{aligned} p\,\delta_{\alpha\beta} - 2\eta D_{\alpha\beta} - \xi \delta_{\alpha\beta} \nabla_\gamma u_\gamma \quad &= \quad \widehat{P}_{\alpha\beta} \\ -\kappa \nabla_\alpha T \quad &= \quad q_\alpha \,. \end{aligned} \tag{4.8}$$

Thus, the transport coefficients can be constructed from the fluxes and the gradients for a given situation.

For a proper determination of the transport coefficients in the simulations it must be ensured that these simulations do not develop overstable oscillations. This is most easily done by choosing the dimensions of the simulation box small enough, so that they are below the minimal wavelength of overstability.

The fluxes have local and nonlocal (collisional) contributions as mentioned in chapter 2.2 where the nonlocal viscosity was found to be important for the modeling of the vertical structure of the rings. In appendix A both contributions to the fluxes are motivated in terms of kinetic theory and in appendix B examples are given for transport coefficients for granular material.

The local contribution is the direct transport of momentum or energy in the particles' motion, the familiar kind of transport in gas– and hydrodynamics. This is drawn schemat-

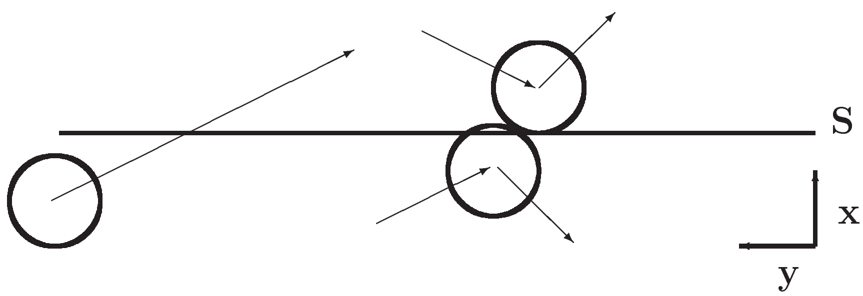

Figure 4.4: *Transport through the surface S in a particles' motion (left) and over the particle diameter in a collision (right).*

ically in fig (4.4, left). Let the local mean flow velocity $\vec{u} = \langle\vec{v}\rangle$ be different above and below the imagined interface S and let $\vec{a} = \vec{v} - \vec{u}$ be the deviation of the particles' velocity from the local mean velocity. Then particles that cross S between two collisions will on the average transfer momentum and energy between the two regions. These momentum and energy fluxes are

$$\begin{aligned} \widehat{P}^{local}_{\alpha\beta} &= \sigma\langle a_\alpha a_\beta\rangle \\ q^{local}_\alpha &= \frac{\sigma}{2}\langle a^2 a_\alpha\rangle\,. \end{aligned} \tag{4.9}$$

The nonlocal contribution to the fluxes, referring to momentum and energy transfered *in* a collision over a particles' diameter, drawn schematically in fig (4.4, right). The corresponding fluxes are (Wisdom & Tremaine, 1988)

$$\begin{aligned} \widehat{P}^{nonlocal}_{\alpha\beta} &= \frac{\sigma}{N\Delta t}\sum_{impacts}\Delta x_\alpha \Delta a_\beta \\ q^{nonlocal}_\alpha &= \frac{1}{2}\frac{\sigma}{N\Delta t}\sum_{impacts}\Delta x_\alpha \Delta a_t^2\,, \end{aligned} \tag{4.10}$$

where $\Delta\vec{x}$ is the distance of the particle centers at the moment of impact, $\Delta\vec{a}$ is the velocity change of the particle with the larger αth coordinate. Δa_t^2 refers to the transported energy in the impact, which has to be separated from the dissipated energy, as will be described in more detail below. The sum extends over all impacts taking place in the system (or in the local region of interest) in the time interval Δt and N is the total number of particles.

Shear viscosity, pressure, and temperature

In the unperturbed steady state of the simulations the mean velocity is $\vec{U} = -\frac{3}{2}\Omega\, x\vec{e}_y$ in the coordinate frame centered in the middle of the simulation box, the x–axis pointing radially outward, the y–axis in direction of the orbital motion. This implies with eq (4.9) the definition of the local and nonlocal dynamic shear viscosities

$$\widehat{P}_{xy}^{local} = \eta^{local}\frac{3}{2}\Omega\,, \quad \widehat{P}_{xy}^{nonlocal} = \eta^{nonlocal}\frac{3}{2}\Omega\,. \tag{4.11}$$

The local and nonlocal parts of the dynamic viscosity η can thus be determined from the tabulated particle positions and velocities of a simulation with the momentum flux terms eq (4.9) or eq (4.10), respectively. It is possible to achieve a high accuracy for the value of η, since in the steady state the averages can be taken over all particles in the system, and also over an arbitrarily long time.

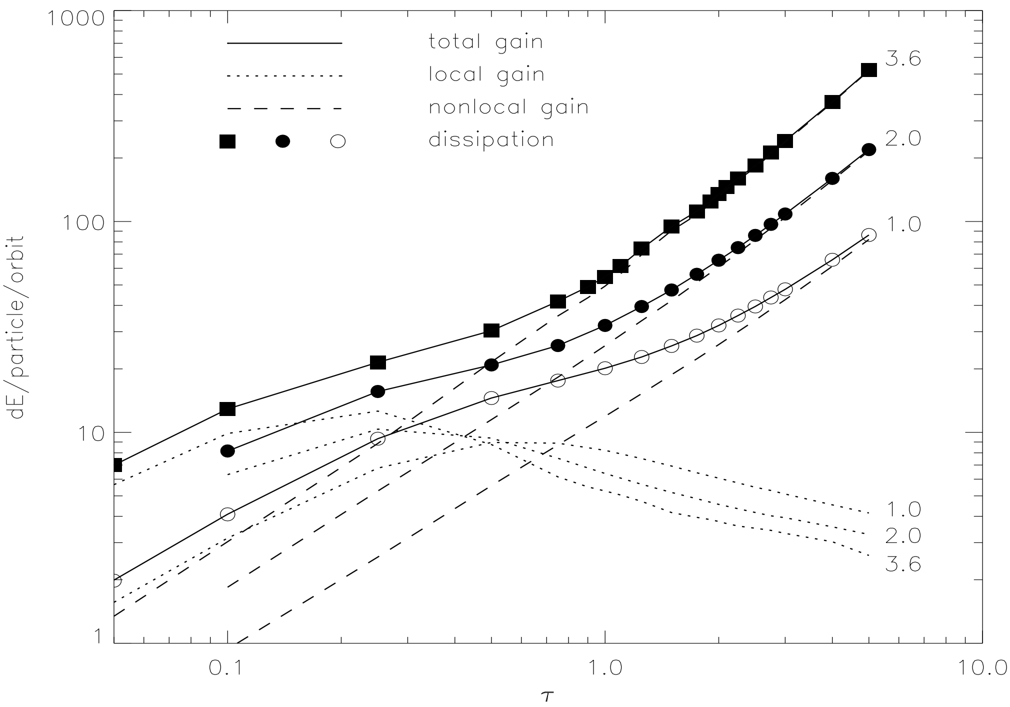

Figure 4.5: *Check of the measurements of the shear viscosity and the dissipation rate. The total energy gain rate is shown vs optical depth as a solid line for different factors of enhancement of vertical oscillations Ω_z/Ω. The symbols mark the dissipation rate. The energy unit is $(R_p\Omega)^2$.*

Taking the trace of eq (4.8) provides in a similar manner a method to determine the local and nonlocal components of the isotropic pressure p from the simulations. Also, summing up directly the energy dissipation in individual impacts, the energy dissipation rate Γ is determined.

A check for the values of the shear viscosity and the cooling function Γ is the energy balance of the simulated system which should fulfill eq (3.1). In fig (4.5) the energy gain and loss per particle and per orbital revolution is shown for simulations with different enhancement factors Ω_z/Ω of the frequency of vertical oscillations. The total (local plus nonlocal) gain rates are the solid lines and the dissipation rates are the symbols. The relation (3.1) is accurately fulfilled.

Bulk viscosity

The bulk viscosity can not be measured from the steady state in the simulations, since the effect of bulk viscosity enters through a compression, while the ground state velocity profile is free of divergences. Thus, a small perturbation is added to the steady state velocities of the form

$$\Delta u(x) = A_u \cos\left(\frac{2\pi x}{L_x}\right) \tag{4.12}$$

causing a non–vanishing divergence in the velocity with a decaying amplitude A_u. L_x is the radial box length. Taking the trace of eq (4.8) now yields

$$p(\vec{\nabla}\cdot\vec{u}) = p(\vec{\nabla}\cdot\vec{u} = 0) - \xi\vec{\nabla}\cdot\vec{u}\,. \tag{4.13}$$

The pressure p deviates from the pressure in a system with the same density and velocity dispersion but vanishing compression by the last term which is proportional to the bulk viscosity. This provides a method to determine ξ. Practically, the instantaneous pressure $p(\vec{\nabla}\cdot\vec{u})$ is obtained in small radial bins again from the tabulated particle positions and velocities employing relations (4.9), and (4.10). Similarly, the instantaneous compression $\vec{\nabla}\cdot\vec{u}$ is determined in each radial bin. The value for the compression-less pressure $p(\vec{\nabla}\cdot\vec{u} = 0)$ is taken from the steady state simulations that have been used for the measurement of the shear viscosity, intermediate values are interpolated with a second degree polynomial.

The radial profiles of the local and nonlocal parts of the pressures $p(\vec{\nabla}\cdot\vec{u})$ and $p(\vec{\nabla}\cdot\vec{u} = 0)$ and their difference is shown in fig (4.6) for one time step of the relaxation of the superimposed compression wave. The simulation experiment is repeated several times. When the pressure difference is plotted against the compression for all radial bins and time steps, a linear fit yields the value of the bulk viscosity.

It has been checked that the so obtained bulk viscosity is independent of the initial amplitude of the velocity perturbation A_u. For the measurement of plot (4.6) an amplitude $A_u = 2R_p\Omega$ was chosen. This is a relatively large perturbation, comparable in size to the radial velocity dispersion. Still, the perturbation leads to an enhancement of the mean temperature in the simulation box of only 2%. A smaller amplitude $A_u = R_p\Omega$ yields practically the same results within 3% accuracy.

Heat conductivity

To evaluate the heat conductivity a temperature gradient must be present in the system. This is achieved by superimposing a temperature perturbation to the simulations, determining the heat conductivity from the instantaneous fluxes and gradients of temperature in appropriately chosen spatial bins. Instead of applying an initial perturbation of the particle random velocities that decays in time, a slight modification of the elastic properties of the particles is imposed of the form

$$v_c(x) = v_B\left[1 + A_B\cos\left(\frac{2\pi x}{L_x}\right)\right] \tag{4.14}$$

where v_c now replaces the characteristic velocity in the Bridges et al. (1984) collision law [eq (4.5)], so that

$$\epsilon(x) = \left(\frac{\vec{v}\cdot\vec{n}}{v_c(x)}\right)^{-0.234} \tag{4.15}$$

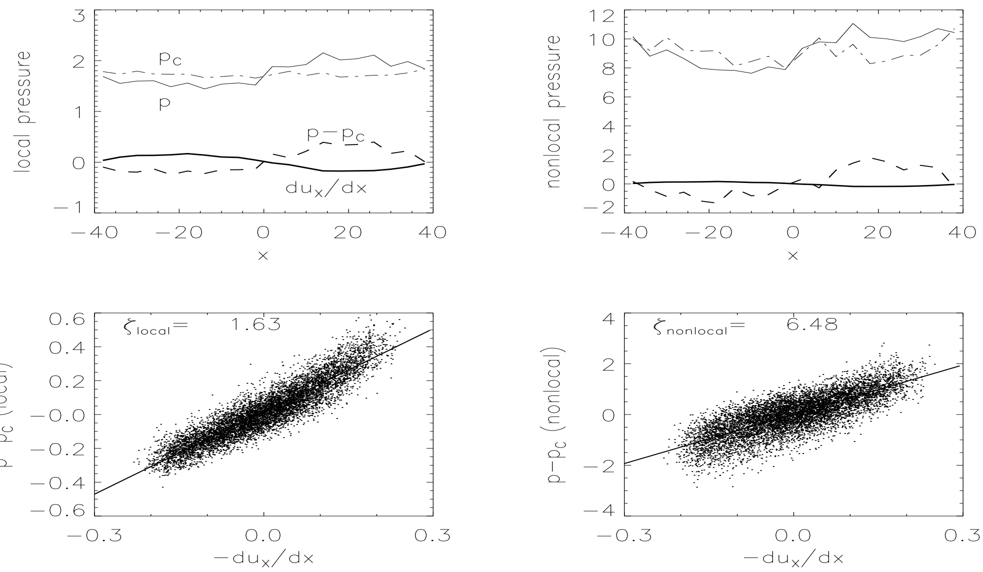

Figure 4.6: *Measurement of the bulk viscosity for an optical depth $\tau = 0.5$ and $\Omega_z/\Omega = 3.6$. The upper plots show the local and nonlocal parts of the pressure $p(\vec{\nabla}\cdot\vec{u})$ and $p(\vec{\nabla}\cdot\vec{u} = 0)$ (labeled by p_c in the plot) and the compression $\vec{\nabla}\cdot\vec{u} = \partial u/\partial x$ against the radial coordinate for a single time step. The lower plots show the pressure difference against the compression for all radial bins and all the recorded time steps. The slope of a linear fit yields the local and nonlocal part of the bulk viscosity.*

varies along the radial direction in the simulation box. Then a stationary radial temperature profile develops, allowing a more accurate determination of the heat conductivity than from a non–steady situation, since the obtained values can be averaged again over arbitrarily long times. The variations in the density profiles associated with those in the temperature remain tolerably small, as long as the amplitudes A_B are not too large. For the purpose of this measurement A_B was varied between 0.01 and 0.5, leading to values of κ that differed at most by 5%. The final measurements were carried out with an amplitude of $A_B = 0.2$.

Again, local and non–local contributions to the energy transport are determined. The nonlocal energy flux affords more care, since the energy transfered in a collision $\propto \Delta a_t^2$ has to be separated from the energy that has been dissipated. Let the non–systematic velocities of the colliding particles before the collision be denoted by $\vec{a}_1$ and $\vec{a}_2$. The center of mass velocity for particles of equal mass is

$$\vec{a}_c = \frac{1}{2}(\vec{a}_1 + \vec{a}_2) \tag{4.16}$$

and the relative velocity

$$\vec{g} = \vec{a}_2 - \vec{a}_1 \,. \tag{4.17}$$

The impact velocities expressed through relative and center of mass velocity are

$$\vec{a}_{1/2} = \vec{a}_c \mp \frac{1}{2}\vec{g} \tag{4.18}$$

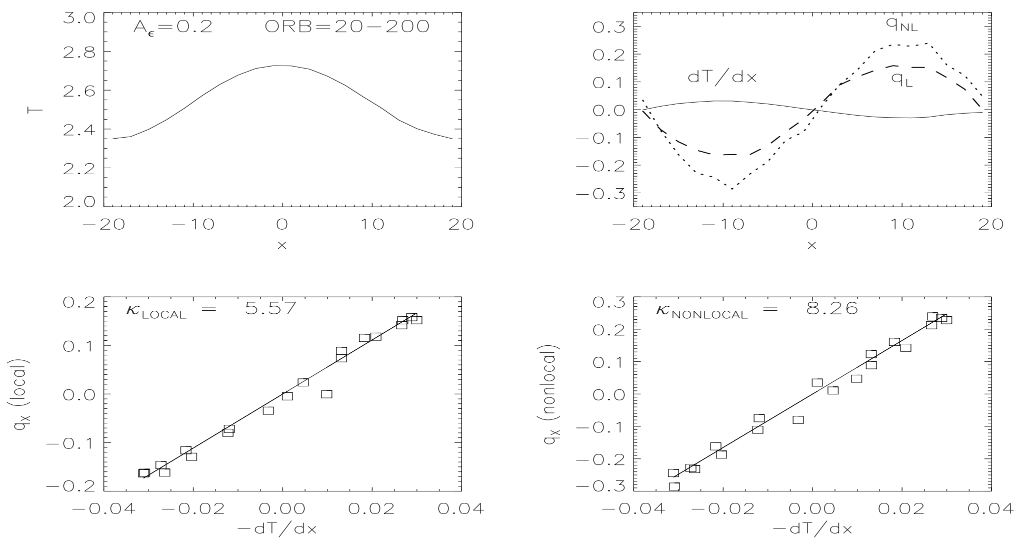

Figure 4.7: *Measurement of the heat conductivity. Upper plots: Steady state radial temperature profile, temperature gradient and local and nonlocal heat flux. Lower plots: Fluxes plotted vs the temperature gradient. Units of temperature, heat conductivity, and heat flow are $(R_p\Omega)^2$, $R_p^2\Omega$, and $(R_p\Omega)^3$, respectively.*

and the specific energies before the collision

$$E_{1/2} \equiv \frac{1}{2}\vec{a}_{1/2}^2 = \frac{1}{2}\left(\vec{a}_c^2 + \frac{1}{4}\vec{g}^2 \mp \vec{a}_c \cdot \vec{g}\right) \tag{4.19}$$

In the collision, for the smooth spherical particles considered here, only the relative velocity is changed by the dissipation in the impact as

$$\vec{g}' = \vec{g} - (1+\epsilon)(\vec{g}\cdot\vec{n})\,\vec{n} \tag{4.20}$$

where a prime denotes the values after the collision and $\vec{n}$ is the unit vector pointing from particle 1 to particle 2 at the moment of the collision. The collisional change of the kinetic energies of the particles participating the impact is then

$$\Delta E_{1/2} \equiv E'_{1/2} - E_{1/2} = \frac{\epsilon^2-1}{8}(\vec{g}\cdot\vec{n})^2 \mp \frac{1+\epsilon}{2}(\vec{g}\cdot\vec{n})(\vec{a}_c\cdot\vec{n})\,. \tag{4.21}$$

The first term on the right–hand–side is the energy (per particle) dissipated in the impact and the second one is the transfered energy. This transported energy defines the quantity Δa_t^2 needed for the evaluation of the nonlocal heat flux (4.10)

$$\frac{1}{2}\Delta a_t^2 \equiv \frac{1+\epsilon}{2}(\vec{g}\cdot\vec{n})(\vec{a}_c\cdot\vec{n})\,. \tag{4.22}$$

An example of a measurement of κ from a simulation is shown in fig (4.7). The radial profiles of temperature and local and nonlocal heat flux are averaged values over about 200 orbital periods. The dependence of the heat flow on the temperature gradient is approximately linear, a fit yields the coefficient of heat conductivity.

A check of the measurement is provided by the energy balance of the stationary state of these simulations with a radial temperature gradient. Perturbations in the linear shear profile have to be taken into account

$$\vec{u} = \begin{pmatrix} \delta u(x) \\ -\frac{3}{2}\Omega x + \delta v(x) \end{pmatrix} \tag{4.23}$$

The energy balance equation

$$\frac{3}{2}\sigma(\partial_t + \vec{u}\cdot\vec{\nabla})T = -\hat{P} : \vec{\nabla}\vec{u} - \vec{\nabla}\cdot\vec{q} - \Gamma \tag{4.24}$$

reduces not to the simple relation (3.1) in this case. The pressure contribution reads

$$\hat{P} : \vec{\nabla}\vec{u} = p\,\partial_x\delta u - \left(\frac{4}{3}\eta + \zeta\right)(\partial_x\delta u)^2 - \eta\left[-\frac{3}{2}\Omega + \partial_x\delta v\right]^2 \tag{4.25}$$

with the dynamic quantities η, ζ and the scalar pressure p. Thus, the radial energy balance is

$$\begin{aligned} &\frac{3}{2}\sigma\,\delta u\,\partial_x T = \\ &-p\,\partial_x\delta u + \left(\frac{4}{3}\eta + \zeta\right)(\partial_x\delta u)^2 + \eta\left[-\frac{3}{2}\Omega + \partial_x\delta v\right]^2 + \partial_x(\kappa_D\partial_x T) - \Gamma\,. \end{aligned} \tag{4.26}$$

In the simulations the perturbations in the radial velocity δu are negligibly small compared to those in the tangential velocity δv, the latter being itself a small correction to the linear shear profile. Neglecting the terms that contain δu the balance of viscous gain, heat flow, and collisional dissipation is

$$0 = \eta\left[-\frac{3}{2}\Omega + \partial_x\delta v\right]^2 + \partial_x(\kappa_D\partial_x T) - \Gamma\,. \tag{4.27}$$

The radial profiles of gain, flow, and loss rates (denoted as G_{sim}, H_{sim}, and Γ_{sim}) are shown in fig (4.8) for a simulation of optical depth $\tau = 0.5$. Taking into account the difference in scale of the upper and lower plot, it follows that the difference in energy production and dissipation is indeed very accurately balanced by the energy flow.

4.3.2 Ground State Temperature Derivatives

In the non–isothermal dispersion relation also the derivatives of the pressure p, kinematic viscosity ν, and collisional cooling Γ with respect to temperature, taken at the systems ground state, are required. They are determined again from the measurement of the instantaneous values of p, ν, and Γ for short time intervals in course of the relaxation of the system to the ground state temperature T_s after a uniform temperature perturbation. Practically, this perturbation is made by a multiplication of the random velocities of the particles by a constant factor f, resulting in an overall change in the temperatures by a factor f^2. The local simulation method is particularly convenient for the determination of the temperature derivatives in this manner, since the surface density is fixed *a priori*, and thus the temperature can be varied independently.

A basic difficulty in the determination of the temperature derivatives, are oscillations in the scale hight of the system during the relaxation to the steady state temperature. These oscillations are reflected in the collision frequency and the development of the mean temperature itself [see fig (4.9)]. A possible way to reduce the influence of the oscillations

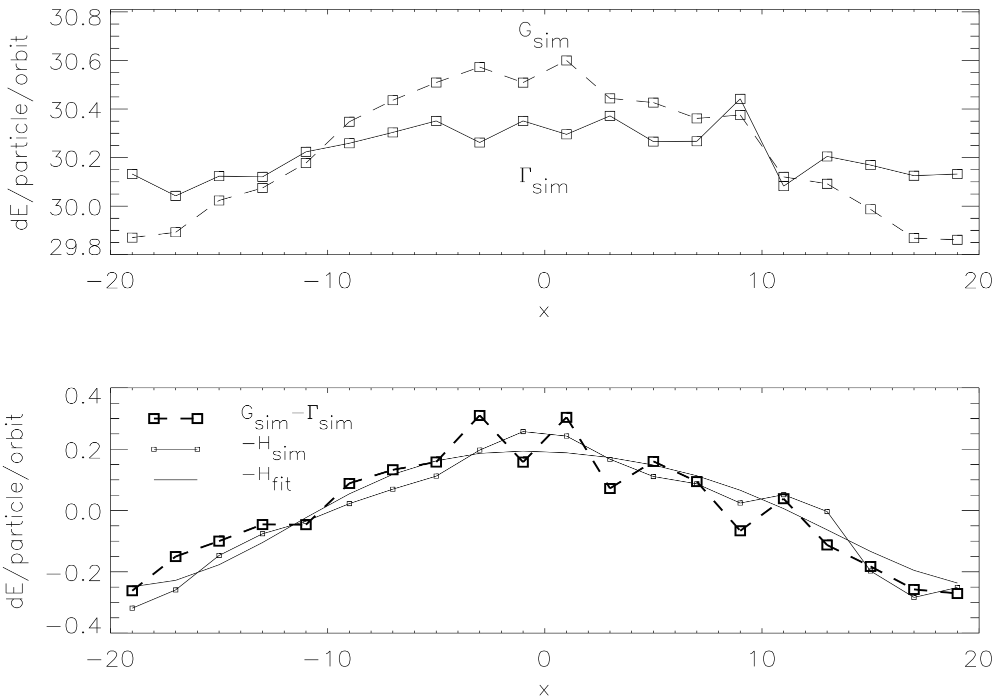

Figure 4.8: *Simulations ($\tau = 0.5$) with a steady state radial temperature profile used to determine the heat conductivity. Upper plot: Radial profiles of gain and loss rates. Lower plots: Difference of gain and loss compared to the heat flow. H_{sim} is the gradient of the heat flow vector [eq (4.9) and (4.10)] and in H_{fit} the measured value for κ is used. The units of energy are $(R_p\Omega)^2$.*

is to average over measurements with different f, since the oscillations differ slightly with altered f. For the final evaluation of the temperature derivatives a superposition of 11 runs is used with $f = 0.5 - 2.0$, as shown in fig (4.9) for a system with $\tau = 1$ and $\Omega_z/\Omega = 3.6$. Instead of the derivative of Γ the derivative

$$E_{\mathrm{T}} = \frac{\partial}{\partial T}\left(\frac{2}{3}\Gamma - \frac{3}{2}\Omega^2\eta\right) \tag{4.28}$$

is determined directly, since $\partial\Gamma/\partial T$ enters the dispersion relation of the non–isothermal model in this combination. The derivatives are determined by a linear fit of the measured values of p, ν, divided by their ground state values, and $\frac{2}{3}\Gamma - \frac{3}{2}\Omega^2\eta$ plotted against the deviation of the instantaneous temperature from the ground state temperature. For this fit the high temperature regime is excluded, since the *ground state* values of those derivatives are needed. Also the temperature regime too near the noise level of the ground state is excluded.

4.3.3 Ground State Density Derivatives

A similar method to determine the required derivatives with respect to the surface density, as was followed for the temperature derivatives, is very difficult to realize in in the local

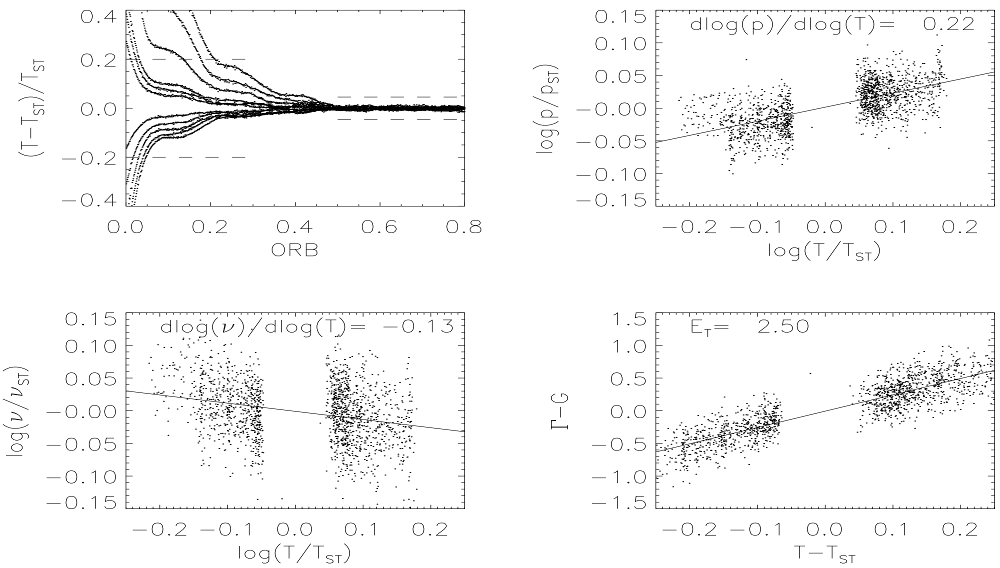

Figure 4.9: *Determination of the temperature derivatives of p, ν, and E_T from simulations with optical depth $\tau = 1$. In a steady state simulation the random velocities of the particles are multiplied by a factor f, resulting in a sudden change in the overall temperature. The temperature derivatives are derived from the development of the instantaneous values of p, ν, and $E_{loss} - E_{gain}$ in course of the relaxation to equilibrium.*

simulations. A sudden enhancement or decrease of Σ could in principle be obtained from a change in the box dimensions. However, this would affect immediately the temperature as well as the density, so that both effects could not be separated. The derivatives with respect to surface density are therefore approximated by the variation of the ground state quantities from simulations with different ground state density. This approximation should give a good result since in the regime of optical depths of interest here the ground state temperature varies very weakly with the density, a consequence of the fact that the temperature has a minimum around $\tau = 1$ ($\Omega_z/\Omega = 3.6$), see fig (4.10).

4.3.4 Results

The methods described in the last section for the determination of various quantities needed as parameters in the dispersion relation are applied to simulations of different optical depth and different enhancement factors for the frequency of vertical oscillations $\Omega_z/\Omega = 1.0, 2.0, 3.6$ (Salo et al., 2000b). The simulations employ uni–sized particles of radius $R_p = 1\,\mathrm{m}$ and Bridges et al. (1984) elasticity law.

It is remarkable that the variation of Ω_z changes the transport properties, as well as the pressure, and the derivatives with respect to temperature and density, basically through the collision frequency of the system. This becomes clear when the results are plotted against the collision frequency at given optical depth, rather than the optical depth itself. In fig (4.10) the dependence of the ground state temperature, the kinematic pressure, and the kinematic viscosity on the optical depth is shown. The curves for $\Omega_z/\Omega = 1.0$ and 3.6 nearly coincide when pressure and viscosity are plotted against the collision frequency. The ground state

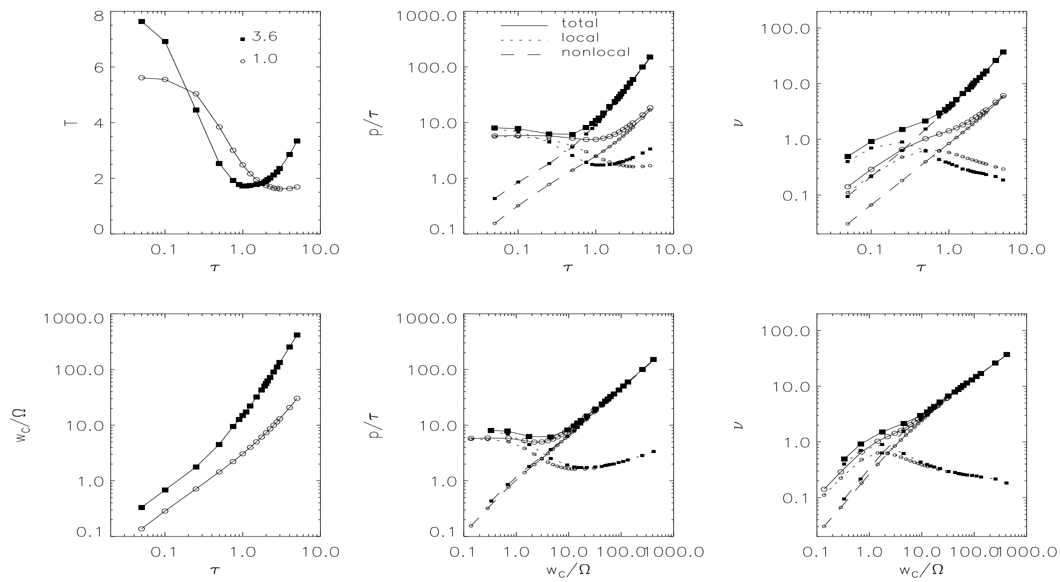

Figure 4.10: *Dependence of various quantities on the optical depth for* $\Omega_z/\Omega = 1.0$ *and* 3.6. *Upper row: Ground state temperature, kinematic pressure, and kinematic shear viscosity. Lower row: Dependence of the collision frequency on the optical depth. The curves for* $\Omega_z/\Omega = 1.0$ *and* 3.6 *of the kinematic pressure and the kinematic shear viscosity nearly coincide when plotted against the collision frequency rather than the optical depth.*

temperature first decreases with increased τ and starts to increase again for still larger τ. The decrease in T can be attributed to the influence of the particle volume, growing with optical depth and reducing the mean free path, and thus, the local viscosity. Simultaneously, the collision frequency rises, and thus the collisional energy loss. If the optical depth is further increased, the nonlocal viscosity becomes dominant and the steady state temperature rises again. The nonlocal contributions to the kinematic pressure and shear viscosity exceed the local ones for $\omega_c/\Omega \approx 2.5$, which corresponds to about 15 collisions per particle and orbital revolution.

Fig (4.11) shows the variation of the kinematic transport coefficients with the optical depth. For optical depths larger than about $\tau = 0.5$ the nonlocal contributions dominate ($\Omega_z/\Omega = 3.6$). For local and nonlocal, as well as total values, the magnitudes relate as $\kappa > \zeta > \nu$. The ratios κ/ν and ζ/ν decrease with increasing optical depth and approach constant values for high densities, namely $\kappa/\nu \to 4$ and $\zeta/\nu \to 2$. This is remarkably close to the ratios obtained from kinetic theory for hard sphere gases (Chapman & Cowling, 1970) and slightly inelastic hard sphere gases (Jenkins & Richman, 1985), [see fig (3.1)]. The deviations at low τ are to be expected since here the hydrodynamic regime is left.

The derivatives with respect to temperature are displayed in fig (4.12). Both, pressure and shear viscosity depend nearly linearly on the temperature for low optical depth, as was to be expected, since then the local contributions are dominant [the kinematic shear viscosity is then in good approximation given by eq (2.14)]. With increasing optical depth the logarithmic derivatives of both quantities with respect to temperature decrease to zero. This implies that the nonlocal pressure and shear viscosity, dominant at large optical depth, are nearly independent of the velocity dispersion. The quantity E_{T} is always positive, indicating

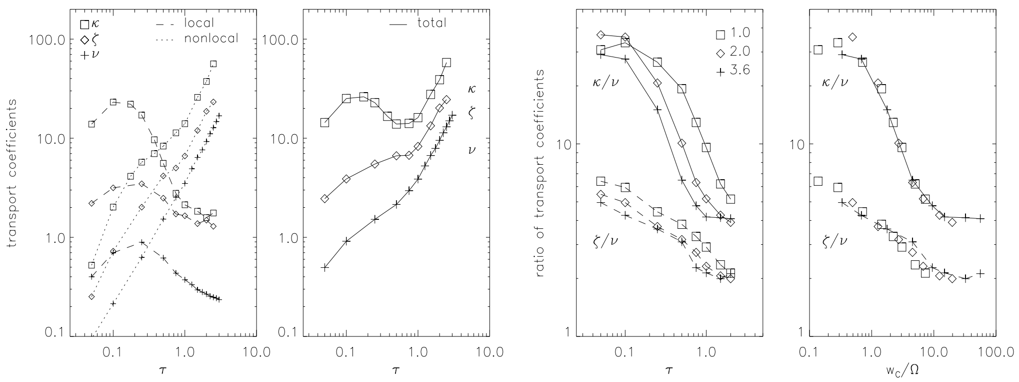

Figure 4.11: *Left frames: Kinematic transport coefficients for various optical depths for simulations with $\Omega_z/\Omega = 3.6$. Right frames: Ratios κ/ν and ζ/ν for different enhancement of vertical frequencies plotted vs optical depth. When plotted against the collision frequency the different cases fall on top of each other.*

thermal stability of the system [see eq 3.17 and the subsequent discussion].

The dependency of the quantities of interest on the optical depth is inferred from the density variation of their ground state values. This should be a good approximation, since the ground state temperature only varies weakly for the optical depths investigated here [see first plot in fig (4.10)]. This relates the derivative of the cooling function directly to the derivative of the shear viscosity, since viscous gain and collisional cooling balance at the ground state, i.e. $\partial \log \Gamma / \partial \log \tau = \partial \log \nu / \partial \log \tau + 1$. In the low optical depth regime the pressure and the kinematic shear viscosity are both proportional to τ, since again the local contribution dominates [fig (4.13)]. The logarithmic derivative $\beta = \partial \log \nu / \partial \log \tau$ first decreases with increasing optical depth to about 0.5 and then increases when the nonlocal part becomes dominant. β is unity for a collision frequency of $\omega_c/\Omega \approx 10$ for all the ratios Ω_z/Ω, or about 60 collisions per particle and orbit.

The parameters needed in the non–isothermal dispersion relation obtained from simulations are displayed in table (4.1) for the case of a vertical frequency enhancement factor of $\Omega_z/\Omega = 3.6$ and for the optical depths $\tau = 0.5, 1, 1.5, 2$. All the quantities given in that

Ground state parameters

τ	c[cm/s]	ν	ζ/ν	κ/ν	p^{local}	p_σ	p_{T}	E_{T}	η_{T}	Γ_σ	β
0.5	0.048	0.348	3.10	6.48	0.411	1.79	1.28	0.72	-0.031	1.34	0.67
1	0.064	0.357	2.14	4.17	0.160	2.19	1.35	2.50	-0.280	1.74	1.15
1.5	0.086	0.342	1.99	4.14	0.091	2.41	1.68	3.78	-0.363	1.67	1.19
2	0.106	0.322	2.12	4.09	0.064	2.72	2.72	4.51	0.378	1.84	1.55

Table 4.1: *Ground state parameters obtained from simulations with a enhancement of the vertical frequency of oscillations $\Omega_z/\Omega = 3.6$.*

table are dimensionless, excluding the effective velocity dispersion c. Time is scaled with the Keplerian frequency, the numerical value used is $\Omega = 1.948 \times 10^{-4}\mathrm{s}^{-1}$, the value for a semimajor axis of 100 000 km in the Saturnian system. Length is scaled with c/Ω, velocity

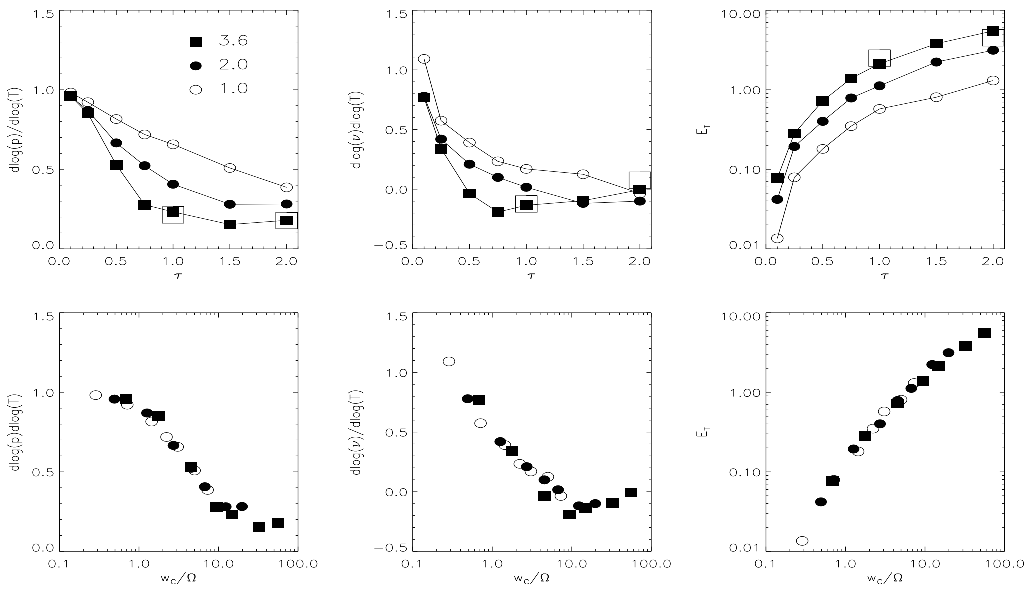

Figure 4.12: *Temperature derivatives from simulations vs optical depth (upper row) and collision frequency. Again, the differences for altered Ω_z/Ω are mainly due to the altered collision frequency.*

with c, and density with the ground state density Σ. Thus, the total ground state pressure is unity and the ground state temperature T_0 is equal to p^{local} in this scaling. The numerical value of the ground state density does not alter the analysis in the non-self–gravitating case, or, if the effect of self-gravity in the simulations is taken into account by an enhancement of the vertical frequency.

4.3.5 Summary

The parameters needed for the linear stability analysis of the nonisothermal hydrodynanic model presented in chapter 3 are determined in local molecular dynamics simulations of a dense planetary ring. The simulations employ

- a Saturnian distance of $100,000\,\mathrm{km}$
- uni–sized ($R_p = 1\,\mathrm{m}$) spherical frictionless particles
- the velocity dependent elasticity law determined experimentally by Bridges et al. (1984)
- self–gravity approximated by an enhacement of the frequency of vertical oscillations $\Omega_z/\Omega = 1, 2, 3.6$
- optical depths $\tau = 0.5, 1, 1.5, 2.$

Results are shown in table 4.1 for $\Omega_z/\Omega = 3.6$ in dimensionless units. General properties are

- the **transports are mainly determined by the collision frequency.**

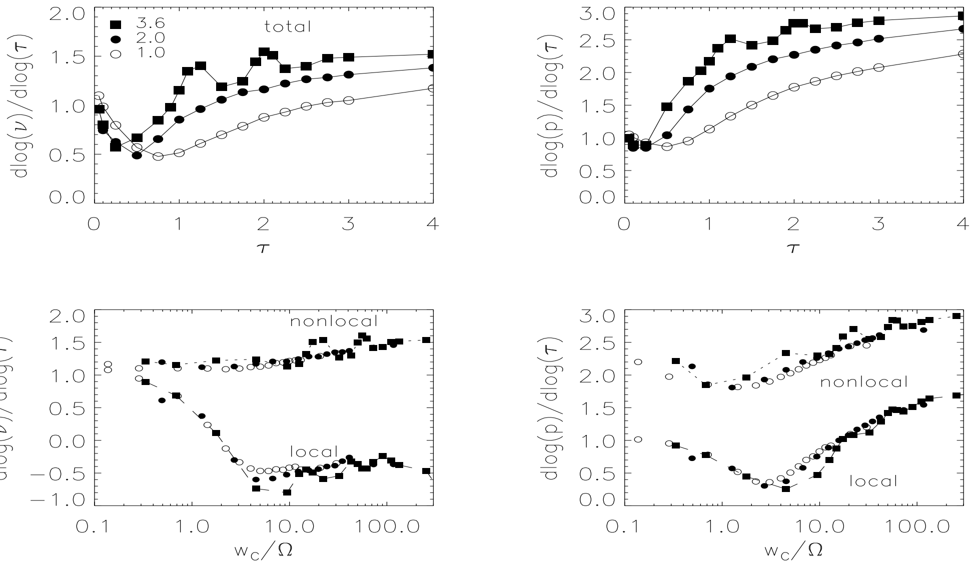

Figure 4.13: *Derivatives with respect to surface density vs optical depth (upper frames) and collision frequency (lower frames).*

- the **nonlocal part of the transports and the pressure dominates the local part in dense rings** of optical depth $\tau = 1$ and higher. Both contributions are comparable at $\tau \approx 0.5$, corresponding to about 20 to 30 collisions per orbit and particle.
- for large optical depth ($\tau > 2$) the **bulk viscosity exceeds the shear viscosity by a factor of two**. Similarly, the **ratio of heat conductivity and shear viscosity is about four**. This is close to values obtained from kinetic theory of inelastic hard sphere gases [see fig (3.1)].

Chapter 5

Comparison of Theory and Simulation

In this section the results of the hydrodynamic model are compared to 3D local N-particle simulations for meter sized particles for high optical depth ($\tau = 1$, $\tau = 2$). The simulation box is located at a distance of $100,000\,\mathrm{km}$ of a point mass of one Saturnian mass. For the inelasticity of the particles the standard formula of Bridges et al. (1984) is taken for an impact velocity dependent coefficient of restitution.

As already mentioned in section (3.1.2), the nonlinear non-axisymmetric gravitational wakes are not covered by the analysis of chapter 3. Consequently, the attention is restricted on simulational systems that consider self–gravity via the enhancement of the vertical frequency, leading to purely radial structure. Also, in this case the system has a stationary ground state, from which transport coefficients and other parameters needed for a comparison to the hydrodynamic model can be obtained, as is described in section 4.3. An inclusion of direct particle-particle self-gravity, and thus the presence of gravitational wakes will at least alter the ground state of the system. However, the growth of radial overstable modes is retained [see fig (4.2)].

Section 5.1 gives a quantitative comparison of the growth rates and oscillation frequencies predicted by the theory and those observed in simulations. In section 5.2 amplitude ratios and phase differences of the eigenfunctions of the isothermal hydrodynamic model are compared to simulational results.

5.1 Growth Rates and Oscillation Frequencies

In chapter 3.1 the non–isothermal model has been investigated for linear stability, resulting in a dispersion relation [eq (3.14)] conecting the complex frequency ω and the real radial wavenumber k. The real parts of the pair of complex conjugate roots of this dispersion relation correspond to the growth rate of viscous overstability, their imaginary parts to the oscillation frequency. Both quantities can be compared to simulations.

Growth Rates

In simulations that start from a stationary state the formation of oscillating radial perturbations is observed in the mean surface density, as well as in the non systematic radial and tangential velocities, and in the velocity dispersion [fig (4.3)]. The development of the Fourier modes of these perturbations is followed, and tabulated 40 times per orbital period.

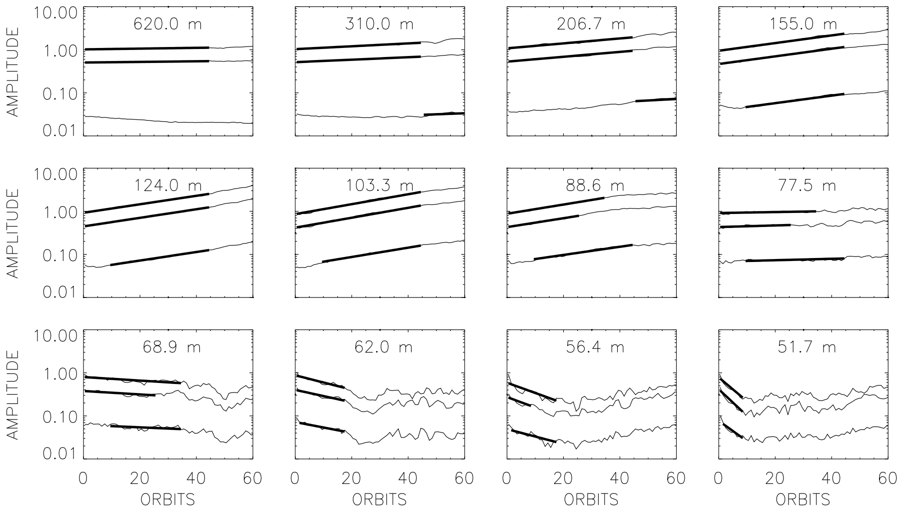

Figure 5.1: *Example for the determination of growth rates from a simulation with optical depth $\tau = 1$. The amplitudes of the Fourier modes of overstable oscillations in the optical depth (lower curve), and the radial (upper curve) and tangential velocity are tabulated 40 times per orbital revolution. Linear fits yield the growth and decay rates for the different modes. The unit of the velocity amplitudes is ΩR_p.*

An initial exponenential growth with characteristic times of a few tens of orbital revolutions is observed, depending on wavelength and optical depth of the run. To facilitate the determination of the growth rates a small initial seed is superimposed to the stationary state in form of low amplitude harmonic perturbations in solely the radial velocity of the simulational system. An example for the measurement from a simulation with optical depth $\tau = 1$ is shown in fig (5.1) in logarithmic scale. Linear fits yield the growth and decay rates in density and radial and tangential velocity for the different wavelengths. The amplitude in the density perturbation of longer wavelengths may decay initially before the overstable growth sets in, but then the growth rates in all the three state variables are practically the same. The growth rate is positive for all wavelengths larger than a critical wavelength (in the example with $\tau = 1$ about 80 m) and is maximal for an intermediate wavelength (100 m for $\tau = 1$). For modes that are shorter than the critical wavelength the decay rates of the initial seed perturbation are determined which can also be compared to the model predictions. The growing longer modes soon start to excite shorter modes and so the short perturbations start to grow again. This is a nonlinear effect that already sets in shortly after the beginning of the overstable growth.

In the model the growth rates are determined by computing numerically the roots of eq (3.14) with the parameters obtained in simulations (table 4.1). The growth rates corresponding to overstability are the real parts of the two conjugate complex solutions. Results are shown in fig (5.2) (upper plots). Ten folding times are related to the real parts of the growtn rates by eq (3.26). Basically, all perturbations with wavelength larger than roughly 100 m are found to be overstable for the dense model rings under consideration [particle radius 1 m elasticity of Bridges et al. (1984)], with fastest growth at a somewhat larger

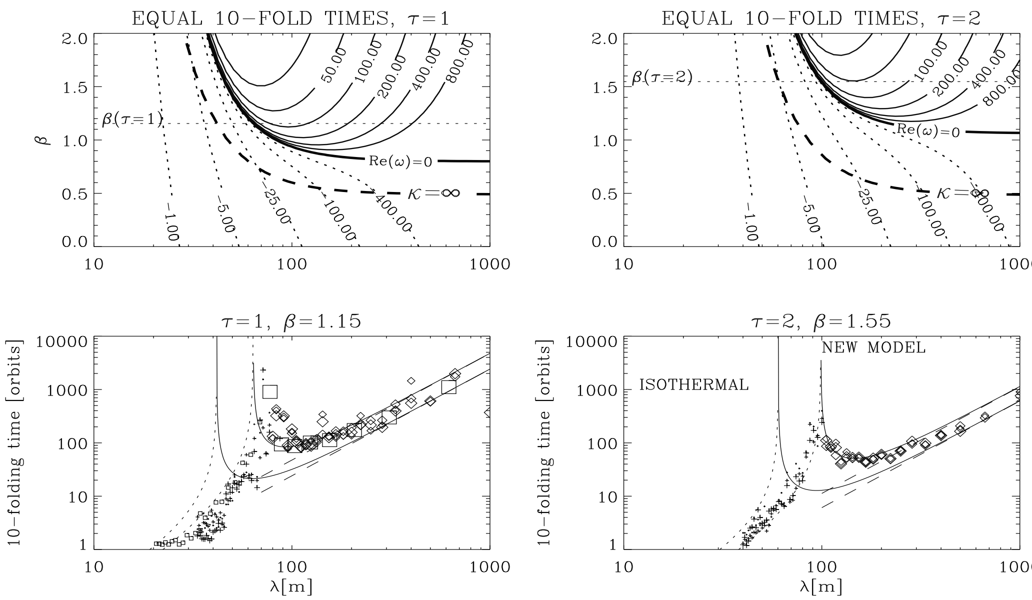

Figure 5.2: *Upper two plots: Lines of equal 10-folding times [eq (3.26)] of radial oscillations in units of orbital revolutions in the (λ, β)-plane, for $\tau = 1$ on the left and for $\tau = 2$ on the right. Solid lines correspond to growth times of the model including the energy balance, dotted lines to decay times of stable wavelengths. In both cases parameter values obtained in simulations have been used (table 4.1). The horizontal lines indicate the value of β that is relevant for the respective optical depth. The non–isothermality is found to moderate the overstability. For comparison the line of marginal stability of the isothermal model is also plotted (thick dashed line). Lower plots: 10-folding times from simulations where rise times of unstable wavelengths are plotted as diamond symbols and decay times of stable wavelengths as crosses. Different symbol sizes correspond to separately determined 10-folding times of perturbations in density (largest), radial velocity, and shear corrected tangential velocity (smallest). The theoretical rise and decay times, evaluated at the value of β marked with the horizontal line in the upper plots, are drawn as solid and dotted lines, respectively.*

wavelength. The growth rates decrease if the wavelength is further increased, finally going to zero for perturbations of a large spatial extension. The main effect of the inclusion of the energy balance is a stabilizing one as already indicated by the more qualitative analysis in Spahn et al. (2000). For comparison the marginal curve (labeled by $\kappa = \infty$) is also shown in fig (5.2). The stabilizing influence of a larger bulk viscosity $\zeta > \nu$ (as well as nonlocal pressure) is contained in that limit, in contrast to the similar plot in Schmit & Tscharnuter (1995), where $\zeta = \nu$ was assumed which would shift marginal stability to still smaller values of β [see eq (3.21)].

In fig (5.2) (lower plots) 10-folding times are shown for the hydrodynamic model as solid lines and for simulations as diamond symbols. The agreement between simulation and theory is significantly improved when the energy balance equation is considered in the analysis. In particular, in simulations without vertical frequency enhancement no overstability is observed for $\tau < 4$, in accordance with the non–isothermal model. The isothermal model on the other hand still predicts overstability for the system. The diamond symbols in fig (5.2) are the growth times obtained from simulations with a radial extension of the simulation box of 2000 m. For $\tau = 1$ growth times from a simulation with reduced radial box–length (620 m) are also shown as square symbols. The growth times are also practically independent of the tangential width of the box except for a slight delay of the onset of the overstable growth in a tangentially larger system. The dashed lines are the long–wavelength approximate solutions (3.18) for the overstable roots of the dispersion relation (3.14).

The influence of various parameters on the marginal curve of the oscillatory instability is displayed in fig (5.3) for an example with $\tau = 2$. Interestingly, the ten–folding times of overstable modes suffer a similar shift in the (λ, β) plane when parameters are varied. An important parameter, already present in the isothermal model, is the bulk viscosity ζ. In many studies that based on hydrodynamic models it was assumed that bulk viscosity is equal to shear viscosity. In the simulational systems investigated in section 4.3, it is found to be about double the shear viscosity, a change that stabilizes the system considerably. Other parameters introduced with the energy balance that may have a large influence on the growth times are p_{T}, η_{T}, and Γ_σ. The ratio of heat conductivity to shear viscosity in the simulations is about 4 for the optical depths that have been investigated. The stability behavior of the hydrodynamic model is insensitive to moderate variations of that parameter, while the effect of the thermal equation itself is large, as can be seen from the shift in the marginal stability line for $\kappa \to \infty$, corresponding to an isothermal model. This large influence can rather be attributed to the relaxation of thermal excitations to a balance of collisional cooling and viscous heating, which is neglected in an isothermal system. The time-scale of this relaxation is given by E_{T}^{-1} [see eq (3.4,3.17)].

Oscillation Frequencies

The frequencies of the overstable oscillations for different wavelengths are shown in fig (5.4) as a contour plot from a simulation with $\tau = 2$. The solid line is the imaginary part of the conjugate complex solutions of the dispersion relation eq (3.14), and the dashed line is the imaginary part of the small k expansion (3.18), which both do not deviate very much from eq (3.44). In this case where the self–gravity is approximated by $\Omega_z/\Omega = 3.6$ the frequency is always larger than the Keplerian frequency. In a system with true particle–particle gravity the wavelength dependence of the frequency is qualitatively covered by eq (3.44). Ignoring the small ($\propto k^4$) viscosity term, this means that all wavelengths smaller than the Jeans–length

$$\lambda_J = \pi \frac{p_\sigma}{g} \tag{5.1}$$

oscillate faster than the Keplerian frequency, and those larger than λ_J oscillate more slowly. The oscillation frequency for a simulation with true particle–particle gravity is shown in fig (5.5).

5.2 Eigenfunctions

In section (3.3) eigensolutions have been obtained for a simple isothermal hydrodynamic model of the ring's flow. These solutions were computed at the critical value of the parameter β [see eq (3.53)], from the eigenvectors of the linear problem that correspond to the overstable eigenvalues [eq (3.58) and (3.59)]. Other eigensolutions decay rapidly with characteristic time that is given to leading order in k by the eigenvalue $\omega^{(4)}$ in eq (3.22).

In spite of the simplifications made in the derivation of that solution qualitative agreements with the overstable modes in the simulations can be observed. First, for $k << 1$ in

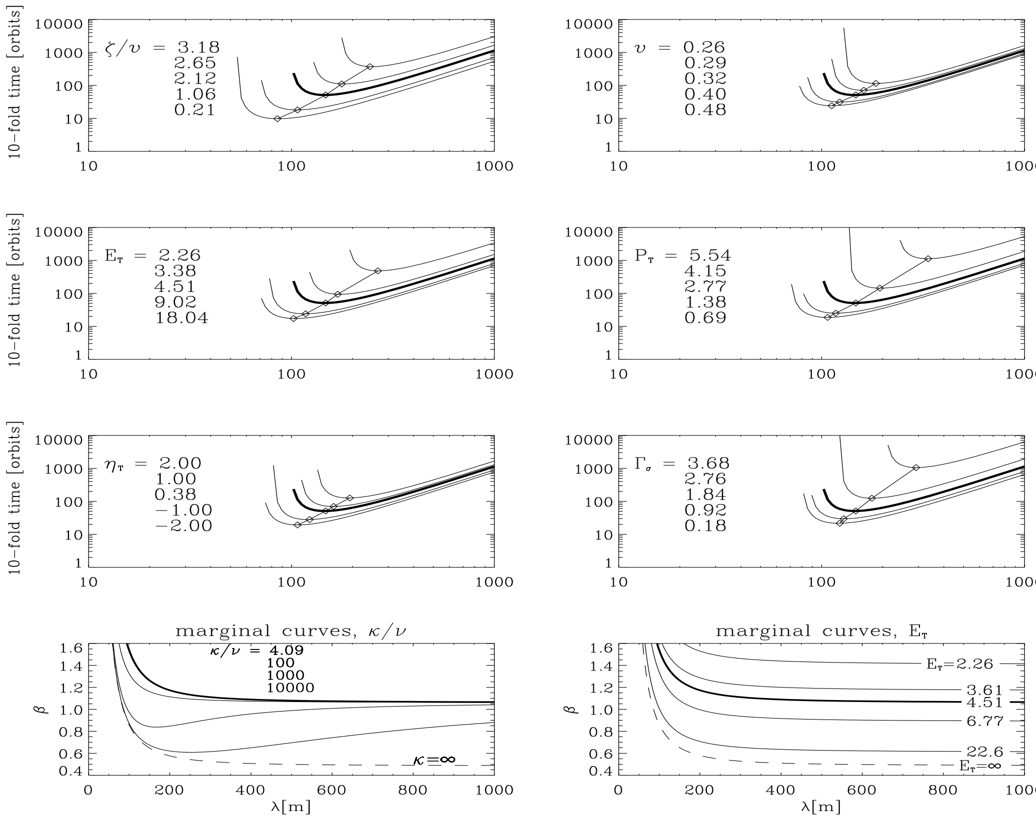

Figure 5.3: *The influence of parameters of the model on the ten folding times (upper six plots) and the marginal curves (lower two plots) of the non isothermal model for $\tau = 2$. The respective values as they are determined in simulations are represented with a thick line.*

the model the ratio of the oscillations of the radial velocity and the shear corrected tangential velocity is about 2, which is also observed approximately in the simulations, as can be seen in fig (4.3) and (5.9). This was also found in a numerical solution of the nonlinear isothermal hydrodynamic equations far from threshold $\beta = \beta_{cr}(k)$ performed by Schmit & Tscharnuter (1999). Second, for long wavelengths the ratio of the amplitudes of the velocity perturbations to the density amplitude should be proportional to λ [see eq (3.62)]. For a simulation this is shown in fig (5.6), where the linear dependence inferred from the theory is indeed observed. Third, the phase differences of the state variables obtained from simulations can be compared to those of the hydrodynamic eigensolutions for standing waves and traveling waves. In the linear regime both are equally good solutions. In those runs where the small initial seed (standing wave) perturbation has been superimposed on the radial velocities phase differences are observed in the early stage of the time development that are consistent with those of the hydrodynamic standing wave solution [eq (3.62)]. In fig (5.7) these are shown tabulated from a simulation for 50 orbital periods. The phases of the simulational system accumulate at the theoretically determined values for standing waves [table (3.1)]. From the initial seed perturbations in the radial velocity alone the system develops oscillations in all the state variables that keep the characteristic phase differences of the standing wave solution for more than 50 orbits. In the further time–evolution, with a

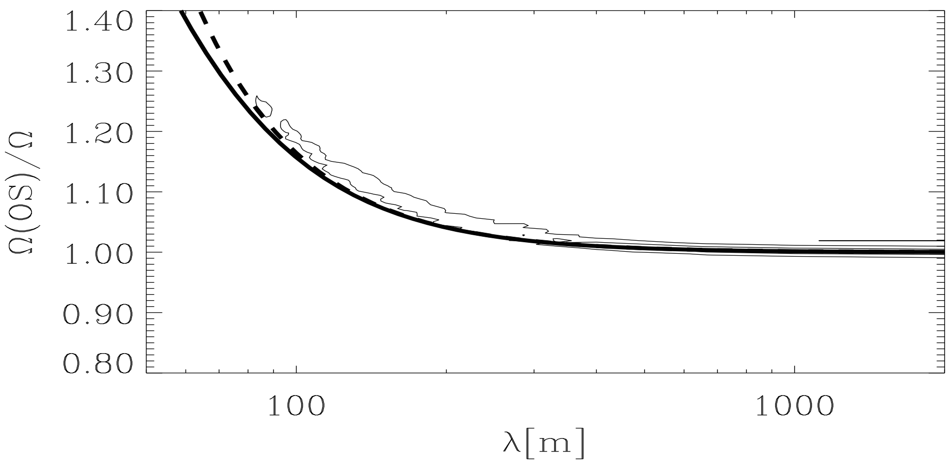

Figure 5.4: *The frequencies of the overstable oscillations from a simulation with optical depth $\tau = 2$ as a contour plot in the (ω, λ)–plane. The solid line is the theoretical curve from the numerical solution of the dispersion relation (3.14), and the dashed line the imaginary part of the approximation (3.18) for large wavelength.*

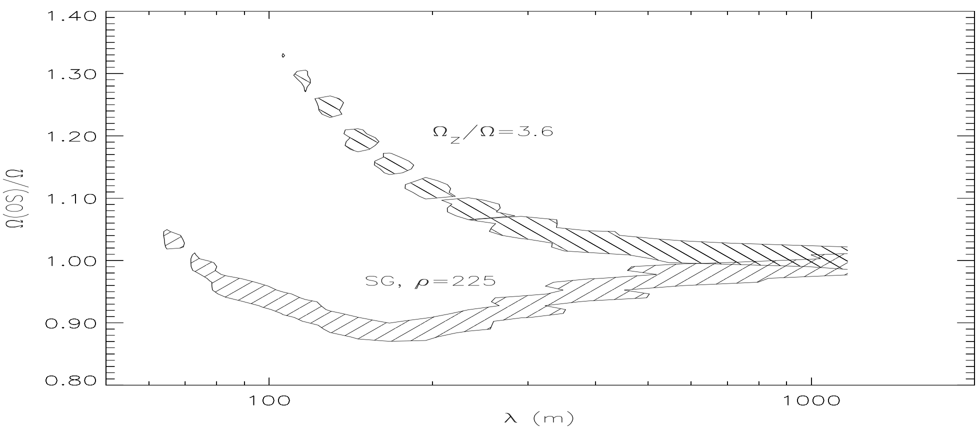

Figure 5.5: *The frequencies of the overstable oscillations from a simulation with optical depth $\tau = 1.4$ as a contour plot in the (ω, λ)–plane for a system with true particle–particle self–gravity and with enhancement of the frequency of vertical oscillations.*

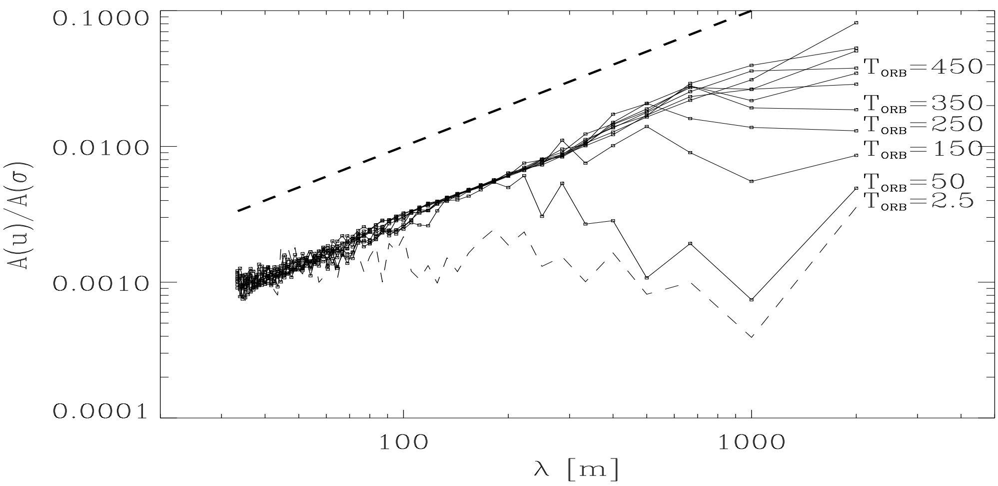

Figure 5.6: *The ratio of the amplitudes of radial velocity and surface density plotted against the wavelength for a simulation with optical depth* $\tau = 1.4$. *The different lines correspond to different times, starting with the dashed line. In course of the time development the ratio approaches the linear dependence on the wavelength (compare to thick dashed line) that is predicted by the hydrodynamic model for not too short wavelengths. The duration of the record in this plot was about 1000 orbital periods.*

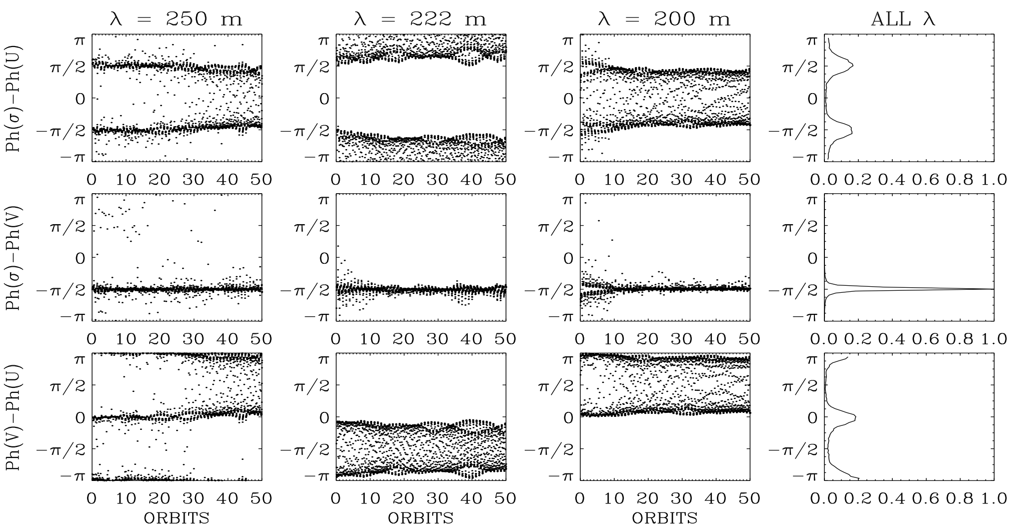

Figure 5.7: *The phase differences of the state variables* $\sigma, u,$ *and* v *for selected wavelengths are shown (first three columns). They are determined* 40 *times per orbital revolution from a simulation that covered* 50 *orbital periods. The last column shows the phase differences summed up over all wavelengths in a histogram with normalized area. The simulational data–points accumulate at the theoretical values given by eq (3.62) for standing waves [table (3.1)].*

beginning slowing down of the amplitude growth, the system shows intermediate transitions to traveling waves which finally displace the standing wave, as shown in fig (5.8). In runs

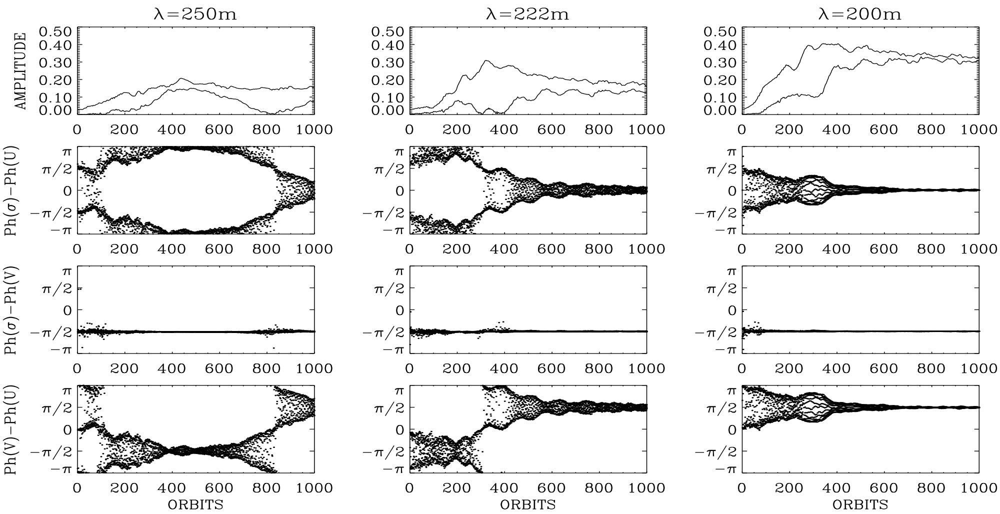

Figure 5.8: *The long time development of typical modes in a simulation with* $\tau = 1$. *The upper row shows the amplitude of density perturbations for three different wavelengths. The growth of the amplitude slows down and finally saturates after* $200 - 400$ *orbits. Also shown are the phase differences of the state variables for these wavelengths in course of the run. Initially, the phase differences are consistent with those of the linear standing wave solution. With growing amplitude, however, traveling waves seem to be preferred.*

without seed, both, standing waves and traveling waves are observed in the linear regime with a much more rapid transition to traveling waves only. The traveling waves seem to be the preferred state of the nonlinearly saturated modes. Also in this case the simulations show the phase differences of the hydrodynamic eigensolutions (3.62), i.e. for right moving waves ($B = 0$) and for left moving waves ($A = 0$) in spite of the fact that the hydrodynamic solutions are strictly only valid at marginal stability.

The preference of traveling waves observed in the simulations is consistent with the results of section 3.3. The coefficients of the Landau equation derived in that section imply the instability of standing waves with respect to traveling waves in the nonlinear regime. A snapshot of the traveling wave profiles from a simulation with $\tau = 1$ after 900 orbital revolutions is shown in fig (5.9) and opposed to the theoretical profiles—including nonlinear corrections—of section 3.3 for the isothermal model. The simulational profiles are a superposition of many modes in a system that is clearly not isothermal. Still, the single mode solution of the hydrodynamic model with first order nonlinear corrections covers qualitatively typical features of the simulated profiles.

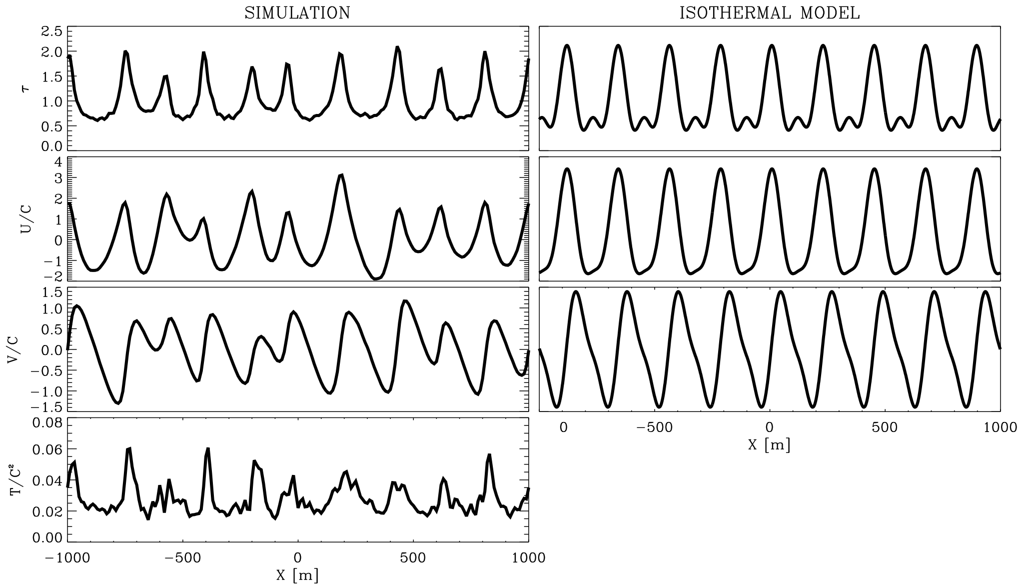

Figure 5.9: *Left: Radial profiles of the state variables of a simulation with* $\tau = 1$ *after 900 orbital revolutions. The nonlinearly saturated perturbations form traveling waves. Right: Profiles from the isothermal hydrodynamic model with nonlinear corrections.*

Chapter 6

Summary and Conclusions

Oscillatory instability (overstability) of dissipative Keplerian shear flow results from an interplay of the action of viscosity, trying to smooth density perturbations, and the inertial forces, i.e. the rotation of the system. Necessary for the onset of overstability is in general an increase of the kinematic viscosity with the density of the system. In usual gases this is not the case, the classical result is $\nu \propto \rho^{-1}$. However, in dense particle systems $\nu \propto \rho^{\alpha}$ with a positive exponent is possible through the collisional contribution to the viscous transport of momentum.

The work presented in this thesis addresses two main topics

- **Generalization of an isothermal model (Schmit & Tscharnuter, 1995) for viscous overstability in Saturn's main rings by the hydrodynamic energy balance equation.** The inclusion of the energy balance allows the flow to be locally and temporarily out of thermal equilibrium. The system has the tendency to reestablish a thermal equilibrium with a balance of the collisional loss of fluctuation energy by the viscous transfer of energy from the systematic motion into the ring particles' random motion. In the non–isothermal model proposed in this thesis this process is found to influence the development of the overstable modes: the **main effect is a stabilization of the overstability when compared to an isothermal system** with the same parameters, i.e. the growth of unstable modes is slowed down or overstability is even prevented.

- **Achievement of a quantitative agreement between the predictions of the hydrodynamic theory and molecular dynamics simulations** in the initial stage of viscous overstability where a linearized theory is applicable. This **agreement has been obtained within the non–isothermal model** where a number of parameters was determined in additional simulations (Salo et al., 2000b).

The simulations were carried out under the simplifying assumptions that have been made in the theory, i.e. identical spherical particles, neglect of rotational degrees of freedom (no surface friction), and no direct particle–particle self–gravity: the disk's self–gravity has been mimicked by an enhancement of the frequency of vertical oscillations. This leads to a flattening of the system with an increase of the collision frequency which strongly affects the transport processes. Especially, this high collision frequency, compared to the orbital frequency, provides a justification for a hydrodynamic description. The transport coefficients, shear viscosity, bulk viscosity, thermal conductivity, as well as the pressure and the granular cooling function, and their derivatives with respect to temperature and density are needed for the unperturbed ground state in the stability analysis of the non–isothermal hydrodynamical model. These values have been determined directly from simulations for various optical depths between $\tau = 0.5$ and $\tau = 2$. The ground state itself is characterized by the optical depth, the particle diameter, the model adopted for the dissipative particle collisions, and the Saturnocentric distance. The effect of approximating the self–gravity with the enhancement of the frequency of vertical oscillation enters the model solely through the altered transport coefficients. In this way a direct comparison of the oscillatory instability of the linearized hydrodynamic model and the initial growth of oscillatory modes in the simulations is possible.

6.1 Results

The hydrodynamic model for a dense planetary ring proposed in this thesis successfully describes the initial development of overstable oscillations in molecular dynamics simulations of a local region of the ring. In particular:

- **Quantitative agreement was found for the growth rates and the oscillation frequency** of the instability. **The critical wavelength for onset of overstability is correctly predicted** by the non–isothermal model. For a quantitatively correct description of the growth of the instability the inclusion of the energy balance equation in the analysis is important.

- The eigenfunctions of the linearized model **predict the observed phase shifts** and amplitude ratios of the oscillations in the mean fields of density and velocity of the simulations.

- A weakly nonlinear stability analysis of an isothermal **model suggests traveling waves to be the stable nonlinearly saturated solutions**. In simulations this is also observed: Standing waves are only transients, finally displaced by traveling waves.

- First order **corrections to the hydrodynamic eigenfunctions due to nonlinearity are in qualitative agreement** with the profiles of the nonlinear waves seen in the simulations.

6.2 Limitations of the Model

A number of simplifying assumptions is made in the hydrodynamic model. Where possible the same simplifications were made in the simulations in order to provide a good base for a comparison.

- In general, hydrodynamic modeling assumes that the velocity dispersion of the system can be described by a scalar value. However, in a sheared granular system the eigenvalues of the velocity dispersion tensor are different in general and its principal axes are not aligned with the radial and tangential direction (Salo et al., 2000b). The neglect of this anisotropy becomes more severe for systems of lower density. The focus of this thesis was on highly flattened disk's as the Saturnian B ring with a high collision frequency. The good quantitative agreement between theory and simulations gives an *a posteriori* justification for the **neglect of the temperature anisotropy in the model**. Still, temperature anisotropy micht affect other dynamical processes in the system.

- The **self–gravity of the particle disk is incorporated in the simulations by an enhancement of the frequency of vertical oscillations** which flattens the disk and thus increases the collision frequency. An inclusion of the more realistic direct particle–particle self–gravity in simulations leads to a similar enhancement of the collision frequency and overstability is retained in this case (Salo et al., 2000b). However, direct gravity leads in addition to the formation of non–axisymmetric gravitational wakes which then form an altered spatially inhomogeneous ground state for the ring's flow with different viscous properties. Such systems are nearer to the threshold of overstability for plausible parameters, when compared to the treatment with vertical frequency enhancement. Since in the case of direct particle–particle self–gravity the marginal curve has a minimum for finite wavelength it is possible that overstability is then restricted to a band of wavelengths around the wavelength of maximal growth.

- **Simulations and model deal with a system of uni–sized particles**. The question arises how the inclusion of a size distribution would alter the viscous overstability. Since the viscous properties of a collisional system are mainly determined by the largest particles, the overstability of a system with size-distribution and a given maximum particle radius should resemble a system of uni-sized particles of that radius with somewhat lower optical depth. Thus, the growth rates of overstable modes are expected to be smaller. First preliminary simulations seem to confirm this presumption. In Salo et al. (2000b) a simulational example is shown for a system with a differential size distribution $n(r) = r^{-3}$ ($r_{min} = 0.5$ m and $r_{max} = 5$ m) where overstability is observed.

- **Rotational degrees of freedom of the particles and friction are neglected**. In general, ring particles will carry spin angular momentum and in a collision spin and rotational energy is exchanged. Due to surface friction a part of the rotational energy will be dissipated in collisions. This additional loss mechanism is expected to lead to an enhanced flattening of the disk compared to a disk of smooth frictionless particles. This in turn will via an increase of the collision frequency enhance the shear viscosity of the system. Thus, the basic effect of friction should result in a stronger tendency for overstability with increased growth rates of oscillatory modes. This estimate is confirmed by preliminary simulations.

6.3 Conclusions and Outlook

"... wir seh'n betroffen den Vorhang zu und alle Fragen offen"

—Bertolt Brecht, *Der gute Mensch von Sezuan*

Hydrodynamic theory leads to a good quantitative description of the simulations that have been investigated in this thesis. This is in spite of the fact that a system with a comparatively small number of particles ($< 50,000$) is employed and the structure that is analyzed is of the order of 100 particle radii only. The inclusion of the energy balance is of crucial importance for the quantitative agreement. The Newtonian stress tensor and Fourier's Law themselves, relating the fluxes of momentum and energy linearly to the gradients of velocity and temperature, lead to a viable description of this non–equilibrium system. However, the transport coefficients have to be determined for the specific situation under consideration.

The results of the work summarized in this thesis substantiate the suggestion by Schmit & Tscharnuter (1995) that the Saturnian B ring is subject to viscous oscillatory instability. The stability boundary for the investigated model rings with the effect of self–gravity approximated by an enhanced frequency of oscillations is an optical depth of about $\tau = 1$ (corresponding to $\beta \equiv \partial \log \nu / \partial \log \sigma \sim 1$), optically thinner rings should be stable. The same stability boundary is also observed in simulations with self–gravitating particles.

Viscous oscillatory instability is thus a possible mechanism for the formation of radial structure in the B ring (optical depth $\tau \sim 2$). The critical wavelength of the instability is about $\lambda = 100\,\mathrm{m}$, where smaller wavelengths are stable. The wavelength with maximal growth rate is slightly larger. Thus, the oscillatory instability could account directly for the sub–km fluctuations in the optical depth profile of the B ring observed by the highest resolution Voyager experiments as the PPS (photo-polarimeter). At present it is not clear if these fluctuations can be attributed to non–axisymmetric gravitational wakes. The Cassini mission, to arrive at Saturn in 2004, will provide us with images of a resolution of less than 50 m per pixel. Thus, in these images it will be possible to distinguish the inclined wakes from purely radial oscillations due to overstability.

It cannot be concluded from the current level of understanding of the instability mechanism near the linear regime reached with this work if the formation of the observed B ring structure with typical scales of about 100 km can be attributed to viscous overstability. To answer this question a study of the interaction of the oscillatory modes is necessary which could lead to the generation of a longer scale structure on a much longer time scale than given by the linear growth rates. Such a process is reported in Schmit & Tscharnuter (1999) where the isothermal nonlinear hydrodynamic equations for Keplerian shear flow have been solved numerically. Interestingly, Schmit & Tscharnuter (1999) also observed a spatial variation of the amplitude of overstable oscillations on a scale of tens of kilometers. An investigation of the large scale structure possibly produced by viscous overstability could proceed in several directions.

- The weakly nonlinear analysis of the single mode time development and the nonlinear interaction of left and right moving traveling waves described in this thesis can be extended to the interaction of modes with different wavelengths. For a quantitative comparison to simulations the analysis has to be generalized to a non–isothermal model.

- Also, the weakly nonlinear analysis can be generalized to include spatial variations of the amplitude of the oscillations leading to a Ginzburg–Landau equation for the amplitude.

- Basing on the local simulation method a multi–domain code can be constructed that allows for the simulation of a larger region of a planetary ring on a parallel machine.

- A numerical solution scheme can be developed for the nonlinear non–isothermal hydrodynamic equations.

For parameter values which are plausible for the B ring a non–isothermal model is closer to the stability boundary as an isothermal model which would predict oscillatory instability even for optical thinner and non–selfgravitating rings. As argued above the inclusion of a size distribution of the particles in simulations additionally tends to further stabilize the system when compared to a simulation with the same optical depth but uni–sized particles. The basic effect of different particle sizes could be studied in a hydrodynamical model with a bimodal particle size–distribution. This would lead to similar balance laws for the mass density, the mass–averaged velocity and velocity dispersion, as in the uni-sized case but with modified transport coefficients, cooling function, and equation of state, which would contain now contributions from different particle species. The parameters for a stability analysis could again be determined in simulations.

Acknowledgment

This work would not have been possible without the help of many people. In particular, I want to express my thanks to:

My supervisor Dr habil Frank Spahn for the opportunity to work on this interesting topic, his permanent advise, and numerous stimulating and helpful discussions.

Dr Heikki Salo for the fruitful discussions and valuable scientific advise in course of our joint work on viscous overstability. I acknowledge the warm hospitality during my two stays at the University of Oulu.

Prof Dr Jürgen Kurths for his support during my work in his group. I thank him and all the members of the AGNLD for the friendly and productive atmosphere.

Dr Olaf Petzschmann, Dr Kai-Uwe Thiessenhusen, Ingo Wardinski, Dr Alexander Krivov, Miodrag Sremcevic, and Dr Frank Spahn for interesting discussions in our 'Ring–Group' and for the warm ambiance.

Dr Wolfgang Jansen for various helpful suggestions.

Ayhan Demircan, Dr Alexander Krivov, Dr Heikki Salo, and Dr Frank Spahn for corrections on the manuscript.

Birgit Nader for her friendliness and help in the office.

Jörg–Uwe Tessmer for the perfectly running computer network.

This work was supported by the Deutsche forschungsgemeinschaft, grant Sp 384/1-1.

Bibliography

A. Drecker, G. Rüdiger, R. Hollerbach (2000). Global structure of selfexcited magnetic fields arising from balbus–hawley instability. *Mon. Not. R. Astron. Soc*, **317**, 45.

Alam, M. & P.R. Nott (1998). Stability of plane Couette flow of a granular material. *J. Fluid Mech.*, **377**, 99–136.

Andrews, J.P. (1930). Theory of collision of spheres of soft metals. *Phil. Mag*, **9**, 593.

Araki, S. & S. Tremaine (1986). The dynamics of dense particle disks. *Icarus*, **65**, 83–109.

Arnarson, B.Ö. & J.T. Willits (1998). Thermal diffusion in binary mixtures of smooth, nearly elastic spheres with and without gravity. *Phys. Fluids*, **10**, 1324–1328.

Balbus, S.A. & J.F. Hawley (1991). A powerful local shear instability in weakly magnetized disks. I. linear analysis. *Astrophysical Journal*, **376**, 214–222.

Balbus, S.A. & J.F. Hawley (1996). Nonlinear stability, hydrodynamical turbulence, and transport in disks. *Astrophysical Journal*, **467**, 76–86.

Binney, J. & S. Tremaine (1987). *Galactic Dynamics*. Princeton University Press.

Blumenthal, G. R., L. T. Yang & D. N. C. Lin (1984). On the overstability of axisymmetric oscillations in thin accretion disks. *Astrophys. J.*, **287**, 774–784.

Bobylev, V.A. (1984). Exact solutions of the nonlinear Boltzmann equation and the theory of Maxwell gas relaxation. *Theor. Math. Phys.*, **60**, 280–310.

Borderies, N., P. Goldreich & S. Tremaine (1985). A granular flow model for dense planetary rings. *Icarus*, **63**, 406–420.

Borderies, N., P. Goldreich & S. Tremaine (1986). Nonlinear density waves in planetary rings. *Icarus*, **68**, 522–533.

Brahic, A. & B. Sicardy (1981). Apparent thickness of Saturn's rings. *Nature*, **289**, 447–450.

Brey, J.J., F. Moreno & J.W. Dufty (1996). Model kinetic equation for low–density granular flow. *Physical Review E*, **54**, 445–456.

Bridges, F.G., A.P. Hatzes & D.N.C. Lin (1984). Structure, stability and evolution of Saturn's rings. *Nature*, **309**, 333–338.

Brilliantov, N., T. Pöschel, F. Spahn & J.-M. Hertzsch (1996). The collision of particles in granular systems. *Physica A*, **231**, 417.

BURNS, J. A., J. N. CUZZI, R. H. DURISEN & P. HAMILL (1979). On the 'thickness' of Saturn's rings caused by satellite and solar perturbations and by planetary precession. *Astronomical Journal*, **84**, 1783–1801.

CARNAHAN, N.F. & K.E. STARLING (1969). Equations of state for non-attracting rigid spheres. *J. Chem. Phys.*, **51**, 635–636.

CHANDRASEKHAR, S. (1981). *Hydrodynamic and Hydrodmagnetic Stability*. Dover Publications, Inc.

CHAPMAN, S. & T.G. COWLING (1970). *The mathematical theory of non-uniform gases*. Cambridge University Press, Cambridge.

CROSS, M.C. & P.C. HOHENBERG (1993). Pattern formation outside of equilibrium. *Reviews of Modern Physics*, **65**(3), 851.

CUZZI, J. N. & R. H. DURISEN (1990). Bombardment of planetary rings by meteoroids - General formulation and effects of Oort Cloud projectiles. *Icarus*, **84**, 467–501.

CUZZI, J. N. & P. R. ESTRADA (1998). Compositional Evolution of Saturn's Rings Due to Meteoroid Bombardment. *Icarus*, **132**, 1–35.

CUZZI, J. N., J.J. LISSAUER, L.W. ESPOSITO, J.B. HOLBERG, E.A. MAROUF, G.L. TYLER & A. BOISCHOT (1984). Saturn's rings: Properties and processes. In R. GREENBERG & A. BRAHIC (Eds.), *Planetary Rings*, pp. 73–199. The University of Arizona Press.

CUZZI, J. N. & J. D. SCARGLE (1985). Wavy edges suggest moonlet in Encke's gap. *Astrophys. J.*, **292**, 276–290.

DEBRULLE, B. & E. KNOBLOCH (1992). On the local stability of accretion disks. *Astronomy and Astrophysics*, **256**, 673–678.

DURISEN, R. H. (1984). Transport effects due to particle erosion mechanisms. In *Planetary Rings*, pp. 416–446.

DURISEN, R. H., P. W. BODE, J. N. CUZZI, S. E. CEDERBLOOM & B. W. MURPHY (1992). Ballistic transport in planetary ring systems due to particle erosion mechanisms. II - Theoretical models for Saturn's A- and B-ring inner edges. *Icarus*, **100**, 364–393.

DURISEN, R. H., P. W. BODE, S. G. DYCK, J. N. CUZZI, J. D. DULL & J. C. II WHITE (1996). Ballistic Transport in Planetary Ring Systems Due to Particle Erosion Mechanisms. *Icarus*, **124**, 220–236.

DURISEN, R. H., N. L. CRAMER, B. W. MURPHY, J. N. CUZZI, T. L. MULLIKIN & S. E. CEDERBLOOM (1989). Ballistic transport in planetary ring systems due to particle erosion mechanisms. I - Theory, numerical methods, and illustrative examples. *Icarus*, **80**, 136–166.

DURISEN, RICHARD H. (1999). *Mercury*, **September–October**.

ESPOSITO, L. W., M. OCALLAGHAN & R. A. WEST (1983). The structure of Saturn's rings - Implications from the Voyager stellar occultation. *Icarus*, **56**, 439–452.

ESTRADA, P. R. & J. N. CUZZI (1996). Voyager Observations of the Color of Saturn's Rings. *Icarus*, **122**, 251–272.

French, R. G., J. Cuzzi, L. Dones & H. Salo (2000). *HST observations of azimuthal brightness asymmetry in Saturn's rings.* Division of Dynamical Astronomy Meeting, Yosemite, April 9–12, 2000.

Goertz, C. K. & G. Morfill (1988). A new instability of Saturn's rings. *Icarus*, **74**, 325–330.

Goertz, C. K., G. E. Morfill, W. H. Ip, E. Grün & O. Havnes (1986). Electromagnetic angular momentum transport in Saturn's rings. *Nature*, **320**, 141–143.

Goldhirsch, I. & G. Zanetti (1993). Clustering instability in dissipative gases. *Phys. Rev. Lett.*, **70**, 1619–1622.

Goldreich, P. & D. Lynden-Bell (1964). Spiral arms as sheared gravitational instabilities II.. *Mon. Not. R. Astron. Soc*, **130**, 125–158.

Goldreich, P. & S. Tremaine (1978b). The excitation and evolution of density waves. *Astrophys. J.*, **222**, 850–858.

Goldreich, P. & S. Tremaine (1978a). The velocity dispersion in Saturn's rings. *Icarus*, **34**, 227–239.

Goldshtein, A. & M. Shapiro (1995). Mechanics of collisional motion of granular materials. Part1. General hydrodynamic equations. *J. Fluid Mech.*, **282**, 75–114.

Grad, H. (1949). On the kinetic theory of rarified gases. *Comm. Pure and Appl. Math.*, **2**, 331–407.

Greenberg, R. & A. Brahic (Eds.) (1984). *Planetary Rings.* The University of Arizona Press.

Grün, E., G. E. Morfill, R. J. Terrile, T. V. Johnson & G. Schwehm (1983). The evolution of spokes in Saturn's B ring. *Icarus*, **54**, 227–252.

Grün, E., G. E. Morfill & D. A. Mendis (1984). Dust-magnetosphere interactions. In R. Greenberg & A. Brahic (Eds.), *Planetary Rings*, pp. 275–332. Univ. of Arizona Press, Tucson Arizona.

Hamilton, P. D. & A. V. Hamilton (1996). Circumplanetary dust Dynamics: Effects of solar gravity, radiation pressure, planetary oblateness, and electromagnetism. *Icarus*, **123**, 503–523.

Hénon, M. (1981). A simple model of Saturn's rings. *Nature*, **293**, 33–35.

Hill, G.W. (1878). Researches in the lunar theory. *Am. J. Math.*, **1**, 5–26.

Holberg, J.B., W.J. Forrester, D.E. Shemansky & D. Barry (1982). Voyager absolute far–ultraviolet spectrophotometry of hot stars. *Ap. J.*, **257**, 656–671.

Hopkins, M.A. & M.Y. Louge (1991). Inelastic microstructure in rapid granular flows. *Phys. Fluids A*, **3**, 47–57.

Horn, L. J. & J. N. Cuzzi (1996). Characteristic Wavelengths of Irregular Structure in Saturn's B Ring. *Icarus*, **119**, 285–310.

Huang, K. (1963). *Statistical Mechanics.* Wiley & Sons.

HUTTER, K. (1996). Avalanche dynamics. In V.P. SINGH (Ed.), *Hydrology of Disasters*, p. 317. Kluwer Academic Publ. Dordrecht 1996.

JEFFREYS, H. (1947). The effects of collisions on Saturn's rings. *Mon. Not. Roy. Astron. Soc.*, **107**, 263–267.

JENKINS, J.T. & F. MANCINI (1989). Kinetic theory for binary mixtures of smooth, nearly elastic shperes. *Phys. Fluids A*, **1**, 2050–2057.

JENKINS, J.T. & M.T. RICHMAN (1985). Grad's 13-moment system for a dense gas of inelastic spheres. *Arch. Ration. Mech. Anal.*, **87**, 355–377.

JULIAN, W. H. & A. TOOMRE (1966). Non-axisymmetric responses of differentially rotating disks of stars. *Astrophys. J.*, **146**, 810–830.

KATO, S. (1978). Pulsational instability of accretion disks to axially symmetric oscillations. *Mon. Not. R. Astron. Soc.*, **185**, 629–642.

KLEIBER, R. & W. GLATZEL (1999). On the stability of viscous accretion tori. *Mon. Not. R. Astron. Soc.*, **303**, 107–115.

KLEY, W., C.B. PAPALOIZOU & D.N.C. LIN (1993). Two–dimensional voscous accretion disk models. II. on viscous overstability. *Astropyhysical Journal*, **409**, 739–747.

KUIPER, G.P., D.P. CRUIKSHANK & U. FINK (1970). The composition of Saturn's rings. *Sky Teles.*, **39**, 14.

KUWABARA, G. & K. KONO (1987). Restitution coefficient in a collision between two spheres. *Jap. J. Appl. Phys.*, **26**, 1230–1233.

LANE, A.L., C.W. HORD, R.A. WEST, L.W. ESPOSITO, D.L. COFFEEN, M. SATO, K.E. SIMMONS, R.B. POMPHREY & R.B. MORRIS (1982). Photopolarimetry from Voyager 2: Preliminary results on Saturn, Titan, and the rings. *Science*, **215**, 537–543.

LIN, D. N. C. & P. BODENHEIMER (1981). On the stability of Saturn's rings. *Astrophys. J. Lett.*, **248**, L83–L86.

LISSAUER, J. J. & J. N. CUZZI (1982). Resonances in Saturn's rings. *Astronomical Journal*, **87**, 1051–1058.

LISSAUER, J. J., F. H. SHU & J. N. CUZZI (1981). Moonlets in Saturn's rings. *Nature*, **292**, 707–711.

LONGARETTI, P.Y. & N. RAPPAPORT (1995). Viscous overstabilities in dense narrow planetary rings. *Icarus*, **116**, 810–827.

LUKKARI, J. (1981). Collisional amplification of density fluctuations in Saturn's rings. *Nature*, **292**, 433–435.

LUN, C.K.K., S.B. SAVAGE, D. J. JEFFREY & N. CHEPURNIY (1984). Kinetic theories for granular flow: inelastic particles in Cuette flow and slightly inelastic particles in a general flow field. *J. Fluid Mech.*, **140**, 223–256.

LYNDEN-BELL, D. & J.E. PRINGLE (1974). The evolution of viscous discs and the origin of the nebular variables. *Mon.Not.Roy.Astron.Soc*, **168**, 603–637.

Marouf, E. A., G. L. Tyler & V. R. Eshleman (1982). Theory of radio occultation by Saturn's rings. *Icarus*, **49**, 161–193.

Marouf, E. A., G. L. Tyler, H. A. Zebker, R. A. Simpson & V. R. Eshleman (1983). Particle size distributions in Saturn's rings from Voyager 1 radio occultation. *Icarus*, **54**, 189–211.

Maxwell, J.C. (1859). *On the stability of the Motions of Saturn's Rings.* Cambridge and London: MacMillan and Co.

Morgado, W. A. M. & I. Oppenheim (1997). Energy dissipation for quasielastic granular particle collisions. *Phys. Rev. E*, **55**, 1940–1945.

Mosqueira, I. (1996). Local Simulations of Perturbed Dense Planetary Rings. *Icarus*, **122**, 128–152.

Nicholson, P. D., M. R. Showalter, L. Dones, R. G. French, S. M. Larson, J. J. Lissauer, C. A. McGhee, B. Sicardy, P. Seitzer & G. E. Danielson (1996). Observations of Saturn's ring-plane crossing in August and November 1995. *Science*, **272**, 509–516.

Nicholson, P.D., R.G. French, E. Tollestrup, J.N. Cuzzi, J. Harrington, K. Matthews, O. Perkovic & R.J. Stover (2000). Saturns rings I: Optical depth profiles from the 28 sgr occultation. *Icarus*, **145**, 474–501.

Papaloizou, J. C. B. & D. N. C. Lin (1988). On the pulsational overstability in narrowly confined viscous rings. *Astrophys. J.*, **331**, 838–860.

Papaloizou, J. C. B. & D. N. C. Lin (1989). Nonaxisymmetric instabilities in thin self–gravitating rings and disks. *Astrophys. J.*, **344**, 645–668.

Petzschmann, O., U. Schwarz, F. Spahn, C. Grebogi & J. Kurths (1999). Length scales of clustering in granular gases. *Phys. Rev. Lett.*, **82**, 4819–4822.

Pilcher, C.B., C. Chapman, L.A. Lebofsky & H.H. Kieffer (1970). Saturn's rings: Identification of water frost. *Science*, **167**, 1372–1373.

Poulet, F., B. Sicardy, C. Dumas, L. Jorda & D. Tiphene (2000). The crossings of Saturn ring plane by the earth in 1995: ring thickness. *Icarus*, **145**, 147–165.

Raman, C.V. (1918). The photographic study of impact at minimal velocities. *Phys. Rev*, **12**, 442.

Résibois, P. & M. De Leener (1977). *Classical kinetic theory of fluids.* Wiley & Sons, New York.

Rosen, P. A., G. L. Tyler, E. A. Marouf & J. J. Lissauer (1991). Resonance structures in Saturn's rings probed by radio occultation. II - Results and interpretation. *Icarus*, **93**, 25–44.

Rüdiger, G., L. Primavera, R. Arlt & D Elstner (1999). Magnetic shear–flow instability in thin accretion disks. *Mon. Not. R. Astron. Soc.*, **306**, 913.

Salo, H. (1991). Numerical simulations of dense collisional systems. *Icarus*, **90**, 254–270.

Salo, H. (1992a). Gravitational wakes in Saturn's rings. *Nature*, **359**, 619–621.

SALO, H. (1992b). Numerical simulations of dense collisional systems: II. Extended distribution of particle size. *Icarus*, **96**, 85–106.

SALO, H. (1995). Simulations of dense planetary rings. III. Self-gravitating identical particles. *Icarus*, **117**, 287–312.

SALO, H., J KARJALAINEN & R. G. FRENCH (2000a). *Modeling the azimuthal brightness asymmetry in Saturn's rings.* Americal Astronomical Society, Division of Dynamical Astronomy Meeting, Yosemite, April 9–12, 2000.

SALO, H., J. SCHMIDT & SPAHN F. (2000b). *Viscous overstability in Saturn's B ring: I. Direct simulations and mesurement of transport coefficients.* submitted to Icarus.

SAVAGE, S.B. (1992). Instability of an unbounded uniform granular shear flow. *J. Fluid Mech.*, **241**, 109.

SAVAGE, S.B. & K. HUTTER (1989). The motion of a finite mass of granular material down a rough incline. *J. Fluid Mech.*, **199**, 177.

SCHMIDT, J., H. SALO, O. PETZSCHMANN & F. SPAHN (1999). Vertical distribution of temperature and density in a planetary ring. *Astron. and Astrophys.*, **345**, 646–652.

SCHMIDT, J., H. SALO, F. SPAHN & OLAF PETZSCHMANN (2000). Viscous overstability in Saturn's b ring: II hydrodynamic theory and comparison to simulations. submitted to Icarus.

SCHMIT, U. & W.M. TSCHARNUTER (1995). A fluid dynamical treatment of the common action of self-gravitation, collisions, and rotation in Saturn's B-ring. *Icarus*, **115**, 304–319.

SCHMIT, U. & W.M. TSCHARNUTER (1999). On the formation of the fine–scale structure in Saturn's B ring. *Icarus*, **138**, 173–187.

SELA, N. & I. GOLDHIRSCH (1998). Hydrodynamic equations for rapid flows of smooth inelastic spheres, to Burnett order. *J. Fluid Mech.*, **361**, 41–74.

SHAN, LIN-HUA & C. K. GOERTZ (1991). On the radial structure of Saturn's B ring. *Astrophys. J.*, **367**, 350–360.

SHOWALTER, M. R. (1991). Visual detection of 1981S13, Saturn's eighteenth satellite, and its role in the Encke gap. *Nature*, **351**, 709–713.

SHOWALTER, M. R., J. N. CUZZI, E. A. MAROUF & L. W. ESPOSITO (1986). Satellite 'wakes' and the orbit of the Encke Gap moonlet. *Icarus*, **66**, 297–323.

SHU, F. H. (1984). Waves in planetary rings. In *Planetary Rings*, pp. 513–561.

SHU, F. H., J. N. CUZZI & J. J. LISSAUER (1983). Bending waves in Saturn's rings. *Icarus*, **53**, 185–206.

SHU, F. H., L. DONES, J. J. LISSAUER, C. YUAN & J. N. CUZZI (1985b). Nonlinear spiral density waves - Viscous damping. *Astrophys. J.*, **299**, 542–573.

SHU, F.H., C. YUAN & J.J. LISSAUER (1985a). Nonlinear spiral density waves: an inviscid theory. *Astrophys. J.*, **291**, 356–376.

SHUKHMAN, I.G. (1984). Collisional dynamics of particles in Saturn's rings. *Sov. Astron.*, **AJ 28**, 574–585.

SIMON, V. & J.T. JENKINS (1994). On the vertical structure of dilute planetary rings. *Icarus*, **110**, 109–116.

SMITH, B. A., L. SODERBLOM, R. M. BATSON, P. M. BRIDGES, J. L. INGE, H. MASURSKY, E. SHOEMAKER, R. F. BEEBE, J. BOYCE, G. BRIGGS, A. BUNKER, S. A. COLLINS, C. HANSEN, T. V. JOHNSON, J. L. MITCHELL, R. J. TERRILE, A. F. COOK, J. N. CUZZI, J. B. POLLACK, G. E. DANIELSON, A. P. INGERSOLL, M. E. DAVIES, G. E. HUNT, D. MORRISON, T. OWEN, C. SAGAN, J. VEVERKA, R. STROM & V. E. SUOMI (1982). A new look at the Saturn system - The Voyager 2 images. *Science*, **215**, 505–537.

SPAHN, F., J. SCHMIDT, O. PETZSCHMANN & H. SALO (2000). Stability analyses of a Keplerian disk of granular grains: influence of thermal diffusion. *Icarus*, **145**, 657–660.

SPAHN, F., U. SCHWARZ & J. KURTHS (1997). Clustering of granular assemblies with temperature dependent restitution and under Keplerian differential rotation. *Phys. Rev. Lett.*, **78**, 1596–1599.

SPAHN, F. & H. SPONHOLZ (1989). Existence of moonlets in Saturn's rings inferred from the optical depth profile. *Nature*, **339**, 607–608.

SPAHN, F. & M. SREMČEVIĆ (2000). Density patterns induced by small moonlets in Saturn's rings? *Astron. & Astrophys.*, **358**, 368–372.

SPAHN, F. & H. J. WIEBICKE (1989). Long-term gravitational influence of moonlets in planetary rings. *Icarus*, **77**, 124–134.

SPAHN, FRANK (1992). Strukturen in planetaren Ringen. *Physik in unserer Zeit*, **3**.

STEWART, G. R., D. N. C. LIN & P. BODENHEIMER (1984). Collision-induced transport processes in planetary rings. In R. GREENBERG & A. BRAHIC (Eds.), *Planetary Rings*, pp. 447–512. Univ. of Arizona Press, Tucson Arizona.

THORNTON, C. (1997). Coefficient of restitution for collinear collisions of elastic-perfectly plastic spheres. *Journal of Applied Mechanics*, **64**, 383–386.

TOOMRE, A. (1964). On the gravitational stability of a disk of stars. *Astrophys. J.*, **139**, 1217–1238.

TOOMRE, A. (1981). On the gravitational stability of a disk of stars. *Astrophys. J.*, **139**, 1217–1238.

TRULSEN, J. (1971). What amplifies the spirals?. In S. M. FALL & D. LYNDEN-BELL (Eds.), *The structure and evolution of normal galaxies*, pp. 111–136. Cambridge Univ. Press

WARD, W. R. (1981). On the radial structure of Saturn's rings. *Geophys. Res. Lett.*, **8**, 641–643.

WISDOM, J. & S. TREMAINE (1988). Local simulations of planetary rings. *Astronomical Journal*, **95**, 925–940.

ZEBKER, H. A., E. A. MAROUF & G. L. TYLER (1985). Saturn's rings - Particle size distributions for thin layer model. *Icarus*, **64**, 531–548.

Appendix A

Kinetic Theory

In this appendix the derivation of balance laws of a many–particle system for mass, momentum, and energy, from a kinetic equation (Boltzmann's or Enskog's equation) is shortly described. A detailed report on kinetic theory of dense gases can be found in Chapman & Cowling (1970) or in (Résibois & De Leener, 1977). An extension to the case of inelastic collisions is given for instance in Lun et al. (1984) or Jenkins & Richman (1985).

Boltzmann's equation

Boltzmann's theory assumes that the development of a non–equilibrium N-particle system can be described in terms of the evolution of the one particle distribution function $f(\vec{x}, \vec{v}, t)$. The theory employs aspects as different as the purely mechanical and deterministic two body interaction of two particles as well as probabilistic assumptions concerning the distribution function and the statistical properties of the particle ensemble. Boltzmann defines the one particle distribution function in such a way that

$$f(\vec{x}, \vec{v}, t) \mathrm{d}^3 x \, \mathrm{d}^3 v \tag{A.1}$$

is the number of particles at the time t in the volume increment $\mathrm{d}^3 x$ at the location $\vec{x}$ and the velocity increment $\mathrm{d}^3 v$ around $\vec{v}$. The increments $\mathrm{d}^3 x$ and $\mathrm{d}^3 v$ are assumed to be small compared to the variations of macroscopic properties of the system but still contain a large number of particles. The time evolution of f is then governed by the Boltzmann equation

$$\begin{aligned}\left(\frac{\partial}{\partial t} + \vec{v} \cdot \frac{\partial}{\partial \vec{x}} + \vec{F} \cdot \frac{\partial}{\partial \vec{v}}\right) f(\vec{x}, \vec{v}, t) \quad = \quad & \int \mathrm{d}^3 v_1 \int \mathrm{d}^2 \Omega \, g \, \sigma \\ & \times \left[f(\vec{x}, \vec{v}', t) f(\vec{x}, \vec{v}_1', t) - f(\vec{x}, \vec{v}, t) f(\vec{x}, \vec{v}_1, t) \right] .\end{aligned} \tag{A.2}$$

It expresses the fact that a change of $f(\vec{x}, \vec{v}, t)$ with time is caused by a flux of particles out of the phase space volume $\mathrm{d}^3 x \, \mathrm{d}^3 v$ (second and third term on the left hand side) or by binary collisions (right hand side) that may decrease or increase the number of particles at $\mathrm{d}^3 x \, \mathrm{d}^3 v$. In this appendix Ω denotes the solid angle element and σ the particles' cross section. The velocity difference of colliding particles is denoted by

$$\vec{g} = \vec{v} - \vec{v}_1 \, . \tag{A.3}$$

The primed velocities are post–collisional velocities, connected to the pre-collisional ones via

$$\begin{aligned}\vec{v}_1' &= \vec{v}_1 - \vec{n}(\vec{g} \cdot \vec{n}) \\ \vec{v}' &= \vec{v} + \vec{n}(\vec{g} \cdot \vec{n}) \, .\end{aligned} \tag{A.4}$$

In the collision term [right hand side of eq (A.2)] the contributions from *binary collisions* are summed up that leave a particle with velocity $\vec{v}$ at position and time $\vec{x}$ and t, or remove one from $\vec{x}$ and t. Both types of collisions are shown in fig (A.1). In the Boltzmann collision term the pair distribution function is approximated by the product of two single particle distribution functions. This is the so called *molecular chaos assumption* (Boltzmann called it "Stosszahlansatz"), meaning that particles that are going to collide are uncorrelated.

The Maxwell–Boltzmann distribution function is a solution of eq (A.2) at equilibrium, i.e. for a vanishing collision term (Huang, 1963).

Dense hard sphere gases

In Boltzmann's theory the particle volume enters solely through the cross section in the collision integral. In dense systems of macroscopic particles, as in granular material, and so in a planetary ring, there are additional effects. So, the volume for the dynamics of the system is reduced geometrically by the particles proper volume. This leads to an enhancement of the pressure (similar to the concept of covolume in the Van der Waals equilibrium equation of state) and to an increased collision frequency. Further, collisions can no more considered to be local. In a collision momentum and energy are transferred instantaneously over the distance of a particle diameter [see fig (4.4)]. Thus, in dense systems additional nonlocal (or collisional) contributions to the fluxes arise.

The inclusion of these effects in the kinetic equation requires a modification of the collision term of the Boltzmann equation (A.2). The locations of two particles in a collision have to be distinguished, leading to the replacement

$$\begin{aligned} f(\vec{v},\vec{x},t)\, f(\vec{v}_1,\vec{x},t) \quad &\rightarrow \quad f(\vec{v},\vec{x},t)\, f(\vec{v}_1,\vec{x}-a\vec{n},t) \\ f(\vec{v}',\vec{x},t)\, f(\vec{v}_1',\vec{x},t) \quad &\rightarrow \quad f(\vec{v}',\vec{x},t)\, f(\vec{v}_1',\vec{x}+a\vec{n},t) \end{aligned} \tag{A.5}$$

where a is the particles diameter, and $\vec{n}$ the vector pointing from particle with velocity $\vec{v}_1$ to the one with velocity $\vec{v}$. Both collisions are pictured in fig (A.1).

To account for the increased collision frequency due to the finite volume occupied by the particles the collision frequencies [eq (A.5]) have to be multiplied by an enhancement factor evaluated at the point of contact

$$\begin{aligned} f(\vec{v},\vec{x},t)\, f(\vec{v}_1,\vec{x}-a\vec{n},t) \quad &\rightarrow \quad g_0(\vec{x}-\frac{a}{2}\vec{n})\, f(\vec{v},\vec{x},t)\, f(\vec{v}_1,\vec{x}-a\vec{n},t) \\ f(\vec{v}',\vec{x},t)\, f(\vec{v}_1',\vec{x}+a\vec{n},t) \quad &\rightarrow \quad g_0(\vec{x}+\frac{a}{2}\vec{n})\, f(\vec{v}',\vec{x},t)\, f(\vec{v}_1',\vec{x}+a\vec{n},t)\,. \end{aligned} \tag{A.6}$$

g_0 is the radial distribution function. It has been calculated for example by Carnahan & Starling (1969) for a fluid of identical hard spheres. In terms of the filling factor $\mathit{ff} = \rho/\rho_p$, with the particles bulk density ρ_p it reads

$$g_0(\vec{x}) = \frac{2-\mathit{ff}(\vec{x})}{2(1-\mathit{ff}(\vec{x}))^3}\,, \quad g_0 \geq 1\,. \tag{A.7}$$

The collision term for hard spheres then reads

$$\begin{aligned} \left.\frac{\partial f}{\partial t}\right|_{col} = &\int \mathrm{d}^3 v_1 \int \mathrm{d}^2\Omega\, g\, \sigma \\ &\times \Big[g_0(\vec{x}+\frac{a}{2}\vec{n})\, f(\vec{v}',\vec{x},t)\, f(\vec{v}_1',\vec{x}+a\vec{n},t) - g_0(\vec{x}-\frac{a}{2}\vec{n})\, f(\vec{v},\vec{x},t)\, f(\vec{v}_1,\vec{x}-a\vec{n},t) \Big] \end{aligned} \tag{A.8}$$

With this collision integral the kinetic equation (A.2) is called the Enskog equation.

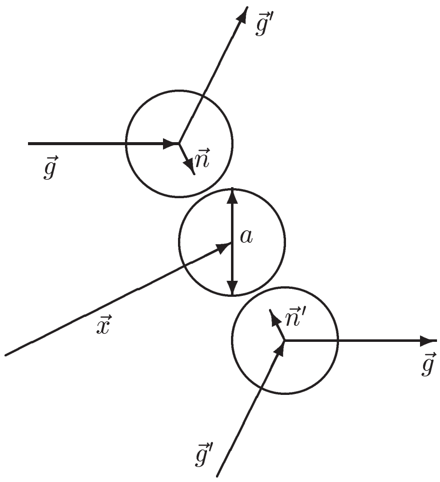

Figure A.1: *Elastic collision of hard spheres of diameter a. Collision of the upper spheres: A sphere initially at ($\vec{v}$, $\vec{x}$, t) is deflected to another velocity. Collision of the lower spheres:A sphere is left at ($\vec{v}$, $\vec{x}$, t) after the collision ($\vec{n}' = -\vec{n}$).*

Inelastic collisions
An additional modification of the collision term arises when the hard sphere collisions are allowed to be inelastic (Trulsen, 1971; Goldshtein & Shapiro, 1995; Sela & Goldhirsch, 1998). Then eq (A.4) has to be modified, so that

$$\vec{v}'_{1,2} = \vec{v}_{1,2} \mp \frac{1+\epsilon}{2}(\vec{g}\cdot\vec{n})\vec{n} \tag{A.9}$$

where ϵ is the normal coefficient of restitution. Often ϵ is assumed to be independent of the impact velocity, and it is defined as

$$\epsilon = -\frac{\vec{n}\cdot\vec{g}'}{\vec{n}\cdot\vec{g}}\,, \quad 0 < \epsilon < 1\,. \tag{A.10}$$

Reconsidering carefully all the arguments that led to the Boltzmann collision term and the modifications due to the close packing of particles in a dense gas yields

$$\begin{aligned} \left.\frac{\partial f}{\partial t}\right|_{col} &= \int \mathrm{d}^3 v_1 \int \mathrm{d}^2\Omega\, g\, \sigma \\ &\times \left[\frac{g_0(\vec{x}+\frac{a}{2}\vec{n})}{\epsilon^2} f(\vec{v}',\vec{x},t)\, f(\vec{v}'_1,\vec{x}+a\vec{n},t) - g_0(\vec{x}-\frac{a}{2}\vec{n})\, f(\vec{v},\vec{x},t)\, f(\vec{v}_1,\vec{x}-a\vec{n},t)\right] \end{aligned} \tag{A.11}$$

In an inelastic system the collisional gain term for the velocity distribution function has more weight.

The distribution function
A solution of the complicated kinetic equation for the distribution function f is in general impossible. However, there exist solution schemes for approximate solutions of the non–equilibrium distribution function f that do not deviate too much from the Maxwellian distribution. Such approximation schemes are

- Linearization of the kinetic equation in terms of a small deviation of f from the Maxwell–Boltzmann equilibrium solution. The small deviation can be regarded as a first order non–equilibrium correction. This first order correction is additionally expanded in a series of orthogonal functions (e.g. Sonine polynomials, see Résibois & De Leener (1977)) and the first coefficients of that series can be computed.
- Grad's moment method (Grad, 1949). f is expanded in terms of gradients of the Maxwell–Boltzmann distribution. Grad shows that a subset of 13 coefficient of the general expansion is enough to obtain a closed set of equations.
- the Chapman–Enskog method. This is the most sophisticated solution scheme. It gives a solution for the non–equilibrium distribution function in terms of successive approximation. At increasing degrees of approximation the Euler–equations, the Navier–Stokes equations, and the Burnett equations are obtained (Chapman & Cowling, 1970).

Grad's moment method was extended by Jenkins & Richman (1985) to the case of dense gases of inelastic spheres with a velocity independent coefficient of restitution. The coefficient of restitution enters through the 13 moment coefficients in the transport coefficients and the equation of state.

Balance laws

In terms of the single particle distribution function f mean values can be defined for any given quantity ψ

$$\langle \psi(\vec{x},t) \rangle \equiv \frac{\int \mathrm{d}^3 v\, \psi\, f(\vec{v},\vec{x},t)}{\int \mathrm{d}^3 v\, f(\vec{v},\vec{x},t)}\,, \tag{A.12}$$

and the systems mass density, mean velocity, and temperature are

$$\rho = m_p \int \mathrm{d}^3 v\, f(\vec{v},\vec{x},t) \tag{A.13}$$

$$\vec{u} = \langle \vec{v} \rangle \tag{A.14}$$

$$T = \frac{1}{3} \langle (\vec{v}-\vec{u})^2 \rangle \tag{A.15}$$

For any quantity ψ balance equations can be written down, multiplying the kinetic equation [eq (A.2) for dilute gases, or with the collision term (A.8) for dense systems] with ψ and integrating over $\mathrm{d}^3 v$. For dilute systems it is particularly convenient to compute balance laws for *collisional invariants* as the mass, momentum, and energy. The conservation of these quantities in a collision leads to a vanishing collisional contribution to the balance when the collision term of eq (A.2) is used.

With the collision term (A.8), in general, there arise additional flux terms in the balance equations, even for collisional invariants, as a consequence of the nonlocal nature of the collision. Practically these contributions are evaluated approximately (Résibois & De Leener, 1977), expanding the functions $g_0(\vec{x}+\frac{a}{2}\vec{n})$ and $f(\vec{v}_1',\vec{x}\pm a\vec{n},t)$ about $\vec{x}$ in powers of a, keeping only terms up to second order in a. This results in the balance equations

$$\frac{\partial \rho}{\partial t} + u_\alpha \nabla_\alpha \rho = -\rho \nabla_\alpha u_\alpha \tag{A.16}$$

$$\rho \left(\frac{\partial}{\partial t} + u_\beta \nabla_\beta \right) u_\alpha = \rho F_\alpha - \nabla_\beta \left(\widehat{P}_{\alpha\beta} + P^{coll}_{\alpha\beta} \right) \tag{A.17}$$

$$\frac{3}{2}\rho \left(\frac{\partial}{\partial t} + u_\beta \nabla_\beta \right) T = -\nabla_\alpha q_\alpha - \widehat{P}_{\alpha\beta} \nabla_\beta u_\alpha - \Gamma\,. \tag{A.18}$$

The stress tensor and the energy flux vector are

$$\widehat{P}_{\alpha\beta} = \rho\langle(v_\alpha - u_\alpha)(v_\beta - u_\beta)\rangle + \widehat{P}^{coll}_{\alpha\beta} \tag{A.19}$$

$$q_\alpha = \frac{1}{2}\rho\langle(v_\alpha - u_\alpha)(\vec{v} - \vec{u})^2\rangle + q^{coll}_\alpha \tag{A.20}$$

where $\widehat{P}^{coll}_{\alpha\beta}$ and q^{coll}_α are the collisional parts of the total stress tensor and the heat flow vector, respectively. The term Γ in the last equation of (A.16) is zero for systems with elastic particles. It is the collisional sink term that arises if $\epsilon < 1$ when the collision term (A.11) is used.

Constitutive equations

When the distribution function is specified as a solution of the kinetic equation (exact or approximately) explicit expressions can be computed for the stress tensor, the heat flow vector, and in case of inelastic collisions for the cooling function Γ. By comparison to the Newtonian expression for the stress

$$\widehat{P}_{\alpha\beta} = p\delta_{\alpha\beta} - 2\eta\widehat{D}_{\alpha\beta} - \xi\nabla_\mu u_\mu \delta_{\alpha\beta} \tag{A.21}$$

and Fourier's law for the heat flow

$$\vec{q} = -\kappa_D \vec{\nabla} T \tag{A.22}$$

in addition to the equation of state the dynamic transport coefficients can be defined, i.e. the shear viscosity η, the bulk viscosity ξ, and the heat conductivity κ_D. The computation of these quantities from the mechanics of the collision process and the probabilistic assumptions made for the distribution function alone is a principle success of Boltzmann's kinetic theory.

Appendix B

Transport Coefficients for Granular Material

In chapter (2.2) explicit expressions for transport coefficients are needed to derive the vertical density profile of a planetary ring. For this purpose the transport coefficients are employed that have been derived by Jenkins & Richman (1985) for dense rapidly sheared granular material in the nearly elastic limit. Also the equation of state and the granular cooling Γ given in that study are used.

Here ϵ is the constant coefficient of restitution, ϱ_p and d are the particle's bulk density and diameter, respectively, and $\mathit{ff} = \varrho/\varrho_p$ is the filling factor. The dynamic shear viscosity and heat conductivity are

$$\eta = \widetilde{\eta}\left(1 + \frac{2}{5}\mathit{ff}\, g_0(3\epsilon - 1)(1+\epsilon)\right)\left(1 + \frac{4}{5}\mathit{ff}\, g_0(1+\epsilon)\right) + \frac{3}{5}\xi \tag{B.1}$$

$$\widetilde{\eta} = \frac{5\varrho_p\, R_p\, \pi^{1/2} T^{1/2}}{12 g_0(1+\epsilon)(3-\epsilon)}$$

and

$$\kappa_D = \widetilde{\kappa}_D\left(1 + \frac{3}{5}\mathit{ff}\, g_0(1+\epsilon)^2(2\epsilon - 1)\right)\left(1 + \frac{6}{5}\mathit{ff}\, g_0(1+\epsilon)\right) + \frac{3}{2}\xi \tag{B.2}$$

$$\widetilde{\kappa}_D = \frac{25\varrho_p\, R_p\, \pi^{1/2} T^{1/2}}{2 g_0(1+\epsilon)(49 - 33\epsilon)}$$

Here, ξ is the dynamic bulk viscosity

$$\xi = \frac{8\varrho_p\, R_p\, \mathit{ff}^2 g_0(1+\epsilon) T^{1/2}}{3\pi^{1/2}}\,. \tag{B.3}$$

which arises only in dense systems where the effects of finite particle volume are taken into account in a collision integral of the form (A.11). When the dilute form of the collision integral, similar to the one in eq (A.2), is used, the transport coefficients reduce to the tilded quantities. The function

$$g_0(\mathit{ff}) = \frac{2 - \mathit{ff}}{2(1 - \mathit{ff})^3} \tag{B.4}$$

is the radial distribution function at contact (Carnahan & Starling, 1969), accounting for finite particle size effects in dense systems.

The equation of state for the sheared granular flow is

$$p = \rho T \left[1 + 2 \mathit{ff} g_0 (1+\epsilon) \right] \tag{B.5}$$

leading for $\epsilon = 1$ to the equation of state of Carnahan & Starling (1969).

For the granular cooling the expression

$$\Gamma = \frac{6 \varrho_p \mathit{ff}^2 g_0 (1-\epsilon^2) T^{3/2}}{\pi^{1/2} \, R_p} \tag{B.6}$$

is found.

The coefficient functions for the triaxial balance equations used in chapter (2.2), following Simon & Jenkins (1994), read

$$\begin{aligned}
\alpha &= \frac{[1 - \frac{2}{7}(1-\epsilon)][\frac{1}{5} - \frac{1}{7}(1-\epsilon)]}{(1+\epsilon)\left\{49 - 33\epsilon + \frac{1-\epsilon}{2744}(5\epsilon - 54)(237\epsilon - 461)\right\}} \\
\beta &= \frac{1}{9-5\epsilon}\sqrt{\frac{1-\epsilon}{125\pi d}\,(225\epsilon^2 + 4415\epsilon - 2876)} \\
\gamma &= \frac{48}{25\pi d^2}\left(1 + \frac{(\epsilon-1)(195\epsilon - 979)}{6272}\right)(1-\epsilon^2)\,,
\end{aligned} \tag{B.7}$$

and

$$\lambda = \frac{7}{2+5\epsilon}\,.$$